

# Measurement of the Indium 7P Excited-State Polarizabilities Using Two-Step Atomic Beam Spectroscopy

by  
Nathaniel B. Vilas

Professor Protik K. Majumder, Advisor

A thesis submitted in partial fulfillment  
of the requirements for the  
Degree of Bachelor of Arts with Honors  
in Physics

WILLIAMS COLLEGE  
Williamstown, Massachusetts  
May 21, 2017

## Abstract

We have made progress towards a series of precise measurements of the indium  $7P_{1/2}$  and  $7P_{3/2}$  polarizabilities using two-step atomic beam spectroscopy. Preliminary analyses give scalar polarizabilities of  $\alpha_0(7P_{1/2}) = 1.8064(32) \times 10^5 a_0^3$  and  $\alpha_0(7P_{3/2}) = 2.852(30) \times 10^5 a_0^3$ . Both results are in reasonable agreement with recent theoretical calculations and significantly more precise, though we require more data collection and error analysis in each case. In the experiment, we lock a 410 nm diode laser to the indium  $5P_{1/2} \rightarrow 6S_{1/2}$  resonance and overlap a counter-propagating 685-690 nm diode laser, tuned to one of the  $6S_{1/2} \rightarrow 7P_{1/2,3/2}$  transitions, through a collimated beam of indium atoms. We then use lock-in demodulation techniques to detect two-step transitions an order of magnitude weaker than those previously measured in our group. Alongside this experimental progress, we have developed a theoretical treatment of the Stark shift in a many-level atomic system coupled by two laser fields. This work allows for numerical lineshape simulations instrumental in the successful extraction of the  $7P_{3/2}$  tensor polarizability from atomic beam data. With continued refinements to theory and more data collection and systematic error analysis, we hope to achieve final measurements at or below the 1% level for all three quantities.

## Acknowledgements

First of all, I would like to thank my advisor, Professor Tiku Majumder. His warm personality, unbounded dedication to teaching, and extraordinary knowledge of physics have proven inspirational on a daily basis, and I will always be indebted to him for teaching me, above all else, to *think* like a physicist. I am similarly grateful to Professor Charlie Doret, whose comments as a second reader on this thesis were consistently illuminating, and whose brilliance as a teacher and experimentalist has demonstrated firsthand all that of which Majumder lab alumni are capable.

I am ever thankful to Dr. Milinda Rupasinghe for invaluable help around the lab; his constant work debugging troublesome portions of the apparatus, in particular, made my own experimental work all that much simpler. I also thank Michael Taylor and Jason Mativi for their help in the machine shop over the course of this work, particularly in fabricating a new crucible and measuring electric field plates. Professor Fred Strauch was generous in sitting down with me for a brief but illuminating discussion that planted the seeds of what became a significant theory project.

I thank Eli Hoenig for being a friendly labmate and partner in thesis work. Additionally, Bingyi Wang's and Ashay Patel's presence in lab at various points during the year made life in Bronfman basement all that much more vibrant. I would be remiss not to thank Allison Carter as well; her mentorship during the winter study of her thesis allowed me to hit the ground running on my own work this past summer.

Finally, I thank the wonderful people I met at Williams for making my four years here so extraordinary, and I thank my loving family for their support and for the opportunity to so readily pursue my passion for physics.

# Executive Summary

This thesis describes progress towards a series of high-precision measurements of the indium  $7P$  excited-state polarizabilities. We have nearly completed a measurement of the  $7P_{1/2}$  scalar polarizability and have made significant contributions towards a determination of the  $7P_{3/2}$  scalar and tensor polarizabilities. Our preliminary results for the scalar polarizabilities give  $\alpha_0(7P_{1/2}) = 1.8064(32) \times 10^5 a_0^3$  and  $\alpha_0(7P_{3/2}) = 2.852(30) \times 10^5 a_0^3$ ; both values have uncertainties at or below the 1% level and agree reasonably well with recently completed theoretical calculations. Figure 1 shows a comparison of present results and their corresponding theory values. In each case, we find that theory overestimates measured values by between 3 and 5 percent; this result is consistent with previous findings in lower states of indium.

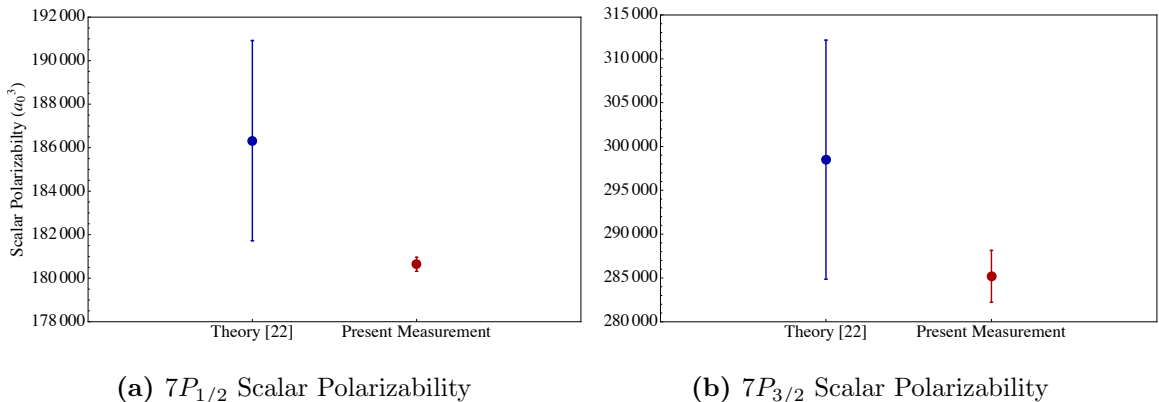


**Figure 1:** Comparison of present scalar polarizability results with theory for (a) the indium  $7P_{1/2}$  state and (b) the indium  $7P_{3/2}$  state.

In the Majumder lab, we make measurements of atomic observables, like polarizabilities, for precisely the purpose of such comparisons with the state-of-the-art in *ab initio* atomic theory calculations. Over the years our group has formed a productive partnership with that of Marianna Safronova at the University of Delaware. By completing precision measurements of structural quantities we aim to guide the refinement and test the accuracy of their theoretical methods in complicated atomic systems like indium. Ultimately, with improved theory, atomic systems can be used for tests of fundamental physics, giving our work a relevance beyond the world of precision spectroscopy.

The present measurements provide particularly strong tests of theory. The  $7P_{1/2}$  scalar polarizability is due largely to mixing with the nearby  $6D_{3/2}$  state, and so from our measurement we can determine the dipole matrix element between the two;  $D$  states are particularly challenging to model theoretically, and this offers a stringent test of such models. We can similarly extract  $D$ -state mixing matrix elements from the  $7P_{3/2}$  scalar polarizability, and the tensor polarizability offers a distinct test of theory regarding the *relative* magnitudes of such matrix elements.

We experimentally realize the present polarizability measurements using two-step laser spectroscopy in an atomic beam of indium atoms. This beam is formed by heating indium metal to 1100°C in a molybdenum crucible, newly machined over the course of this thesis, and allowing a collimated portion of the resulting vapor to propagate through a vacuum chamber held at  $\sim 10^{-7}$  Torr. We lock a 410 nm external cavity diode laser to the  $5P_{1/2} \rightarrow 6S_{1/2}$  ground-to-excited state transition, using an EOM-based frequency modulation technique to achieve long-term stability at the level of roughly 0.5 MHz. We collimate this light and propagate it orthogonally through the indium atomic beam. Two precisely spaced electric field plates surround this interaction region. From the opposite direction, we overlap a beam of 690 nm (685 nm) diode laser radiation with the 410 nm light to drive the ‘second-step’  $6S_{1/2} \rightarrow 7P_{1/2}$  ( $6S_{1/2} \rightarrow 7P_{3/2}$ ) resonance. By using a lock-in demodulation technique to observe the 690 nm (685 nm) absorption, we resolve the hyperfine resonances of the relevant  $7P$  state. Applying a precisely measured voltage across the capacitor plates in the interaction region allows us to observe and measure an induced Stark shift.

Though two-step excitation has previously been observed in the Majumder lab’s atomic beam apparatus, the beam’s low atomic density means that such a measurement is inherently quite challenging. The second-step transitions studied in this thesis are between one and two orders of magnitude weaker than those previously observed in the lab for indium, and significant experimental effort has accordingly been spent modifying the apparatus to allow for the observation of such unprecedentedly small absorption lines. A sample fit to this new atomic beam signal is shown in figure 2.

To extract a scalar polarizability from observed  $7P_{1/2}$  atomic beam signals, we measure the energy shift between electric field-on and field-off configurations, per the approach used in a recent lab measurement of the  $6P_{1/2}$  scalar polarizability. Because the  $7P_{3/2}$  state admits a tensor polarizability as well as the standard scalar component, however, we can no longer simply measure such energy shifts from field-free resonance – once-degenerate hyperfine sublevels now split under application of an electric field, and lineshapes become much more complicated.

We have, over the course of this thesis, undertaken a significant amount of theoretical work targeted at better understanding such behavior and developing a method of scalar and tensor polarizability extraction. At the core of this work was a full quantum mechanical treatment of the sixty-level system comprising all accessible hyperfine states in our two-step excitation scheme. By numerically diagonalizing the resulting Hamiltonian, we have been able to simulate observed lineshapes for a range of laser powers and polarizations (figure 3). These simulations have proven essential to our

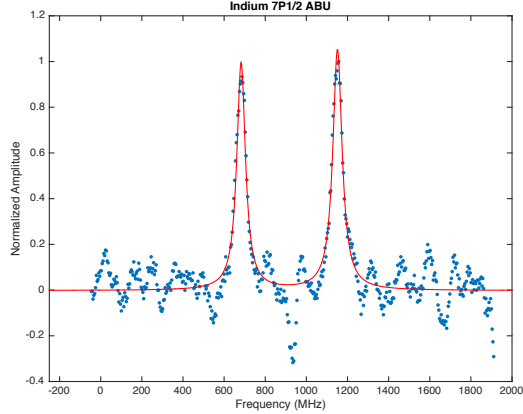


**Figure 2:** Observed indium  $7P_{1/2}$  atomic beam signal, along with a fit to a sum of two Lorentzian peaks (solid red line).

efforts towards the extraction of a tensor polarizability. Though this theory work is ongoing, we have arrived at a robust means of scalar polarizability determination, capable of yielding uncertainties at the 1% level despite significant imprecision in our knowledge of the tensor part.

We have assembled a suite of MATLAB code for use in analyzing  $7P_{1/2}$  and  $7P_{3/2}$  spectra. In all cases we have found that statistical errors in our fits will not be a limiting factor in the the precision of our measurements, allowing for the careful evaluation of systematic uncertainties. With further data collection and error analysis we hope in the near future to arrive at final, precise values for the  $7P_{1/2}$  and  $7P_{3/2}$  scalar polarizabilities at or below the 1% uncertainty level. Building from theory developed in this thesis, we hope that future work will also result in the lab's first-ever measurement of a tensor polarizability.

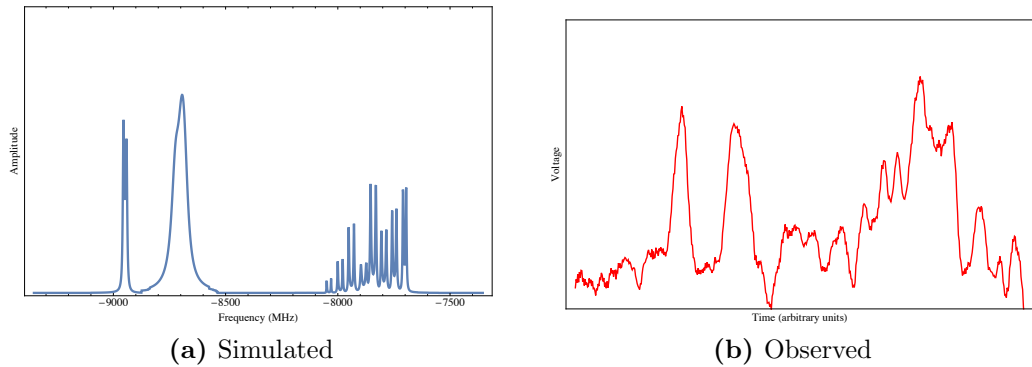


**Figure 3:** Comparison of simulated and observed indium  $7P_{3/2}$  atomic beam spectra under application of a 15 kV/cm electric field. Simulations were carried out by diagonalizing a  $60 \times 60$  Hamiltonian treating the full atomic system accessible in our two-step excitation scheme.

# Contents

Abstract . . . . .	iii
Acknowledgements . . . . .	v
Executive Summary . . . . .	vii
<b>1 Introduction</b>	<b>1</b>
1.1 Motivation . . . . .	1
1.2 Indium and Thallium . . . . .	3
1.3 Previous Work . . . . .	5
1.4 Present Work . . . . .	6
1.5 Outline of the Thesis . . . . .	6
<b>2 Atomic Theory and Spectroscopy</b>	<b>9</b>
2.1 Atomic Structure . . . . .	9
2.1.1 Fine Structure . . . . .	9
2.1.2 Hyperfine Structure . . . . .	10
2.2 Absorption Spectroscopy and Line Broadening . . . . .	11
2.2.1 Direct Absorption Spectroscopy . . . . .	11
2.2.2 Broadening Mechanisms . . . . .	12
2.2.3 Two-Step Spectroscopy . . . . .	15
<b>3 Atoms in External Electric Fields</b>	<b>17</b>
3.1 Polarizabilities and the Stark Effect . . . . .	17
3.2 The Stark Shift in an N-Level System . . . . .	21
3.2.1 The $7P_{1/2}$ State: Three Levels . . . . .	21
3.2.2 The $7P_{3/2}$ State: Sixty Levels . . . . .	24
3.3 Extraction of $7P_{3/2}$ Polarizabilities . . . . .	25
3.3.1 Scalar Polarizability Determination . . . . .	27
<b>4 Experimental Setup and Methods</b>	<b>29</b>
4.1 Overview of the Experiment . . . . .	29
4.2 Sources of Atoms . . . . .	30
4.2.1 Indium Vapor Cell . . . . .	30
4.2.2 Atomic Beam Unit . . . . .	30
4.3 Optical Setup . . . . .	34
4.3.1 External Cavity Diode Lasers (ECDLs) . . . . .	35

4.3.2	410 nm Laser Locking and Stark Shift Correction . . . . .	35
4.3.3	Vapor Cell Reference . . . . .	41
4.3.4	Atomic Beam Signal . . . . .	42
4.4	Data Collection Process . . . . .	43
<b>5</b>	<b>Data Analysis and Preliminary Results</b>	<b>45</b>
5.1	Data Fitting Procedure . . . . .	45
5.1.1	Frequency Mapping, Linearization, and Calibration . . . . .	45
5.1.2	Vapor Cell Reference Spectra . . . . .	46
5.1.3	Atomic Beam Fitting and Stark Shift Determination . . . . .	47
5.2	Preliminary $7P_{1/2}$ Results and Error Analysis . . . . .	51
5.2.1	Determination of Center Values and Statistical Errors . . . . .	51
5.2.2	Consideration of Systematic Errors . . . . .	53
5.2.3	Preliminary $7P_{1/2}$ Scalar Polarizability Results . . . . .	56
5.3	Preliminary $7P_{3/2}$ Scalar Polarizability Results . . . . .	57
<b>6</b>	<b>Ongoing and Future Work</b>	<b>63</b>
6.1	Continuing Scalar Polarizability Work . . . . .	63
6.1.1	$7P_{1/2}$ Scalar Polarizability . . . . .	63
6.1.2	$7P_{3/2}$ Scalar Polarizability . . . . .	64
6.2	$7P_{3/2}$ Tensor Polarizability Work . . . . .	64
<b>A</b>	<b>Atomic Units and Literature Corrections</b>	<b>67</b>
<b>B</b>	<b>Atomic Theory Results</b>	<b>69</b>
B.1	Broadened Lineshapes . . . . .	69
B.1.1	Doppler Broadening . . . . .	69
B.1.2	Lifetime Broadening . . . . .	70
B.1.3	Power Broadening . . . . .	71
B.2	Many-Level Systems . . . . .	72
B.2.1	The Wigner-Eckart Theorem and Polarization Selection Rules . . . . .	72
B.2.2	The Generalized Three-Level Hamiltonian . . . . .	74
B.3	$7P_{3/2}$ Tensor Polarizability Extraction . . . . .	78
<b>C</b>	<b>Mathematica Simulations</b>	<b>85</b>
C.1	Three-Level Lineshapes . . . . .	85
C.2	Generalized Three-Level Lineshapes . . . . .	85
C.3	$7P_{3/2}$ Scalar Polarizability Extraction . . . . .	90
<b>D</b>	<b>MATLAB Code</b>	<b>91</b>
D.1	$7P_{1/2}$ Stark Shift Code . . . . .	91
D.1.1	Fitting of Raw Data . . . . .	91
D.1.2	Final Analysis . . . . .	94
D.2	$7P_{3/2}$ Polarizability Code . . . . .	94

<b>E Indium 7P Hyperfine Splitting Measurements</b>	<b>97</b>
E.1 Experimental Setup . . . . .	97
E.2 Analysis Method . . . . .	97
E.3 Extraction of Splittings and Statistical Errors . . . . .	99
E.4 Consideration of Systematic Errors . . . . .	101
E.5 Final Results . . . . .	105

# List of Figures

1	Scalar Polarizability Theory Comparisons . . . . .	vii
2	$7P_{1/2}$ Atomic Beam Signal . . . . .	ix
3	Simulated and Observed $7P_{3/2}$ Spectra . . . . .	ix
1.1	Indium $6P_{1/2}$ Theory Comparison . . . . .	4
1.2	Group IIIA Energy Diagrams . . . . .	5
2.1	Comparison of Lineshapes . . . . .	14
3.1	Stark-Shifted $7P_{1/2}$ Levels . . . . .	19
3.2	Tensor Polarizability Splitting . . . . .	20
3.3	Analytic Lineshapes for a Two-Step Transition . . . . .	23
3.4	Simulated 15 kV/cm Spectrum . . . . .	26
4.1	Full Experimental Setup . . . . .	30
4.2	New Indium Crucible . . . . .	32
4.3	Vacuum System . . . . .	33
4.4	Interaction Region . . . . .	34
4.5	Simulated FM Locking Lineshapes . . . . .	37
4.6	Locking Setup . . . . .	38
4.7	Observed Locking Signal . . . . .	38
4.8	410 nm Lock Quality . . . . .	39
4.9	AOM Setup for Lock Correction . . . . .	40
4.10	$7P_{1/2}$ Data Acquisition Outline . . . . .	44
5.1	$7P_{1/2}$ Vapor Cell Spectrum . . . . .	48
5.2	$7P_{1/2}$ Atomic Beam Signal . . . . .	49
5.3	Overlapped Atomic Beam Signals . . . . .	51
5.4	Fitted Chi-Squared Curve . . . . .	52
5.5	$7P_{1/2}$ Stark Shift Histograms . . . . .	53
5.6	$7P_{1/2}$ Shift vs. Electric Field . . . . .	54
5.7	Binary Systematics . . . . .	55
5.8	Field Correlation Systematic . . . . .	56
5.9	$7P_{1/2}$ Scalar Polarizability Theory Comparison . . . . .	58
5.10	$7P_{3/2}$ Atomic Beam Signal . . . . .	59
5.11	$7P_{3/2}$ Data Acquisition Outline . . . . .	59

5.12 $7P_{3/2}$ Atomic Beam Fit . . . . .	60
B.1 Simulated $7P_{3/2}$ , $ F, m_F\rangle =  4, 4\rangle$ Lineshapes . . . . .	80
B.2 Simulated $7P_{3/2}$ ‘Composite’ Peak . . . . .	81
B.3 Tensor Polarizability Divergence . . . . .	83
C.1 Three Level Mathematica Code . . . . .	86
C.2 Mathematica Code for Generalized Three Level Hamiltonian . . . . .	88
C.3 Sixty Level Mathematica Code . . . . .	89
C.4 Hyperfine Level Energy Determination . . . . .	90
C.5 $7P_{3/2}$ Scalar Polarizability Extraction Code . . . . .	90
E.1 $7P_{1/2}$ Hyperfine Signal . . . . .	98
E.2 $7P_{3/2}$ Hyperfine Signal . . . . .	98
E.3 HFS Experimental Setup Diagram . . . . .	99
E.4 HFS Histograms . . . . .	100
E.5 Hyperfine Group Systematic . . . . .	105

# List of Tables

2.1	Indium Structure and Magnitudes . . . . .	10
5.1	$7P_{1/2}$ Stark Shift Results . . . . .	57
5.2	Comparison of Polarizabilities with Theory . . . . .	61
A.1	Quantities Taken to One in Atomic Units . . . . .	67
A.2	Corrected Publication Values . . . . .	68
B.1	Composite Peak Simulation Data . . . . .	81
E.1	$7P_{1/2}$ and $7P_{3/2}$ Hyperfine Splitting Results . . . . .	106
E.2	Comparison of Hyperfine Results . . . . .	106

# Chapter 1

## Introduction

When, in 1947, Willis Lamb and Robert Retherford announced their measurement of a small energy difference between the  $2S_{1/2}$  and  $2P_{1/2}$  states of hydrogen, it marked the start of a revolution in modern physics. Contained in this rather unassuming splitting, known to future generations of physicists as the Lamb shift, was a simple comment on all that was wrong with physics as it stood after World War II. Dirac's famous equation was rendered obsolete, and the desire to explain the new measurement drove a generation of physicists towards the development of quantum electrodynamics. Such was the importance of atomic spectroscopy at the cutting edge of physics in the middle of the twentieth century. Moreover, in this one measurement was embodied, perhaps better than any other, the astoundingly seductive nature of pursuits towards yet-more-precise measurements of nature's building blocks. It is, after all, only by digging deeper that we uncover new physics.

In the Majumder group we perform the measurements of atomic structure so critical to the successful extraction of fundamental physics from atomic systems. Our work has centered on the Group IIIA atoms thallium and indium, though work concurrent with this thesis [1] marks the group's first foray into the study of lead. In this thesis I describe one series of measurements aimed at a further understanding of the structure of atomic indium.

### 1.1 Motivation

#### Atoms as Testbeds for Fundamental Physics

Atoms, as core constituents of our physical world, are governed by the most fundamental laws of nature. At least in principle, then, through the careful study of atomic behavior one should be able to approach an understanding of such foundational physics. Experiments of this sort are not uncommon. Thallium, in particular, has been employed in work aimed at the observation of parity nonconserving (PNC) optical rotations [2] as well as in several measurements of electric dipole moments (EDMs) and potential CPT violation [3, 4]. Indium, too, has been proposed as a fertile medium for EDM measurements [5].

The difficulty in such measurements is that atoms are not vessels of exciting fundamental physics alone; rather, such interesting physics tends at first glance to be obscured by properties specific to the atomic testing ground. To illustrate this, we might take as an example the PNC measurements performed in [2]. The observable in this case,<sup>1</sup> an optical rotation we might call  $\epsilon_w$ , can be expressed as the product of two quantities,

$$\epsilon_w = Q_w \mathcal{C}(Z) \quad (1.1)$$

where  $Q_w$  represents the fundamental physical quantity of interest (in this case the so-called weak charge from electroweak theory) and  $\mathcal{C}(Z)$  contains the atom-specific effects in the measurement – those effects that would cause  $\epsilon_w$  to change if the measurement were performed in, say, lead instead of thallium. The challenge, accordingly, is to understand  $\mathcal{C}(Z)$  in any particular atom with enough precision to extract meaningful values of  $Q_w$ , which tends to be quite small.<sup>2</sup> The achievement of such a lofty goal requires exceptionally precise atomic theory, and it is in service of this requirement that the work of the Majumder group comes into play.

### Precision Measurements as Guideposts for Atomic Theory

As outlined in [6], efforts at extracting values for  $Q_w$  from optical rotation measurements in both cesium and in thallium, while in agreement with standard model predictions, result in large uncertainties dominated by error bars in the  $\mathcal{C}(Z)$  theory. This theory consists of precise, *ab initio* quantum-mechanical wavefunction calculations for the atoms of interest, a non-trivial matter requiring well-chosen approximations for any atom larger than hydrogen (one of the few systems that quantum mechanics *can* solve analytically).

Such theoretical calculations, of course, can be used to predict a variety of atomic structural quantities (examples in multi-electron atoms are found in [7–12]), and it is through comparison with experimental measurements of these quantities that one can develop an understanding of the accuracy and precision of the theory. These benchmark values come in many forms – examples include lifetimes, energies, transition rates, and dipole matrix elements – but in this thesis our particular interest is in polarizabilities (as well as in hyperfine splittings, at least tangentially – see appendix E). It is only by measuring a variety of such complementary properties that we can gather a complete picture of an atom’s structure: hyperfine splittings, for instance, test short-range wavefunction behavior while polarizabilities, in their reliance on external electric fields, test the long-range behavior of those same calculations.

It should be emphasized that our work is not simply to make measurements of atomic structure but to perform *precision* measurements of the same; the goal is

---

<sup>1</sup>Though the notation of this discussion is specific to the case of PNC optical rotations, the same principle applies to most any experiment aimed at extracting fundamental physics from atomic measurements.

<sup>2</sup>The reason we’re still searching for such fundamental physics, after all, is that its effects are very difficult to detect.

always to achieve uncertainties below the 1% level. The purpose of these experiments, after all, is not simply to confirm or refute the state-of-the-art in *ab initio* wavefunction calculations but to push forward that theory – in both accuracy and precision – by providing it with ever more precise benchmarks towards which to strive.<sup>3</sup> Indeed, our measurements often fall into statistical agreement with theory but represent near order-of-magnitude improvements in precision.

## 1.2 Indium and Thallium

The work of the Majumder group has, until recently, focused exclusively on measurements in the group IIIA atoms indium and thallium. One motivation regards their valence structure: though they contain three valence electrons, two are bound in an *s* state while the third is alone in a *p* state (we might notate the structure  $ns^2p^1$ ). This arrangement lends itself to two approaches towards the *ab initio* wavefunction calculations described above. The first treats the atom as having a single valence electron, that in the *p* state, making the calculation similar to that used in hydrogenic systems like the alkalis. The other considers all three valence electrons together, incorporating the effects of the two in the *s* state as well. Accordingly, group IIIA atoms fall into a ‘sweet spot’ in the theory: they are not so easy to compute as the alkalis (which are themselves one step away from hydrogen, ionized helium, and the other analytically solvable single-electron systems), but rather represent the next logical step in difficulty beyond those hydrogenic, single-valence systems.

As an illustration of the relevance of the two disparate approaches to wavefunction calculations in group IIIA atoms, we can refer to the results of [13] in conjunction with the theory calculations in [11]. The experiment contained within the former, carried out in the Majumder lab by two previous thesis students, demonstrates a scalar polarizability for the  $6P_{1/2}$  state of indium that falls between the two theory results of [11], as seen in figure 1.1. The result is certainly closer to the theory approach that takes all three valence electrons into account, but the remaining discrepancy indicates the potential validity of both approaches.

An important motivation for our use of thallium, in particular, is its history of use in tests of fundamental physics like [2]. These tests rely specifically on the precision of wavefunction calculations for the element, and so measurements of the sort performed in the Majumder lab are particularly necessary and relevant. More generally, physical effects like those represented by  $Q_w$  in equation 1.1 scale rapidly with atomic number, making heavy atoms like thallium ( $Z = 81$ ) particularly suitable choices for fundamental physics tests.

If thallium is the group IIIA atom most relevant to atomic tests at the foundations of physics, measurements in indium ( $Z = 49$ ) are nearly as useful by virtue of the element’s identical valence structure – the approximations used in indium wavefunction

---

<sup>3</sup>We pick the 1% level specifically because it tends to outpace theory precision rather handily – the latter is typically at or above 5%.

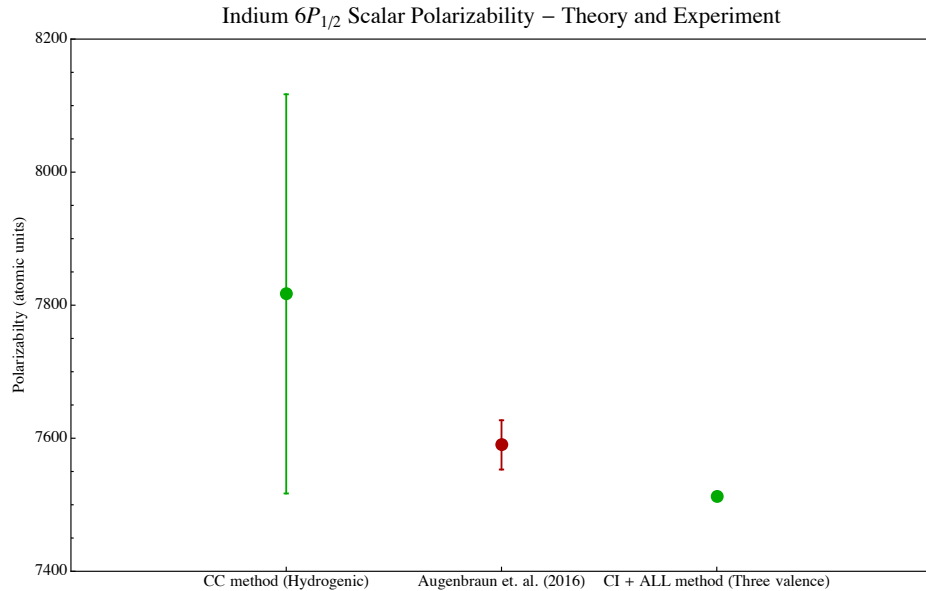


**Figure 1.1:** Comparison of the experimental results of [13] with the theoretical calculations of [11] for the indium  $6P_{1/2}$  scalar polarizability. Note how the experimental value falls between the theory numbers, though it prefers the approach that takes all three valence electrons into consideration. The error bar on the CC method covers the difference between the two theory values and can be treated as an error bar on the theory as a whole (this is why there is no quoted error for the CI + ALL method).

calculations should be equally valid for thallium – and, as an experimental bonus, indium has the advantage of not being highly toxic.<sup>4</sup> To this end, it is possible to conduct roughly analogous experiments in the two atoms, simply subtracting 1 from the principal quantum number in thallium to achieve its indium counterpart (e.g. an experiment probing the 378 nm  $6P_{1/2} \rightarrow 7S_{1/2}$  transition in thallium becomes an experiment on the 410 nm  $5P_{1/2} \rightarrow 6S_{1/2}$  transition in indium). See figure 1.2 for an overview of the indium energy levels relevant to the present work, as well as their thallium counterparts. It is worth noting that all ‘second-step’ wavelengths fall within the 655 - 690 nm range; in practice, this means that we can use the same laser and simply exchange diodes to probe all four transitions.

For our purposes, the only significant difference between indium and thallium arises in their hyperfine structure. Indium possesses an unusually large nuclear magnetic moment (nuclear spin  $I = 9/2$ ), resulting in more than two hyperfine levels in states for which  $J > 1/2$ . As much of the work outlined below regards the  $7P_{3/2}$  state of indium, that its four hyperfine levels differ from thallium’s two is interesting to bear in mind.

---

<sup>4</sup>Wikipedia tells us that ‘Because of its historic popularity as a murder weapon, thallium has gained notoriety as “the poisoner’s poison” and “inheritance powder” (alongside arsenic)’ (<https://en.wikipedia.org/wiki/Thallium>).

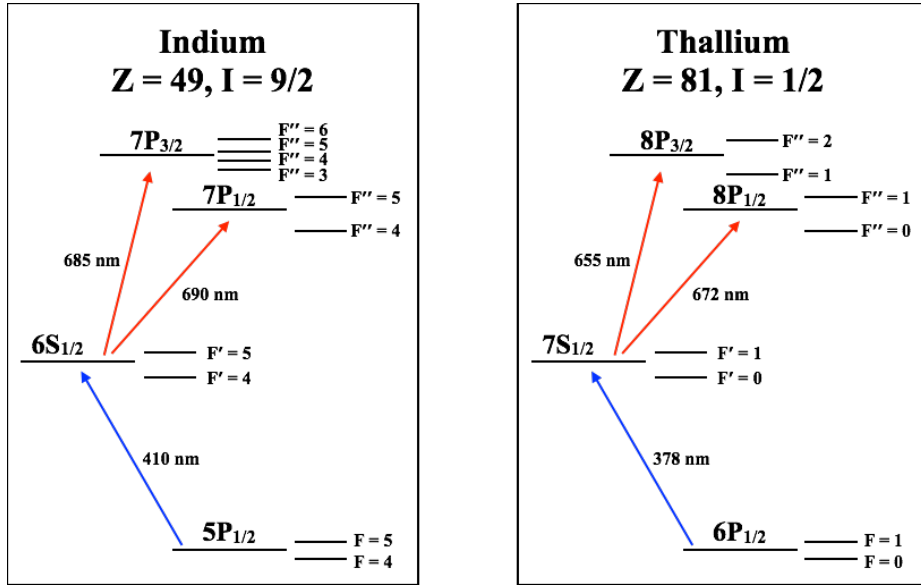


**Figure 1.2:** Diagram of relevant energy levels in indium and thallium. Note their closely analogous structures: besides the expected difference in principal quantum number, the only discrepancies arise at the level of hyperfine structure due to indium’s particularly high nuclear spin,  $I$ .

### 1.3 Previous Work

Since the inception of the Majumder lab at Williams in 1994, the group has performed measurements of polarizabilities, hyperfine splittings, and other structural quantities in several states of indium and thallium. One series of measurements involved hyperfine splittings [14–16]; a new set of such measurements was completed over the first summer of this thesis (see appendix E and [17]) and represents a culmination, for now, of this line of work.

Previous atomic beam work in the group, meanwhile, involved scalar polarizability measurements of single step, low-lying transitions in thallium and indium [18, 19]. More recent work, published in 2016, represented the first application of two-step spectroscopy to polarizability measurements in the atomic beam [13]. The measurement described in the body of this thesis represents an extension of the latter technique.

Other than those conducted in the Majumder lab over the past five years [13, 19], indium has not historically been the subject of many polarizability measurements. Atomic beam polarizability work was also done on the  $5P_{1/2} \rightarrow 6S_{1/2}$  transition in 1970 [20], and within the ground state in 1984 [21]. Both measurements were completed at the 10% level; for comparison, a 2013 Majumder group measurement [19] of the same polarizability as [20] improved the error bar by an order of magnitude, to 0.3%.

The most recent and complete set of theoretical polarizability calculations in indium was completed in 2013 [11]. Both previous Majumder lab measurements in indium [13, 19] are in good agreement with these values. At our request, calculations

of the indium  $7P_{1/2}$  scalar polarizability and  $7P_{3/2}$  scalar and tensor polarizabilities were completed for the purpose of comparison to present work [22].

## 1.4 Present Work

The work presently described is an extension, with significant modifications, of the line of work leading to a Majumder lab measurement of the indium  $6P_{1/2}$  scalar polarizability in 2016 [13]. We now consider the  $7P_{1/2}$  and  $7P_{3/2}$  states, switching out a near-infrared for a red laser in our two-step spectroscopic scheme. Both states have properties that make these measurements worthwhile. The scalar polarizability<sup>5</sup> of the  $7P_{1/2}$  state is roughly a factor of 30 larger than that of the  $6P_{1/2}$  state, meaning that it can be extracted to good precision without excessive difficulty. Most interesting from a theoretical perspective is that a measurement of the scalar polarizability in this state can be easily interpreted as a dipole matrix element between it and a nearby  $D$  state in indium.<sup>6</sup> Such matrix elements are difficult to directly measure experimentally, yet they provide particularly valuable tests of atomic theory.

The  $7P_{3/2}$  state is interesting in that it admits a tensor component to its polarizability. This piece, which causes hyperfine levels to *split* under application of an electric field, is much more challenging to measure than its scalar counterpart but provides a particularly robust test of atomic theory.

Over the course of this thesis we have worked to realize polarizability measurements in both states. While work is ongoing, we have arrived at a preliminary value for the  $7P_{1/2}$  scalar polarizability well below the 1% level; it *disagrees* with theory in precisely the way we might expect. We have also determined a preliminary value for the  $7P_{3/2}$  scalar polarizability at the 1% level and have devoted significant theoretical work towards an understanding of the tensor polarizability in the indium  $7P_{3/2}$  state, making progress towards a method for its determination.

## 1.5 Outline of the Thesis

This thesis begins by working through the requisite theory for understanding our spectroscopic measurements of the indium  $7P$  polarizabilities. We then describe the experimental and analytic methods employed in the execution of these measurements. In chapter 2 we introduce several fundamental concepts of atomic physics and atomic spectroscopy. This includes a discussion of the structure of the indium  $7P$  states along with the broadening mechanisms contributing to observed lineshapes. In chapter 3 we consider the theory underlying atomic behavior in the presence of external electric fields, beginning with a discussion of the Stark effect and continuing on to

---

<sup>5</sup>This part of the polarizability is responsible for homogeneous shifts of atomic level energies under the influence of an external electric field – see chapter 3.

<sup>6</sup>As will be seen in chapter 3, the scalar polarizability can be written as a sum over matrix elements, and it turns out the one in question accounts for  $\sim 97\%$  of the sum.

considerations of atomic systems with more than two levels under the influence of external fields. In the process we work towards an understanding of how to extract polarizabilities from observed atomic spectra. Chapter 4 describes the experimental apparatus and techniques used to detect *very* small signals from an atomic beam of indium. In chapter 5 we discuss the analysis methods employed in the experiment and quote preliminary values and error budgets for the  $7P$  polarizabilities measured in this thesis. Finally, chapter 6 looks ahead, discussing short-term future work and prospects for the present experiment.

# Chapter 2

## Atomic Theory and Spectroscopy

In this chapter we introduce the atomic theory necessary for a proper understanding of the spectroscopic measurements described in this thesis. In section 2.1 we offer a brief overview of the fundamentals of atomic structure. Section 2.2 turns to spectroscopy – the probing of atomic structure with electromagnetic radiation – briefly touching upon the nature of absorption spectroscopy and then discussing a series of mechanisms that broaden observed lineshapes. We close by introducing the two-step spectroscopic scheme used in this thesis. For more theory regarding the behavior of atoms in external electric fields, see chapter 3.

### 2.1 Atomic Structure

We here assume familiarity with elementary atomic structure as introduced in any modern physics course, including the quantum numbers  $n$ ,  $L$ ,  $m_L$ , and  $S$  and their interpretations. What follows is a brief discussion of smaller effects: the fine structure due to the spin-orbit interaction and the hyperfine structure due to nuclear-electronic spin-spin coupling.

#### 2.1.1 Fine Structure

The first effect, appearing at energy scales roughly a factor of  $Z^2\alpha^2$  (where  $Z$  is the atomic number and  $\alpha \approx 1/137$  is the fine structure constant) smaller than the above-mentioned gross structure, is what we call ‘fine structure.’ In the case of indium, the gross transitions we probe ( $5P_{1/2} \rightarrow 6S_{1/2}$ ,  $6S_{1/2} \rightarrow 7P_{1/2,3/2}$ ) have splittings of order  $10^{14}$  Hz while the fine structure splitting between the  $7P$  states is of order  $10^{12}$  Hz. Table 2.1 presents an overview of the magnitudes of various splittings of interest in this thesis, including the hyperfine splitting discussed below.

Fine structure arises from interactions between electron spin and orbital angular momentum,<sup>1</sup> denoted here by the operators  $\vec{S}$  and  $\vec{L}$ , respectively. Because this

---

<sup>1</sup>A semiclassical but intuitive picture suggests that this interaction is between two magnetic fields: one due to the magnetic moment of the spinning electron, and the other due to the current associated

Structure	Transition	Splitting
Gross	$5P_{1/2} - 6S_{1/2}$	$7.3 \times 10^8$ MHz
	$6S_{1/2} - 7P_{1/2,3/2}$	$4.3 \times 10^8$ MHz
Fine	$7P_{1/2} - 7P_{3/2}$	$3.3 \times 10^6$ MHz
Hyperfine	$7P_{1/2}(F = 4 - F = 5)$	$4.6 \times 10^2$ MHz

**Table 2.1:** Types of structure found within the indium atom, with representative splittings and magnitudes relevant to the present work.

structure is discussed in any intermediate quantum mechanics text we will here forgo substantive treatment. Worth knowing is the fine structure Hamiltonian,

$$H_{fs} \propto \vec{L} \cdot \vec{S}, \quad (2.1)$$

and that the solution allows the introduction of a new angular momentum operator,  $\vec{J} = \vec{L} + \vec{S}$ . Angular momentum addition rules dictate that in a state with  $L = 1$  and  $S = 1/2$  we should have fine structure levels for which  $J = 1/2$  and  $J = 3/2$ , as is the case for the  $7P_{1/2}$  and  $7P_{3/2}$  states of indium.

## 2.1.2 Hyperfine Structure

Beyond the fine structure due to spin-orbit coupling (and roughly a factor of  $m_e/m_p$  smaller in energy) comes atomic structure due to interactions between total electronic angular momentum and nuclear spin – the so-called (and perhaps not very creatively so) hyperfine interaction. The Hamiltonian for this effect is given by

$$H_{hf} = a(\vec{I} \cdot \vec{J}), \quad (2.2)$$

where  $\vec{I}$  is the spin of the nucleus,  $\vec{J} = \vec{L} + \vec{S}$  is the total electronic angular momentum, and  $a$  is some constant determining the magnitude of the interaction.<sup>2</sup>

Defining an angular momentum operator  $\vec{F}$  such that  $\vec{F} = \vec{I} + \vec{J}$  allows for a convenient re-expression of the hyperfine Hamiltonian in terms of familiar angular momenta. Namely, if we take the square of  $\vec{F}$  and solve the resulting equation for  $\vec{I} \cdot \vec{J}$ , we find that

$$H_{hf} = \frac{a}{2}(F^2 - J^2 - I^2), \quad (2.3)$$

which leads to energy eigenvalues of<sup>3</sup>

$$\frac{a}{2}[F(F+1) - J(J+1) - I(I+1)]. \quad (2.4)$$

---

with the proton's orbit in the electron frame.

<sup>2</sup>It turns out that this is only one term of the full hyperfine Hamiltonian (see, for instance, [23]) but it is all we need for consideration of  $J=1/2$  states.

<sup>3</sup>Up to a factor of  $\hbar^2$ , which we can absorb into the  $a$  constant.

For the  $7P_{1/2}$  state of indium, we have  $I = 9/2$  and  $J = 1/2$ , yielding two hyperfine levels,  $F = 4$  and  $F = 5$ . Substituting these values into equation 2.4 and subtracting the two resulting energies yields a hyperfine splitting of

$$\Delta\nu_{5-4} = 5a. \quad (2.5)$$

Thus the hyperfine splitting,  $\Delta\nu_{5-4}$ , can just as easily be expressed in terms of the hyperfine constant,  $a$ .

While hyperfine splittings in  $J = 1/2$  states can be expressed exactly<sup>4</sup> in terms of the magnetic dipole interaction described above, higher  $J$  states admit higher-order multipole terms. Accordingly, we can no longer express the hyperfine splittings for the  $7P_{3/2}$  state of indium in terms of a single hyperfine constant and must rather allow for a dipole constant,  $a$ , a quadrupole constant,  $b$ , and an octupole constant,  $c$ . Following [15] and using expressions for the  $b$  and  $c$  constants found in [24], we can write the  $7P_{3/2}$  splittings in terms of these constants as follows:

$$\begin{aligned}\Delta\nu_{4-3} &= 4a - \frac{2}{3}b + \frac{208}{21}c, \\ \Delta\nu_{5-4} &= 5a - \frac{5}{24}b - \frac{65}{6}c, \\ \Delta\nu_{6-5} &= 6a + \frac{2}{3}b + \frac{16}{3}c.\end{aligned} \quad (2.6)$$

We note that while there are four hyperfine levels ( $F = 3, 4, 5, 6$ ) in the  $7P_{3/2}$  state, the selection rule  $\Delta F = 0, \pm 1$  dictates that we are only ever able to observe three at a time. For most of this thesis we will be interested in the  $F = 4, 5, 6$  levels alone; to see them we should thus drive transitions from the  $6S_{1/2}(F = 5)$  state.

## 2.2 Absorption Spectroscopy and Line Broadening

### 2.2.1 Direct Absorption Spectroscopy

In the Majumder group we employ laser absorption spectroscopy to study the atomic transitions induced by interactions between atoms and electromagnetic radiation. When we direct laser radiation of frequency  $\omega$  (near but not necessarily on the atomic resonance,  $\omega_0$ ) and intensity  $I$  through a sample of atoms of differential length  $dz$ , the differential change in laser intensity measured after the atomic sample is seen to be

$$dI = -A(\omega)Idz,$$

where  $A(\omega)$  quantifies the absorption of light at frequency  $\omega$ . Straightforward integration gives us an expression for the transmitted intensity,

$$I(\omega) = I_0 e^{-\alpha P(\omega)}, \quad (2.7)$$

---

<sup>4</sup>At least within the confines of first-order perturbation theory – so perhaps it's not truly an exact solution.

where here we have made the substitution  $A(\omega)z = \alpha_{(z)}P(\omega)$ . In this recasting  $P(\omega)$  is the atomic probability of absorption (normalized to equal 1 on resonance) and  $\alpha$  is called the *optical depth*. The latter quantity indicates the magnitude of absorption and is given by  $\alpha = \int n\sigma dz$ , where  $n$  is the atomic number density and  $\sigma$  is the so-called *resonant absorption cross section*.

When we make measurements of atomic structure we record this transmitted intensity function,  $I(\omega)$ . We extract information about atomic structure through the relationship (equation 2.7) between  $I(\omega)$  and the probability of atomic absorption,  $P(\omega)$ ; it is this latter function that tells us the resonance frequencies of the transitions of interest.

## 2.2.2 Broadening Mechanisms

There are a variety of broadening mechanisms – due both to experimental limitations and to intrinsic quantum mechanical effects – that lead to the absorption of a finite amount of off-resonant light and widen the absorption profiles we observe. Below, we outline the broadening mechanisms most relevant to the present experiment.

### Doppler Broadening

If we direct a single laser into a hot atomic vapor (like the  $\sim 750^{\circ}\text{C}$  cell of indium atoms described later) we will observe an absorption profile with width of order 1 GHz. This broadening arises due to the Doppler effect, wherein an atom moving relative to the incident laser beam experiences a frequency shift of

$$\omega_{\text{atom}} \approx \omega_0 \left(1 - \frac{v_z}{c}\right), \quad (2.8)$$

where  $\omega_0$  is the incident laser frequency in the lab frame,  $\omega_{\text{atom}}$  is the observed frequency in the atom frame,  $v_z$  is the velocity of the atom along the laser propagation axis, and the approximation holds for  $v_z \ll c$  (easily satisfied as our atoms move at several hundred meters per second).

As shown in Appendix B, invoking the Maxwell-Boltzmann velocity distribution to account for all atoms interacting with the laser radiation ultimately associates with this ‘Doppler broadening’ a Gaussian absorption profile with full width at half maximum (FWHM)

$$\Delta = \frac{\omega_0}{c} \sqrt{\frac{8kT \ln 2}{m}}, \quad (2.9)$$

where  $k$  is the Boltzmann constant,  $T$  is the temperature, and  $m$  is the atomic mass. For the 410 nm indium  $5P_{1/2} \rightarrow 6S_{1/2}$  transition we study in a vapor cell at  $T = 750^{\circ}\text{C}$ , this yields a Doppler width of  $\Delta/2\pi \approx 1.6$  GHz. This is significantly larger than any other broadening mechanism present in our experiment.

There are, of course, numerous well-known methods of resolving ‘Doppler-free’ spectra beyond this limit. Such a technique is built in to the two-step spectroscopic scheme of our current work – see section 2.2.3 below.

Though eliminating the Doppler effect from our spectra significantly reduces linewidth, the remaining absorption lines are still not delta functions – rather, we find Lorentzian peaks with widths of order 50 – 100 MHz due, primarily, to two additional sources of broadening.

### Lifetime Broadening

The first of these broadening mechanisms reflects a fundamental limit on linewidth imposed by the uncertainty principle. Because an atom does not remain in an excited state indefinitely but instead spontaneously decays with some characteristic time  $\tau$ , there should be an uncertainty in the energy of that state following  $\tau\Delta E \sim \Delta t\Delta E \sim \hbar$ . It turns out (Appendix B) that the lineshape corresponding to this broadening mechanism is Lorentzian, with FWHM precisely as expected from the uncertainty principle above:

$$\Gamma = \Delta\omega = \frac{1}{\tau} . \quad (2.10)$$

For a transition between two excited states  $|i\rangle$  and  $|f\rangle$ , each with its own lifetime, the natural linewidth of the transition is the sum of the two individual linewidths:  $\Delta\omega = \Delta\omega_i + \Delta\omega_f$ . Considering the 685 and 690 nm indium  $6S_{1/2} \rightarrow 7P$  transitions we study here and consulting [8], we find  $\tau_{6S_{1/2}} \approx 7$  ns and  $\tau_{7P} \sim 200$  ns. The lower state then dominates the energy uncertainty, and we find a natural linewidth of  $\Gamma/2\pi \approx 24$  MHz. It is worth noting that this is an example of *homogeneous* broadening – meaning that every atom is affected equally – in contrast with the *inhomogeneous* Doppler broadening described above, wherein a widened line arises from differences between atoms.

### Power Broadening

Though the natural linewidth of the transitions we study should be of order 20-30 MHz, we observe widths between 2 and 4 times greater in our two-step excitation signals. The most significant contribution to this additional width originates from the power of the incident laser radiation. Specifically, once there is enough laser power to induce a significant depopulation of the lower state in a transition (or to induce Rabi oscillations in a significant number of atoms), we find (Appendix B) a Lorentzian profile broadened from the natural linewidth,  $\Gamma_{\text{Natural}}$ , by a factor

$$\Gamma_{\text{Power}} = \Gamma_{\text{Natural}}\sqrt{1+S} , \quad (2.11)$$

where  $S = \Omega_R^2\tau^2$ , with resonant Rabi frequency  $\Omega_R$  and state lifetime  $\tau$ , is also called the *saturation parameter*.

Using dipole matrix elements calculated in [8] combined with measured laser powers and beam sizes, we estimate Rabi frequencies of 5-10 MHz for the 410 nm  $5P_{1/2} \rightarrow 6S_{1/2}$  and 685 nm  $6S_{1/2} \rightarrow 7P_{3/2}$  transitions, leading to broadened linewidths of  $\sim 25$  and  $\sim 5$  MHz, respectively. Our power-broadened line, then, has a width of  $\Gamma/2\pi \approx 30$  MHz. While this is not quite what we observe in our two-step spectra, it offers a better estimate than does lifetime broadening alone.

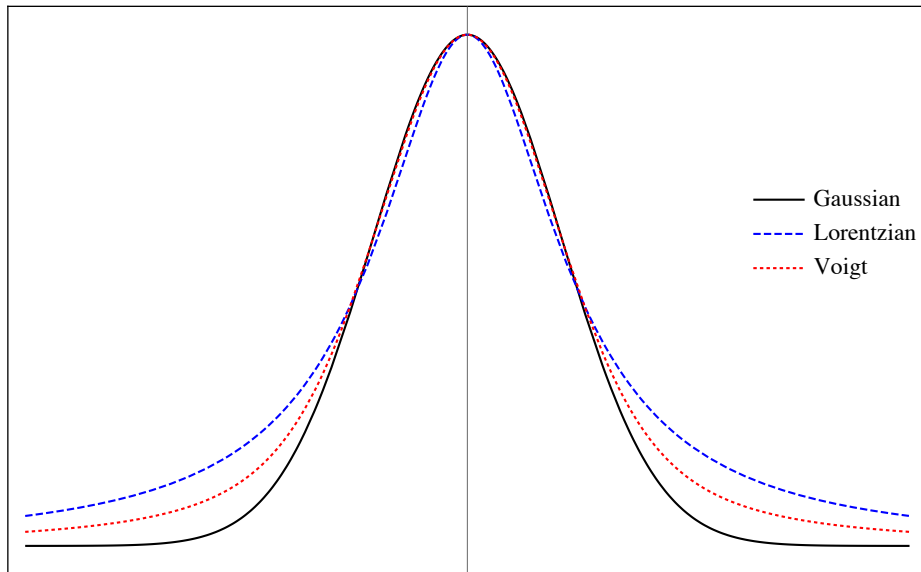


**Figure 2.1:** Comparison of Lorentzian, Gaussian, and Voigt profiles. Note that the Lorentzian is defined by its wide tails, while the Gaussian is more box-like in shape, with the Voigt adopting characteristics of each.

### Additional Broadening Mechanisms and Voigt Convolution

While additional broadening mechanisms exist due to finite laser linewidth, atomic collisions, and the finite transit time of atoms through the path of incident laser radiation, their contributions are all at or below the 1 MHz level and are accordingly negligible.

The last question we address is the nature of the total observed lineshapes. In the 410 nm first-step transition alone, we see both Gaussian (Doppler effect) and Lorentzian (natural and power broadened) contributions to the broadening, and in the second-step spectra there will always exist some residual Gaussian broadening alongside dominant Lorentzian components. In order to account for this complication, we can introduce the well-known *Voigt profile*, a convolution of Gaussian and Lorentzian lineshapes (see figure 2.1 for a comparison of Lorentzian, Gaussian, and Voigt profiles). In practice, most of our spectra are dominated by one component or the other (in two-step vapor cell signals, for instance, Lorentzian widths are of order 60 MHz while Gaussian widths tend to be below 10), and a large volume of past work in the Majumder lab indicates that there are no systematic differences in peak center locations between Voigt and Lorentzian fitting.<sup>5</sup> Accordingly, because the process of fitting to Voigt profiles is computationally intensive, we often elect to fit to Lorentzians exclusively. If there is ever doubt that such a decision will lead to systematic discrepancies, however, we have the machinery in place to fit to the fully

---

<sup>5</sup>This result holds largely because both Voigt and Lorentzian profiles are symmetric, so that even fits which fail to perfectly capture the off-resonant behavior of a line will still extract the correct resonance value.

convolved function.

### 2.2.3 Two-Step Spectroscopy

In the present experiment our interest is in a state of indium that cannot be directly accessed from the ground state by an electric dipole (E1) transition ( $5P \rightarrow 7P$  is disallowed by  $\Delta L$  selection rules). Instead, our approach is to excite *two* E1 transitions, first from the ground state to an intermediate  $S$  state ( $5P_{1/2} \rightarrow 6S_{1/2}$  at 410 nm in the present case), and then from this intermediate state to the excited state of interest ( $6S_{1/2} \rightarrow 7P$ , 685-690 nm).<sup>6</sup> Along with allowing us to use two relatively cheap, low-power diode lasers in the experiment (E1 transitions require little power for significant absorption), this technique has the added advantage of eliminating Doppler broadening in the excited spectrum ‘for free.’ In particular, because the blue laser excites only one velocity class of atoms (or rather a small range of velocity classes that fall within the homogeneous linewidth of the transition) at any given time,<sup>7</sup> the red laser *can only* interact with a small range of velocities, so its absorption resolution is no longer Doppler limited.

There is a trade-off here, and it is one of signal size. Because the blue laser only interacts with a few velocity classes at any given time, only about

$$\frac{\Gamma_{\text{Homogeneous}}}{\Delta_{\text{Doppler}}} \sim \frac{25 \text{ MHz}}{1.6 \text{ GHz}} \sim 1.5\% \text{ (vapor cell)} \quad (2.12)$$

of the total atoms in a vapor cell environment are excited to the intermediate state (this number is closer to 20% in the atomic beam, which has a smaller Doppler width). We typically compensate for this effect by using sensitive detection techniques, described in chapter 4, to look for only that part of the red signal that changes with the blue beam present, as only signals in the presence of first-step excitation can result from true two-step spectroscopy.

We conclude with a brief discussion of two-step lineshapes. In particular, we often describe our red absorption signals as consisting of Lorentzians, or Voigt profiles, appearing to neglect the exponential nature of equation 2.7 entirely. We can justify this by noting that optical depths for the second step of a two step transition must be small, given the small number of atoms present in the intermediate state (equation 2.12). Accordingly, equation 2.7 can be expanded to first order in  $\alpha$ :

$$I(\omega) = I_0 e^{-\alpha P(\omega)} \approx I_0 (1 - \alpha P(\omega)) \quad (2.13)$$

so that the transmitted intensity does look like  $P(\omega)$ , up to a DC offset that is eliminated from collected signals because it does not vary with the presence of the 410 nm laser. We will therefore freely refer to the peaks in our two-step spectra as Lorentzians (or otherwise) without worrying about the effects of the true exponential form of absorption resonances.

---

<sup>6</sup>Such a conception of a two-step transition is perhaps a bit naive, but as we will see in chapter 3, it accords well with a certain limiting case of the full quantum mechanical treatment.

<sup>7</sup>Ideally this is always the same velocity class, given a properly locked laser – see section 4.3.2.

# Chapter 3

## Atoms in External Electric Fields

Though the material covered in chapter 2 is sufficient theory to perform a range of spectroscopic experiments, like the hyperfine splitting measurements outlined in appendix E and [17], the present work consists of the study of atoms *under the influence of an external electric field*. This complicates matters considerably: not only do we need to understand the mechanism through which applied fields alter the energetic structure of an atomic sample, but we must also put our simplified picture of a two-step transition under the microscope. We consider the first matter in section 3.1, which addresses the Stark effect, wherein atomic resonances shift under external electric fields. It is to this phenomenon that the *polarizabilities*, whose measurement is the principal aim of this thesis, are intimately related.

The remainder of this chapter considers the many-level quantum systems inherent in our two-step transitions under the influence of electric fields. In the case of the  $7P_{1/2}$  state of indium, this boils down to the study of three-level systems, a standard problem treated extensively in the literature and considered, in the present context, by a previous thesis student in [25]. The  $7P_{3/2}$  state, however, presents the Majumder group with a new set of problems, and it is the treatment of this system (in which we must consider as many as 60 levels!) that concerns us for much of this chapter. With this theory in hand, we ultimately turn to the question of polarizability extraction from the complicated  $7P_{3/2}$  spectra we observe in the lab.

### 3.1 Polarizabilities and the Stark Effect

When we apply an external electric field to a sample of atoms, its effect will be to induce an atomic dipole moment  $\vec{D} = -\sum_i e\vec{r}_i$ , where  $e$  is the magnitude of the electron charge and the  $\vec{r}_i$ 's are electron positions with respect to the nucleus. This imparts an energy correction, called the Stark shift, corresponding to the dipole's orientation with respect to the electric field. For an electric field  $\vec{\mathcal{E}}$ , which we take to be along the  $z$  axis, this leads to a perturbation Hamiltonian

$$H'_{\text{Stark}} = -\vec{D} \cdot \vec{\mathcal{E}} = -D_z \mathcal{E} . \quad (3.1)$$

The electric fields attained in the laboratory (of order 10 kV/cm) are small compared to those internal to the atoms, so we are justified in turning to perturbation theory.<sup>1</sup> The first order correction to the energy of state  $\eta$  goes to zero by parity, since  $\vec{D}$  is odd<sup>2</sup>:

$$E_\eta^{(1)} = -\mathcal{E}\langle\psi_\eta^0|D_z|\psi_\eta^0\rangle = 0 \quad (3.2)$$

and so we move on to second order perturbation theory. This yields an energy correction proportional to the square of the electric field:

$$E_\eta^{(2)} = -\mathcal{E}^2 \sum_{\nu \neq \eta} \frac{|\langle\psi_\nu^0|D_z|\psi_\eta^0\rangle|^2}{E_\nu^0 - E_\eta^0} \equiv -\frac{1}{2}\alpha(\eta)\mathcal{E}^2, \quad (3.3)$$

where

$$\alpha(\eta) = 2 \sum_{\nu \neq \eta} \frac{|\langle\psi_\nu^0|D_z|\psi_\eta^0\rangle|^2}{E_\nu^0 - E_\eta^0} \quad (3.4)$$

is called the polarizability.<sup>3</sup> This is traditionally broken into two components, each of which characterizes a particular type of behavior (see [26, 27] for details). The first is called the *scalar polarizability*:<sup>4</sup>

$$\alpha_0 = \frac{2}{3(2J+1)} \sum_n \frac{|\langle\psi||D||\psi_n\rangle|^2}{E_n - E}, \quad (3.5)$$

where the quantity in the numerator is a reduced dipole matrix element (see appendix B.2.1 on the Wigner-Eckart theorem), and  $J$  is the total electronic angular momentum of the state of interest. It describes state-independent quadratic shifts, through which all hyperfine levels of interest shift by the same amount.

The second term is called the *tensor polarizability*:

$$\begin{aligned} \alpha_2 = & 4 \left( \frac{5J(2J-1)}{6(J+1)(2J+1)(2J+3)} \right)^{1/2} \\ & \times \sum_n (-1)^{J+J_n} \left\{ \begin{matrix} J & 1 & J_n \\ 1 & J & 2 \end{matrix} \right\} \frac{|\langle\psi||D||\psi_n\rangle|^2}{E_n - E}, \end{aligned} \quad (3.6)$$

where the piece in curly brackets is a Wigner 6-j symbol. From here it is immediately apparent that the tensor polarizability goes to zero for states with  $J = 0$  or  $J = 1/2$ .

<sup>1</sup>In particular, the equations below assume that the Stark shift is small compared to the fine structure - certainly the case for the Stark shifts of order several hundred MHz that we observe.

<sup>2</sup>To see this, consider a simplified dipole operator,  $\vec{D} = -e\vec{r}$ , with an electric field along the  $z$  axis, so that  $H'_{\text{Stark}} = -e\mathcal{E}z$ . Then, since the wavefunction has definite parity (i.e. it is either even or odd), the integral goes to zero because  $H'_{\text{Stark}}$  is odd.

<sup>3</sup>This quantity might be familiar from electrostatics. See, for instance, David J. Griffiths, *Introduction to Electrodynamics*, 4th ed. (New York: Pearson, 2013), 168.

<sup>4</sup>Here I have dropped the label  $\eta$  for the state of interest; now  $E$  and  $\psi$  refer to the unperturbed energy and wavefunction of that state, respectively, and the sum is over all those states allowed by electric dipole selection rules. I have also simplified  $D_z$  to  $D$ ; this is still taken to be the component of the dipole operator along the  $z$  axis.

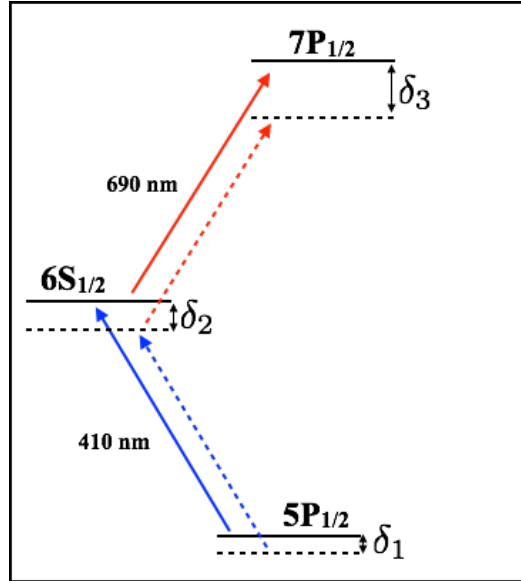


**Figure 3.1:** Effect of the Stark shift on the three-level system associated with our indium  $7P_{1/2}$  polarizability measurements. Note that in the presence of an electric field the red laser frequency shifts down by an amount  $\delta_3 - \delta_2$ , where  $\delta_n = \frac{1}{2}\alpha_0(n)\mathcal{E}^2$  – accordingly, it is really a *difference* of polarizabilities that we observe in the experiment.

This considerably simplifies our Stark shift measurements in the indium  $7P_{1/2}$  state: it admits only scalar shifts (see figure 3.1 for a diagram of these shifts in the  $7P_{1/2}$  three-level system).

What of the  $7P_{3/2}$  state, for which the tensor polarizability is nonzero? It turns out that the tensor polarizability is related to the hyperfine-basis matrix elements of a modified Hamiltonian,  $V_S$ :<sup>5</sup>

$$\langle Fm_F|V_S|F'm_F\rangle = -\frac{1}{2}\alpha_0\mathcal{E}^2\delta_{FF'} - \frac{1}{2}\alpha_2\mathcal{E}^2\langle Fm_F|Q|F'm_F\rangle , \quad (3.7)$$

where the  $Q$  operator is given in [28] and describes hyperfine mixing induced by the Stark effect. The first term includes the effect of the scalar polarizability; it is already diagonal because it shifts each hyperfine level equally. The second term characterizes the Stark mixing between different  $F$  levels.<sup>6</sup> Diagonalizing this matrix to find energy eigenvalues reveals that the magnetic sublevels,  $m_F$ , split under the influence of the applied field (figure 3.2). Accordingly, the  $7P_{3/2}$  state of indium experiences both a large scalar shift and smaller “tensor” shifts that separate once-degenerate sublevels, leading to much more complicated spectra.

<sup>5</sup>This modification is made to allow us to consider hyperfine structure despite the fact that the Stark effect is by no means a small perturbation at that level. Details are found in [28]. See also [29] for more on the application of this hyperfine-basis Stark Hamiltonian.

<sup>6</sup>There is no mixing between states of different  $m_F$  because we take the electric field to lie along the  $z$  axis.

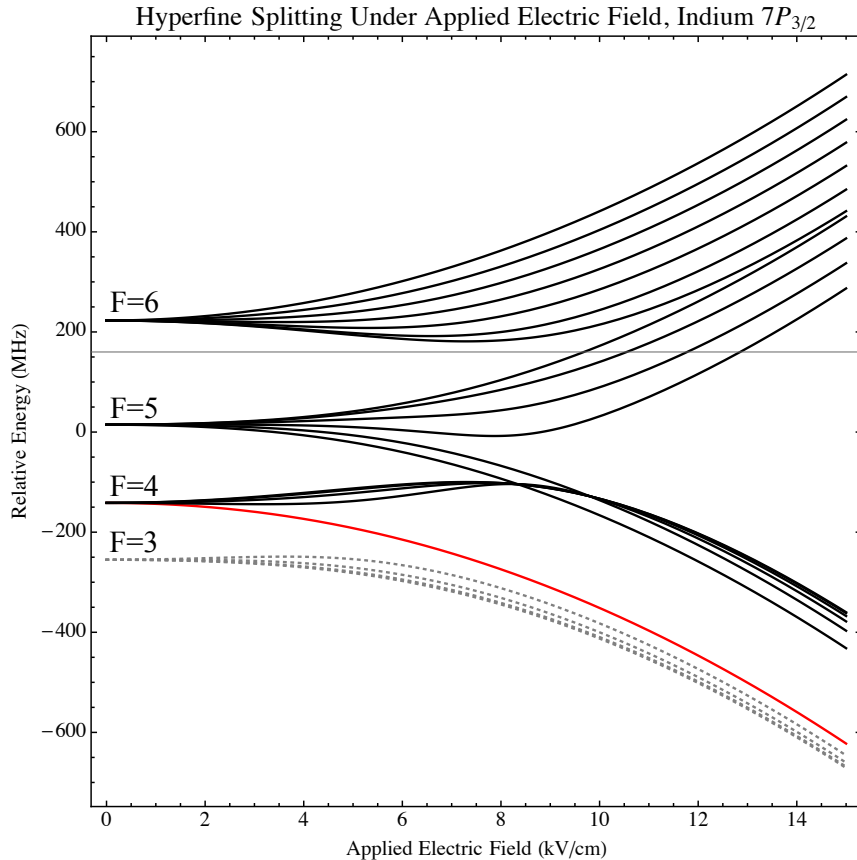


**Figure 3.2:** Splitting of hyperfine sublevels in the indium  $7P_{3/2}$  state under an applied electric field. Here we have subtracted out the effect of the scalar polarizability, leaving just that splitting effected by the tensor piece. In our experiment we excite only the  $F = 4, 5, 6$  levels due to  $\Delta F$  selection rules; accordingly, the  $F = 3$  states (dashed and greyed out in the figure) are not observed. The result is that the  $|F, m_F\rangle = |4, 4\rangle$  level (highlighted in red) becomes individually resolvable at high fields.

## 3.2 The Stark Shift in an N-Level System

Above, we introduced the Stark effect and its associated polarizabilities for a single atomic level. In this thesis, however, we induce transitions between many states of indium, and it is in this section that we address the more complicated quantum mechanics concerning polarizabilities in such multi-level systems. Our goals are two-fold and concern (1) the determination of resonance locations and (2) the simulation of expected lineshapes.

Indeed, though the ‘naive’ picture of two-step spectroscopy implies two wholly independent atomic transitions, the technique really couples all relevant states in a non-obvious way, particularly in the presence of external electric fields. As we will see below, it turns out that the ‘naive’ picture is not totally incorrect given a carefully chosen first-step laser frequency. The two-step lineshapes do, however, differ in general from the pure Lorentzians we would expect from the reasoning in section 2.2.3.

The difficulty of this problem differs dramatically between the two  $7P$  states of indium. In the  $7P_{1/2}$  state, the tensor polarizability goes to zero (equation 3.6), meaning that the various  $m_F$  sublevels are always degenerate, and we can write the problem in terms of a three-level system. Such a system was considered in a previous thesis [25], the results of which we present in section 3.2.1.

The  $7P_{3/2}$  state, because it admits a tensor polarizability, requires that we consider all magnetic sublevels, complicating matters greatly. The treatment of the resulting 60-level system represents a new problem in the Majumder group and is the subject of section 3.2.2.

### 3.2.1 The $7P_{1/2}$ State: Three Levels

Because of the degeneracy of the magnetic hyperfine levels in this tensor-polarizability-free state, we need only consider three levels, corresponding to the relevant ground ( $5P_{1/2}$ ), first-excited ( $6S_{1/2}$ ) and second-excited ( $7P_{1/2}$ ) hyperfine states (we’ll label these  $|1\rangle$ ,  $|2\rangle$ , and  $|3\rangle$ , with unperturbed energies  $E_1$ ,  $E_2$ , and  $E_3$ , respectively). The Hamiltonian for this system in the presence of two near-resonant laser fields (frequencies  $\omega_1$  and  $\omega_2$ ) is derived in appendix B.2.2 using the rotating wave approximation. The result:

$$H_{7P_{1/2}} = \begin{pmatrix} 0 & \Omega_1 & 0 \\ \Omega_1 & -\Delta_1 + (\delta_2 - \delta_1) & \Omega_2 \\ 0 & \Omega_2 & -\Delta_2 - \Delta_1 + (\delta_3 - \delta_1) \end{pmatrix} \quad (3.8)$$

where  $\Omega_1$  and  $\Omega_2$  are the Rabi frequencies of the first- and second-step transitions,  $\Delta_1 = \hbar\omega_1 - (E_2 - E_1)$  and  $\Delta_2 = \hbar\omega_2 - (E_3 - E_2)$  are the laser detunings from the field-free resonances, and  $\delta_1$ ,  $\delta_2$ ,  $\delta_3$  are the Stark shifts of their respective levels (i.e.  $\delta_n = -\frac{1}{2}\alpha_0(n)\mathcal{E}^2$ ).

Our interest is in the probability  $P_3$  of excitation from state  $|1\rangle$  to state  $|3\rangle$ . Its time average (all that our detectors can resolve) is given in [25] by

$$\langle P_3 \rangle = \sum_{j=1}^3 |\langle 3|v_j\rangle\langle v_j|1\rangle|^2, \quad (3.9)$$

where  $|v_j\rangle$  is the  $j$ th eigenvector of the Hamiltonian in equation 3.8.

We can use this result to numerically simulate lineshapes for various choices of  $\Delta_1$ ,  $\Delta_2$ ,  $\Omega_1$ , and  $\Omega_2$ . These lineshapes and the relationship between their centers and the ‘true’ Stark shift ( $\delta_3 - \delta_2$ ) were thoroughly explored in [25] in two regimes: that in which the first-step laser was locked to the *field-free* resonance (i.e.  $\Delta_1 = 0$  always), and that in which the laser was always locked to the *Stark-shifted* resonance (i.e.  $\Delta_1 = \delta_2 - \delta_1$ ). The conclusion? For  $\Delta_1 = 0$ , the relationship between the measured Stark shift and the true Stark shift exhibits a dependence at the  $\sim 4 - 5\%$  level on the ratio  $\Omega_2/\Omega_1$ ; for  $\Delta_1 = \delta_2 - \delta_1$ , the measured and true Stark shift values agree, with no dependence on the (imprecisely-known) Rabi frequencies at our level of precision. It is to this latter regime that the ‘naive’ picture of a two-step transition (figure 3.1) applies; here the observed shift truly corresponds to  $\delta_3 - \delta_2$ . We choose to work in this regime for the present work.

It turns out that an analytical lineshape can be derived in this particular case. The result, which we quote from [25], is

$$\langle P_3 \rangle(\omega) = \frac{2\Omega_1^2\Omega_2^2(\omega^2 + 3(\Omega_1^2 + \Omega_2^2))}{4\omega^4\Omega_1^2 + \omega^2(-8\Omega_1^4 + 20\Omega_1^2\Omega_2^2 + \Omega_2^4) + 4(\Omega_1^2 + \Omega_2^2)^3} \quad (3.10)$$

Plots of this curve are given in figure 3.3 for several values of the ratio  $\Omega_2/\Omega_1$ . While for ratios near 1 the lineshape looks roughly Lorentzian, for smaller values (less than approximately 0.7) the line begins to split into two-peaks. This well-known phenomenon is called the Autler-Townes splitting, and the potential for its presence in our experiment is somewhat concerning. In particular, the  $6S_{1/2} \rightarrow 7P_{1/2}$  dipole matrix element (related to  $\Omega_2$ ) is smaller than the  $5P_{1/2} \rightarrow 6S_{1/2}$  matrix element (related to  $\Omega_1$ ), so that for equal laser intensities we get  $\Omega_2/\Omega_1 \approx 0.36$ , well below the threshold for Autler-Townes splitting.<sup>7</sup> Experimentally we can account for this phenomenon by sending significantly more red than blue power through the atomic beam; for  $\sim 5$  mW of the former and  $\sim 0.5$  mW of the latter (and identical beam waists), this brings the Rabi frequency ratio near 1.1 – safely out of the AT splitting regime.

### Scalar Polarizability and Matrix Element Extraction

In the present regime, wherein the measured red Stark shift is equal to  $\delta_3 - \delta_2$ , extraction of the  $7P_{1/2}$  scalar polarizability is straightforward. We begin by dividing

---

<sup>7</sup>Here we use calculated matrix elements from [8]. It is also worth noting that the qualitative lineshape depends only on this ratio of Rabi frequencies; increasing their overall magnitudes simply widens the profile.

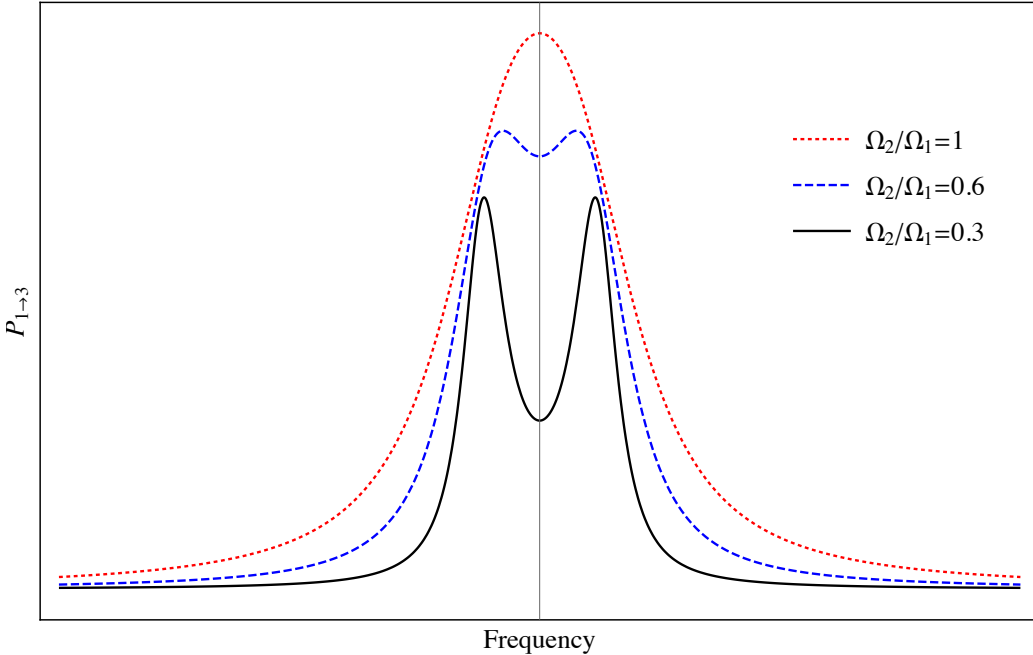


**Figure 3.3:** Plots of the three-level lineshape for excitation from  $|1\rangle$  to  $|3\rangle$  (equation 3.10) for several values of the Rabi frequency ratio,  $\Omega_2/\Omega_1$ . It turns out that, for equal laser intensities,  $\Omega_2/\Omega_1 = 0.3$  roughly corresponds to excitation to the indium  $7P_{1/2}$  state, while  $\Omega_2/\Omega_1 = 0.6$  corresponds to the  $7P_{3/2}$  state.

our measured Stark shifts by the square of the applied field to arrive at the Stark shift constant,

$$k_S \equiv -\frac{\Delta E_{\text{obs}}}{\mathcal{E}^2} = \frac{1}{2}(\alpha_0(7P_{1/2}) - \alpha_0(6S_{1/2})) \quad (3.11)$$

It is this quantity that we will directly measure and analyze for errors in chapter 5. We then convert to the desired polarizability by inverting equation 3.11:

$$\alpha_0(7P_{1/2}) = 2k_S + \alpha_0(6S_{1/2}) = 2k_S + \Delta\alpha_0(6S_{1/2} - 5P_{1/2})_{\text{meas}} + \alpha_0(5P_{1/2})_{\text{theory}} \quad (3.12)$$

where the second term in the rightmost expression was measured in [19] and the last term was calculated in [11].

Examining the sum-over-states definition of the scalar polarizability in equation 3.5 (along with an energy level diagram of indium) reveals that we can, from the polarizability, extract a precise value for the reduced dipole matrix element between the  $7P_{1/2}$  state and the nearby  $6D_{3/2}$  state, whose close energetic proximity means that this particular term contributes  $\sim 97\%$  to the sum.

Rewriting equation 3.5 for the  $7P_{1/2}$  state,

$$\alpha_0(7P_{1/2}) = \frac{1}{3} \sum_n \frac{|\langle n || d || 7P_{1/2} \rangle|^2}{E_n - E(7P_{1/2})}, \quad (3.13)$$

we then invert to solve for the matrix element of interest:

$$\langle 6D_{3/2} || d || 7P_{1/2} \rangle = \sqrt{3|E(6D_{3/2}) - E(7P_{1/2})|C} , \quad (3.14)$$

where  $C$  is the difference between  $\alpha_0$  and the portion of the sum *not* due to the  $6D_{3/2}$  state. Consulting [22], we find that this remaining portion is equal to  $5645(663)\alpha_0^3$ , so that  $C = \alpha_0(7P_{1/2}) - 5645\alpha_0^3$ . Atomic  $D$  states are particularly challenging to model from a theoretical perspective, and so matrix elements like this one are especially helpful in guiding the refinement of theory. They are often very difficult to measure experimentally, so it is remarkable to be able to indirectly attain such a value, with good precision, from Stark shift measurements.

### 3.2.2 The $7P_{3/2}$ State: Sixty Levels

In the  $7P_{3/2}$  state, unlike the  $7P_{1/2}$ , the tensor polarizability is nonzero and leads to a splitting of previously-degenerate magnetic hyperfine sublevels,  $m_F$ . This means that we must account for *all*  $7P_{3/2}$  sublevels if we wish to simulate lineshapes in a manner similar to that of section 3.2.1. Further, because the tensor polarizability mixes hyperfine levels in the  $7P_{3/2}$  state (see equation 3.7), we include all *four* hyperfine levels ( $F'' = 3, 4, 5, 6$ ) in our Hamiltonian (even though E1 selection rules dictate that we can only access three at a time). Finally, if we are interested in relative amplitudes of  $m_F$  levels in the excited state, we must account for  $\Delta m_F$  selection rules from the lower states – accordingly, we also include  $m_F$  sublevels for the ground ( $5P_{1/2}(F = 4)$ ) and intermediate ( $6S_{1/2}(F' = 5)$ ) states.<sup>8</sup> All told, we have  $2F + 1 = 9$  levels from the ground state,  $2F' + 1 = 11$  levels from the intermediate state, and a whopping  $7 + 9 + 11 + 13 = 40$  levels from the excited state. The resulting  $60 \times 60$  Hamiltonian in the presence of two near-resonant laser fields is derived in appendix B.2.2 and generalizes naturally from the  $3 \times 3$  Hamiltonian above. We write it here as a block matrix:

$$H_{7P_{3/2}} = \begin{pmatrix} 0 & \Omega_1 & 0 \\ \Omega_1^\dagger & -\Delta_1 + (\delta_2 - \delta_1) & \Omega_2 \\ 0 & \Omega_2^\dagger & -\Delta_2 - \Delta_1 + (\delta_3 - \delta_1) + \mathbf{V}_{\text{hf}} + \mathbf{V}_{\text{tens}} \end{pmatrix} , \quad (3.15)$$

where the detunings and Stark shifts are defined as in the  $7P_{1/2}$  case (i.e.  $\Delta_1 = \hbar\omega_1 - (E_2 - E_1)$ ,  $\Delta_2 = \hbar\omega_2 - (E_3 - E_2)$ , and  $\delta_n = -\frac{1}{2}\alpha_0(n)\mathcal{E}^2$ ).<sup>9</sup> Components *not* in bold are multiplied by the necessary identity matrix to fill out the Hamiltonian.

The ‘Rabi matrices’,  $\Omega_n$ , quantify laser-induced transitions between states and consist of reduced dipole matrix elements,  $\langle n'L'J' || d || nLJ \rangle$ , multiplied by Wigner 3-j and 6-j symbols designed to pick out the relevant  $|Fm_F\rangle$  states. They are given in

---

<sup>8</sup>We choose these hyperfine levels because they allow the excitation of the  $7P_{3/2}(F'' = 4, 5, 6)$  states only. As seen in figure 3.2, this lets us resolve an individual hyperfine sublevel at high fields.

<sup>9</sup>It is important to note that here  $E_3$  is the field-free energy of the  $7P_{3/2}$  state *in the absence of hyperfine structure*. The hyperfine Hamiltonian in the third diagonal matrix element accounts for hyperfine levels on top of this bare energy.

appendix B by equations B.25 and B.27, as well as the relations  $\Omega_1 = \varepsilon_1 \mathbf{d}_{21}/\hbar$  and  $\Omega_2 = \varepsilon_2 \mathbf{d}_{32}/\hbar$ , where the  $\varepsilon$ 's are the electric field amplitudes of the two lasers.  $V_{\text{tens}}$  is a matrix accounting for the tensor polarizability and is defined (from the second term of equation 3.7) as

$$\langle Fm_F | V_{\text{tens}} | F'm_F \rangle = -\frac{1}{2} \alpha_2 \mathcal{E}^2 \langle Fm_F | Q | F'm_F \rangle . \quad (3.16)$$

Finally,  $V_{\text{hf}}$  accounts for field-free hyperfine structure. Its form, in terms of the  $a$ ,  $b$ , and  $c$  constants (equation 2.6) is given in, for instance, [24].

Here, as with the  $7P_{1/2}$  state, we work in the regime where  $\Delta_1 = (\delta_2 - \delta_1)$  (i.e. the first-step laser is always locked to the Stark-shifted resonance), so that the Hamiltonian (equation 3.15) simplifies to

$$H_{7P_{3/2}} = \begin{pmatrix} 0 & \Omega_1 & 0 \\ \Omega_1^\dagger & 0 & \Omega_2 \\ 0 & \Omega_2^\dagger & -\Delta_2 + (\delta_3 - \delta_2) + \mathbf{V}_{\text{hf}} + \mathbf{V}_{\text{tens}} \end{pmatrix} \quad (3.17)$$

Using this Hamiltonian we can simulate lineshapes according to a modified version of equation 3.9. In particular, the probability of excitation to the  $7P_{3/2}$  state with hyperfine levels  $F''$  and  $m''_F$  is

$$\langle P_{F''m''_F} \rangle = \sum_{j=1}^{60} |\langle F''m''_F | v_j \rangle \langle v_j | 1 \rangle|^2 , \quad (3.18)$$

where the  $|v_j\rangle$  are eigenvectors of the Hamiltonian in equation 3.17. We assume a thermal distribution of states in the atomic beam, so  $|1\rangle$  is a vector representing equal population in each of the nine degenerate ground state sublevels (i.e. 1/3 times a vector with 9 ones followed by 51 zeros).

### 3.3 Extraction of $7P_{3/2}$ Polarizabilities

As figure 3.2 makes clear, the challenge of making polarizability measurements in the indium  $7P_{3/2}$  state is that there are few fully resolved hyperfine sublevels in our spectra for any electric field in an accessible (0-15 kV/cm) range. Rather, at low field ( $\lesssim 2$  kV/cm) we see a level-independent Stark shift down in frequency, accompanied by a splitting of  $m_F$  levels that has the effect of asymmetrically widening our peaks without becoming resolved. Similarly, at higher fields ( $\sim 15$  kV/cm) we see several composite peaks, most of which contain many unresolved sublevels. Accordingly, we must rely on lineshape simulations of the sort detailed above in order to maintain any hope of extracting the desired values.

Using equation 3.18 and a Mathematica program to numerically diagonalize the  $60 \times 60$   $7P_{3/2}$  Hamiltonian (see appendix C), we can simulate the full expected lineshape in both low field and high field regimes. In the former case ( $\mathcal{E} \lesssim 2$  kV/cm)

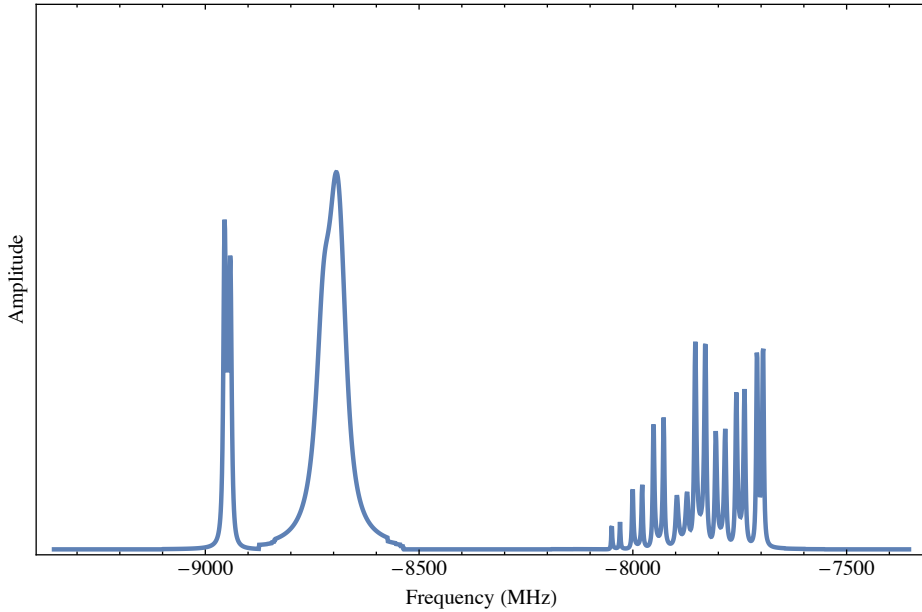


**Figure 3.4:** Simulated atomic beam spectrum for indium  $7P_{3/2}(F'' = 4, 5, 6)$ , with  $\mathcal{E} = 15$  kV/cm and both lasers  $\pi$ -polarized. Note that this spectrum is shifted by over 8 GHz from the field-free case, which is centered around zero on this frequency scale. The leftmost peak here is the resolved  $|4, 4\rangle$  sublevel; it can be used to extract a scalar polarizability. All other sublevels are unresolved.

we arrive at a spectrum consisting of three peaks and many unresolved sublevels. The latter, high-field case yields a more interesting spectrum, shown in figure 3.4 for  $\mathcal{E} = 15$  kV/cm and two  $\pi$ -polarized lasers. It contains three distinct features (which one will note align with expectations from figure 3.2). The first is a wide ‘plateau’ at the high-frequency end of the scan consisting of all  $F = 6$  sublevels and the  $|F, m_F\rangle = |5, 3\dots 0\rangle$  levels. The middle, ‘composite’ peak contains the (unresolved)  $|5, 5\text{-}4\rangle$  and  $|4, 3\dots 0\rangle$  levels. The leftmost peak, meanwhile, is the fully resolved  $|4, 4\rangle$  sublevel.<sup>10</sup>

While it will require significant lineshape simulation work to find any utility in either the ‘plateau’ or the ‘composite’ peak, the resolved  $|4, 4\rangle$  line can be employed immediately in the extraction of polarizabilities. Specifically, if we measure shifts in the location of this peak at various electric fields we can determine the scalar polarizability up to an uncertainty associated with our lack of a precise value for the tensor part; this process is outlined below in section 3.3.1. An experimental measurement of the tensor polarizability, meanwhile, demands a more thorough treatment of unresolved lineshapes; while we have not solved this latter problem, we present one approach in appendix B.3.

---

<sup>10</sup>Sublevels  $\pm m_F$  remain degenerate under the influence of an electric field. If not otherwise specified, when I mention a peak  $|Fm_F\rangle$  it is taken to mean the sum of both degenerate  $|F, \pm m_F\rangle$  peaks.

### 3.3.1 Scalar Polarizability Determination

If we assume a value for the tensor polarizability, finding the scalar part is rather straightforward. In particular, because frequency shifts for varying  $\mathcal{E}$  are fully described by the tensor and scalar polarizabilities together, it is only necessary to consider one peak. The obvious choice is the fully resolved  $|4, 4\rangle$  sublevel.<sup>11</sup>

We can solve for the frequency of this peak as a function of the electric field by diagonalizing the  $m_F = 4$  Hamiltonian given by the Stark (equation 3.7) and hyperfine operators together:

$$\begin{aligned} V_4(\mathcal{E}) &= -\frac{1}{2}\alpha_0\mathcal{E}^2 \\ &+ \begin{pmatrix} \langle 6, 4 | V_{\text{hf}} | 6, 4 \rangle - \frac{1}{22}\alpha_2\mathcal{E}^2 & 2\sqrt{\frac{3}{55}}\alpha_2\mathcal{E}^2 & -\frac{3}{11}\sqrt{\frac{2}{5}}\alpha_2\mathcal{E}^2 \\ 2\sqrt{\frac{3}{55}}\alpha_2\mathcal{E}^2 & \langle 5, 4 | V_{\text{hf}} | 5, 4 \rangle + \frac{1}{10}\alpha_2\mathcal{E}^2 & \frac{1}{5}\sqrt{\frac{6}{11}}\alpha_2\mathcal{E}^2 \\ -\frac{3}{11}\sqrt{\frac{2}{5}}\alpha_2\mathcal{E}^2 & \frac{1}{5}\sqrt{\frac{6}{11}}\alpha_2\mathcal{E}^2 & \langle 4, 4 | V_{\text{hf}} | 4, 4 \rangle + \frac{49}{110}\alpha_2\mathcal{E}^2 \end{pmatrix} \\ &\equiv -\frac{1}{2}\alpha_0\mathcal{E}^2 + V_{\text{tens, hf}}(\mathcal{E}) \end{aligned} \quad (3.19)$$

Analytically diagonalizing this  $3 \times 3$  Hamiltonian proves a bit messy, but luckily there is no need for an analytical solution. After all, our interest is in numerical results, and we already have values for the  $V_{\text{hf}}$  matrix elements at the  $\sim 0.1\%$  level from our summer work (appendix E and [17]), as well as an assumed value for the tensor polarizability.

Accordingly, in order to extract the scalar polarizability, we take data at several electric fields near 15 kV/cm and calculate frequency differences between the field-dependent  $|4, 4\rangle$  peak locations. For electric fields  $\mathcal{E}_1$  and  $\mathcal{E}_2$  and a frequency difference  $\Delta E_{|4,4\rangle}$  between the  $|4, 4\rangle$  peaks at those fields, the scalar polarizability is given by<sup>12</sup>

$$\Delta\alpha_0 \equiv (\alpha_0 - \alpha_0(6S)) = \frac{2(E_4(\mathcal{E}_1) - E_4(\mathcal{E}_2) - \Delta E_{|4,4\rangle})}{\mathcal{E}_1^2 - \mathcal{E}_2^2}, \quad (3.20)$$

where  $E_4(\mathcal{E})$  is the  $F = 4$  eigenvalue of the  $V_{\text{tens, hf}}$  matrix in equation 3.19. Mathematica code for evaluating this equation is given in appendix C.

It turns out that this result has nice properties regarding error propagation. In particular, the  $\sim 16\%$  error in the theoretical value for  $\alpha_2$  [22] corresponds to a 1% error in  $\alpha_0$  given sufficient experimental precision.<sup>13</sup> Accordingly, this allows us to

---

<sup>11</sup>This approach is modeled after one alluded to in [29].

<sup>12</sup>As in the  $7P_{1/2}$  case discussed above, for a first-step laser locked to the Stark-shifted  $5P_{1/2} \rightarrow 6S_{1/2}$  resonance, what we actually expect to measure is the *difference* between the  $6S_{1/2}$  and  $7P_{3/2}$  scalar polarizabilities. Simulations using the  $60 \times 60$  Hamiltonian do, indeed, accord with this expectation to roughly a part in  $10^{-6}$ .

<sup>13</sup>Further, because we are finding differences of peak locations, any difficulties resulting from non-Lorentzian  $|4, 4\rangle$  lineshapes will vanish, since we end up subtracting out any offsets from the ‘true’ peak center (i.e. the energy eigenvalue). We could, alternatively, employ an ‘overlap’ method in the analysis procedure – see chapter 5.

make a precise determination of the scalar polarizability even without a great deal of precision in the tensor part, which is much more difficult to extract.

# Chapter 4

## Experimental Setup and Methods

In this chapter we describe the experimental approach taken, and the apparatus employed, in the present polarizability measurements. The setup builds on the work of a great many previous thesis students; in its present form the experiment is most similar to those carried out in [25, 30], both of which involved two-step measurements in an atomic beam.

The present experiment includes two significant categories of physical component. The first represents parts of the apparatus dedicated to preparation of the atomic samples and electromagnetic fields required to conduct measurements. This includes both a hot vapor cell of indium atoms and a vacuum chamber containing an indium atomic beam and field plates for performing polarizability measurements (section 4.2). The second category consists of the various optical components required to perform spectroscopy in these atomic samples (section 4.3).

### 4.1 Overview of the Experiment

The fundamental concern of this thesis is to measure energy shifts in the indium  $7P$  hyperfine levels under the presence of an external DC electric field. We apply these electric fields (of order several kV/cm) to a beam of hot indium atoms housed in a vacuum chamber and intersect this beam, at the point of applied field, with two overlapped diode lasers. The first laser is locked to the 410 nm (Stark shift-corrected)  $5P_{1/2} - 6S_{1/2}$  resonance using an auxiliary indium vapor cell. The second is scanned over the hyperfine levels of either the 690 nm  $6S_{1/2} - 7P_{1/2}$  or 685 nm  $6S_{1/2} - 7P_{3/2}$  transition to complete a two-step excitation to the state of interest. We monitor this same two-step transition – in the absence of applied fields – in a vapor cell, which serves as a static frequency reference. A Fabry-Pérot cavity is used to monitor the linearity of the second-step laser scan, while 1000 MHz EOM sidebands provide absolute frequency calibration. See figure 4.1 for a schematic diagram of the entire apparatus, the component parts of which will be detailed below.

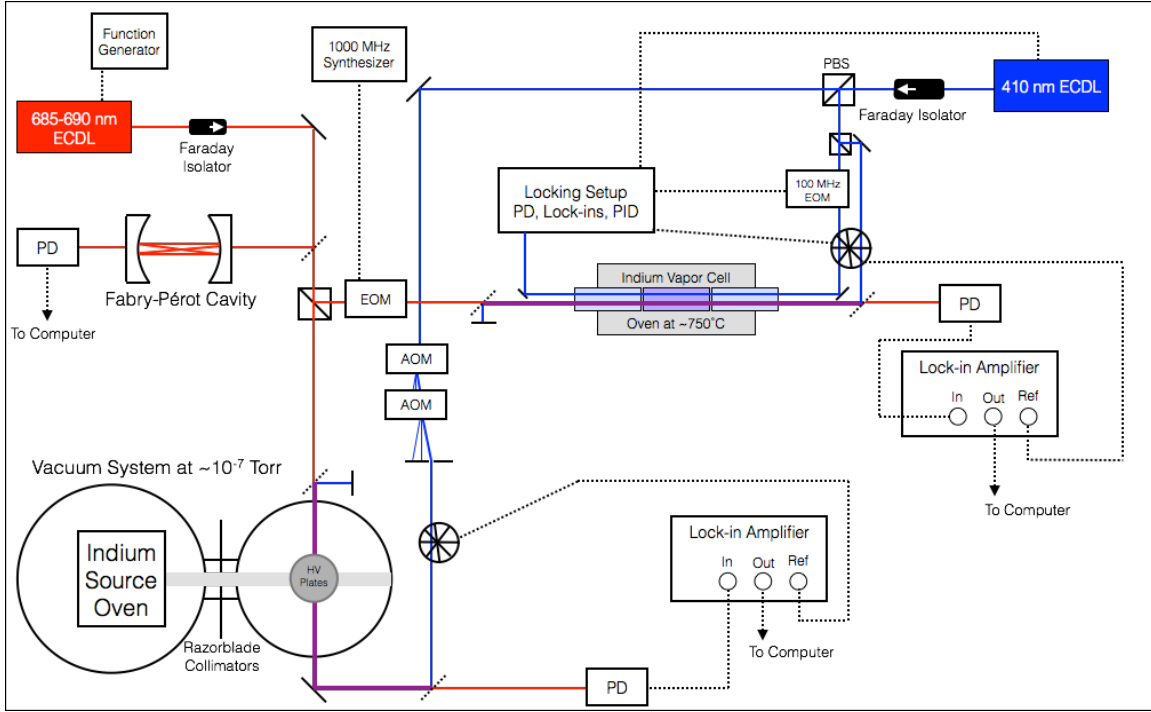


**Figure 4.1:** Simplified diagram of the entire experimental setup. Optical components such as lenses and waveplates have been omitted, and optical paths have been greatly simplified.

## 4.2 Sources of Atoms

### 4.2.1 Indium Vapor Cell

In our polarizability measurements we use two distinct samples of atoms. While we apply electric fields to a beam of indium atoms to actually observe the Stark shift, for diagnostic purposes (to be detailed below) we also probe a second sample of indium atoms under *no applied field*. We produce this sample using a tabletop oven to heat a cylindrical quartz cell containing a small amount of indium metal to roughly 750°C . The resulting atomic vapor is dense enough to allow roughly 80% absorption along the 410 nm  $5P_{1/2} \rightarrow 6S_{1/2}$  first-step transition through the  $\sim 10$  cm-long cell. The absorption line is significantly Doppler broadened, but because of the two-step spectroscopic technique described above (section 2.2.3) such broadening ultimately becomes inconsequential. Vapor cell spectroscopy has been a part of nearly every experiment out of the Majumder group for the past twenty years, and its implementation is by now a near-trivial process.

### 4.2.2 Atomic Beam Unit

The vacuum chamber and oven used to produce and house an indium atomic beam, as well as the metal plates and associated electronics used to produce the well-calibrated

electric fields applied to this beam, together constitute what we call the atomic beam unit (ABU). Though the ABU presents significantly more complications than the field-free vapor cell setup also used in this experiment, those added complications are necessary. Indeed, the presence of a quartz cell might disrupt the uniformity of any electric fields applied to our atoms, dictating that we use an atomic beam. This, in turn, requires vacuum in order to propagate several meters unimpeded; a low pressure environment also helps us avoid electrical breakdown (and catastrophic current flow) between the field plates.

### Vacuum Chamber

The first step in the process of creating the atomic beam is to achieve a vacuum. We do this in a homebuilt metal chamber used over the course of many past theses. The unit contains two large vertically cylindrical sections, connected by a smaller ‘tube’ through which the atomic beam travels. The first section contains the oven used to produce the beam, while the second contains the electric field plates and laser interaction region. We create the vacuum using two devices: the first is a mechanical ‘roughing’ pump (physically contained in an adjacent room) that takes the chamber from atmospheric pressure to  $\sim 10^{-3} - 10^{-4}$  Torr. The second is a set of two diffusion pumps with an associated liquid nitrogen trap, used to remove residual gas from the chamber. These typically bring pressures down to  $\sim 10^{-7} - 10^{-6}$  Torr (monitored with a Bayard-Alpert ionization gauge), even with the indium source oven running at or above 1100°C . At such pressures the mean free path of indium atoms is of order tens to hundreds of meters, and so we need not achieve better vacuum.

### Indium Beam Source and Collimation

In one side of the vacuum chamber is housed a homebuilt oven used to heat indium metal to  $\sim 1100^\circ\text{C}$  and create the beginnings of an atomic beam. The oven consists of an inner ceramic cylinder surrounded by clamshell heaters and various layers of metal and water cooling. We use a standard PID feedback circuit (and a thermocouple inserted next to the clamshell heaters) to stabilize the temperature. For more on the design and construction of the oven, see [31].

Containing the heated indium metal is a molybdenum crucible placed inside the inner ceramic cylinder. Molybdenum, with its melting point of 2623°C , is chosen because of its exceptional compatibility with this high-temperature, low-pressure application. On the front of the crucible is fastened a plate containing a series of thin vertical slits whose job it is to begin to collimate the beam by selecting atoms with near-zero transverse velocities.

Past experiments have used a relatively small crucible that holds at most  $\sim 125\text{g}$  indium. Because of the low line strengths associated with the present experiment, however, we have found it desirable to run at higher temperatures, naturally exhausting this limited supply of indium more rapidly. Accordingly, under the direction of Michael Taylor in the Williams machine shop we designed and built a new, larger

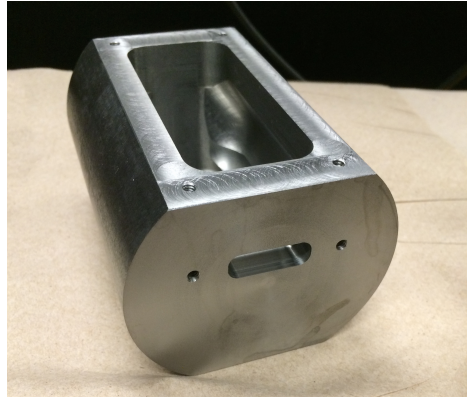


**Figure 4.2:** The body of a new, high-volume molybdenum crucible used to hold ABU source indium. Before putting it in the chamber we attach a collimating faceplate, fill with  $\sim 250$  g indium metal, attach a top cover, and fasten on a thermocouple for temperature monitoring.

molybdenum crucible designed to hold up to 300g indium, therefore doubling the effective lifetime of the atomic beam.

Experimental physics never proceeds precisely as expected, and the first version of this ‘improved’ crucible rather extravagantly proved the point. The crucible was constructed by milling out a solid block of molybdenum through the back and then closing that face by screwing on another plate of the metal. It turns out that such a method does not produce an adequate seal, and run number one of the new crucible resulted in the quick deposition of 250g of indium on the bottom of the vacuum chamber.<sup>1</sup> Our newest crucible was therefore milled out from the top and has allowed us to run the atomic beam with as much as 250g of initial indium (figure 4.2).

After passing through the collimating faceplate of the crucible the beam continues through a set of fine-tunable razor-blade collimators and then through a fixed rectangular aperture (as well as a chopper wheel, whose role will be discussed later) before reaching the field plates and laser interaction region. The result is to collimate the beam to a Doppler width of  $\sim 100$  MHz – certainly not perfect, but nonetheless significant compared to the  $\sim 1.5$  GHz Doppler widths observed in a vapor cell. Figure 4.3 shows a diagram of the vacuum chamber and beam production apparatus.

### Electric Field Production and the Interaction Region

At the heart of the experimental apparatus is the roughly 0.5 cm long, 2 cm wide section of the atomic beam where it interacts with orthogonally-incident laser radiation in an external electric field to produce a field-dependent absorption profile (figure 4.4). We create the field using a set of 10-cm diameter circular metal plates separated by roughly  $d = 1$  cm, across which is applied a large voltage,  $V$ . This leads to an

---

<sup>1</sup>This event will henceforth be known as the Great Indium Catastrophe of 2017.

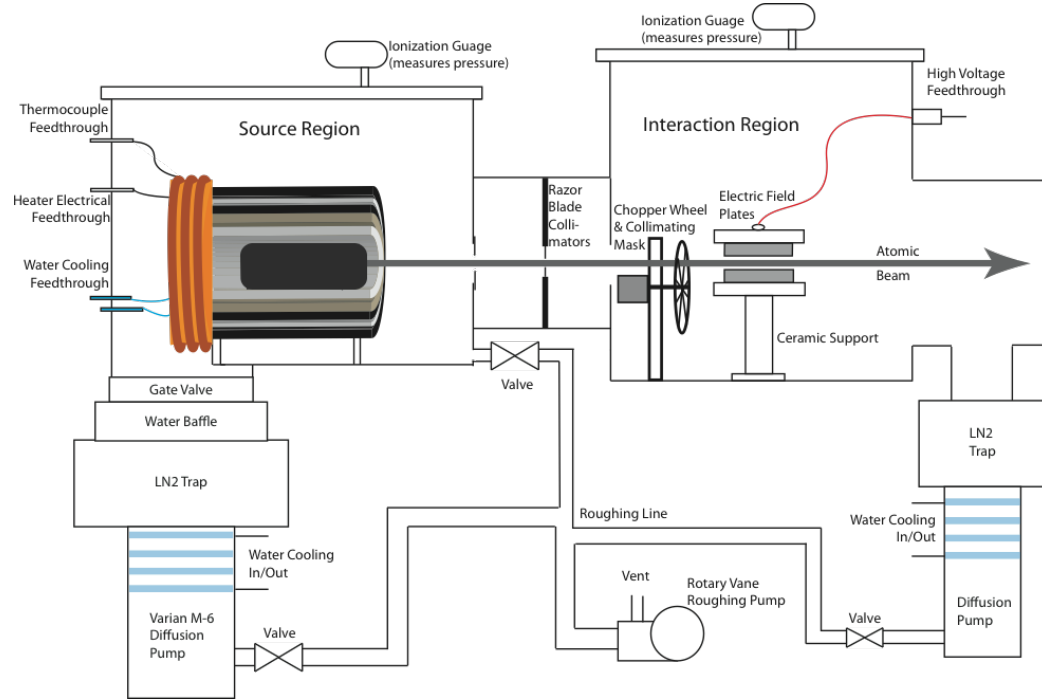


**Figure 4.3:** Diagram of the vacuum system and beam production apparatus. Reproduced, with minor modifications, from a figure in [32, 33].

electric field according to the familiar relation for a parallel-plate capacitor,

$$\vec{E} = \frac{V}{d} \hat{z}, \quad (4.1)$$

at least in the central region of the plates where the interaction occurs and where we can ignore edge effects.<sup>2</sup>

We create this field using a commercial high voltage supply (Glassman High Voltage, Model PS/ER40P07.5XX0) and measure it with a precisely calibrated<sup>3</sup> factor-of-1000 voltage divider (Ross Engineering VD45-0-BDX-LD-ALF) and a calibrated 6½ digit voltmeter (Keithley 2100 series). Combined, this system enables us to measure the voltage to roughly a part in  $10^5$ , therefore causing it to be of negligible significance in our later consideration of systematic errors. For more on the high voltage system see [33].

The separation between the electric field plates,  $d$  in equation 4.1, is not so precisely known as the voltage and is therefore the dominant source of error in determination of the electric field. Using a CNC mill in the Williams machine shop, we were able to measure the separation of our plates to better than a part in  $10^{-3}$ ; the most

<sup>2</sup>A simple implementation of the ‘relaxation’ method to solve Maxwell’s equations shows that the assumption of uniformity is, indeed, valid (at the level of precision we care about) over the region in which the interaction occurs.

<sup>3</sup>Accredited as of February 2017.

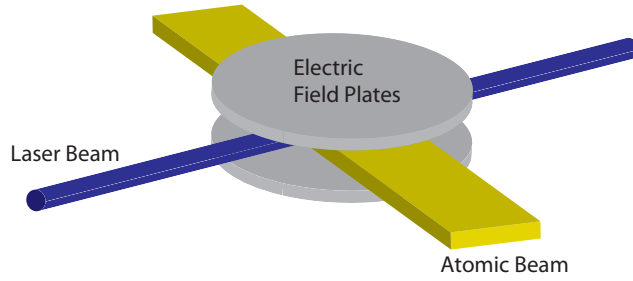


**Figure 4.4:** Diagram of the interaction geometry between the atomic beam, incident laser radiation (two beams), and electric field plates. Reproduced from [25, 30, 33].

recent measurement (made shortly before we began data collection) gave a value of  $d = 1.0038(5)$  cm.

Following the standard propagation of errors formula, we note an error in the electric field (from equation 4.1) of

$$\delta E = \sqrt{\delta V^2 + \delta d^2} , \quad (4.2)$$

where the  $\delta$  represents a fractional uncertainty. Given  $\delta d \approx 5 \times 10^{-4}$  and  $\delta V \sim 10^{-5}$ , it is clear that the error in the plate separation measurement accounts for nearly all the uncertainty in the electric field. Because Stark shift measurements depend on the *square* of the electric field, we include twice  $\delta E$  in our final error budget.

### 4.3 Optical Setup

The optical setup of the present thesis builds on that of [25, 30] with modifications intended to improve the quality of the atomic beam signal. The most significant challenge of the current  $7P$  polarizability work as compared to previous work on the  $6P_{1/2}$  state involves relative signal size: theory calculations suggest that the  $6S_{1/2} - 6P_{1/2}$  line strength is a factor of 30 stronger than the  $6S_{1/2} - 7P_{3/2}$  transition and a full 75 times stronger than the  $6S_{1/2} - 7P_{1/2}$  transition [8]. Given the rather modest signal-to-noise ratios observed in the atomic beam on that former, much stronger transition in [13, 25, 30], it was clear from the outset that significant modifications to the apparatus would be required to resolve the much weaker transitions to be studied in the present thesis. As such, while the sections below detail the entire optical apparatus, we will focus particularly on the changes made to allow these order-of-magnitude improvements in the ABU signal-to-noise resolution.

### 4.3.1 External Cavity Diode Lasers (ECDLs)

External cavity diode lasers (ECDLs) work well in the context of the measurements undertaken in the Majumder lab because they are easily tunable (our lasers can typically scan over  $\sim 5$  GHz in a single mode), are inexpensive, and provide enough power ( $\sim 10$  mW) for the relatively strong E1 transitions we typically study.

Though greater detail can be found in [34], it is worth briefly noting the way in which these lasers work. As the name might suggest, the gain medium is a semiconductor diode (InGaN for the 410 nm laser, AlGaInP for the 685-690 nm laser). While the diode itself has a cavity that will permit lasing, ECDLs (in the Littrow configuration, as are our lasers) contain a diffraction grating placed 1-3 cm from the diode. While zero order diffraction from the grating forms the output beam, first order diffraction is reflected back into the diode to allow for lasing at a frequency selected in part by the grating. Adjusting the grating changes the cavity length and diffraction wavelength in such a way as to tune the laser frequency. An attached piezo electric transducer (PZT) allows for small adjustments, and in this way we can use a variable voltage source to effect finer tuning (say, for frequency stabilization – see section 4.3.2) or to scan over several GHz by connecting the voltage supply to a function generator.

The first of the two lasers used in the present experiment is a commercially produced 410 nm ECDL in the Littrow configuration (Toptica DL 100). The second is a homebuilt Littrow ECDL that roughly follows the design outlined in [35, 36]<sup>4</sup> and was constructed by Sauman Cheng '16 in 2015 (see [34] for more details on the laser and its construction). The latter laser has previously been used at 671 nm and 655 nm, and the diode used in the present experiment (ThorLabs HL6750MG) allows it to operate at both 690 nm and 685 nm.

### 4.3.2 410 nm Laser Locking and Stark Shift Correction

An essential first step in the two-step spectroscopic technique used in this thesis is to lock our first-step, 410 nm diode laser to the  $5P_{1/2} \rightarrow 6S_{1/2}$  resonance.<sup>5</sup> Indeed, free-running diode lasers tend to drift hundreds of MHz over time scales of several minutes. This results in the excitation of many velocity classes – therefore altering the relative locations of second-step resonances – over the course of a single red laser scan. Our goal is to determine these relative peak locations to within roughly one MHz on any given scan, so blue laser drifts of tens of MHz over the course of a scan lead to unacceptably large systematic errors.

Though we must prevent these sorts of long-term drifts, as well as large short-

<sup>4</sup>Thanks go to Prof. Charlie Doret '02 for introducing the lab to this design.

<sup>5</sup>In reality, of course, we must take into account hyperfine structure. Over the course of the present thesis we typically locked to the  $5P_{1/2}(F=4) \rightarrow 6S_{1/2}(F'=5)$  resonance because of the desirability of accessing the  $F'' = 4, 5, 6$  levels of the  $7P_{3/2}$  state. Nonetheless, for  $7P_{1/2}$  measurements we can just as well lock to the first-step  $F = 5 \rightarrow F' = 4$  resonance; this is a mere 20 GHz away – easily accessible by the 410 nm laser – and can be used in systematic error searches.

timescale fluctuations, we nevertheless do not require an extraordinarily tight lock. Indeed, given the  $\sim 1$  MHz precision aimed for in the experiment, we simply need a lock whose instability will not contribute to errors above this level; a typical goal for laser locks in the Majumder group is about 0.5 MHz RMS. RMS fluctuations of this size will tend to quickly average out over timescales of one scan, and so their only contribution is to negligibly increase the size of statistical errors. In principle, such a lock will also eliminate long-term laser drifts. Any residual effect should at least be small over the  $\sim 20 - 30$  seconds it takes to complete a second-step scan, and we can account for any remaining systematic associated with this drift by separately considering two directions ('upscans' and 'downscans') of red laser frequency sweep.

Though many locking mechanisms employ a stable Fabry-Pérot cavity, our desire to lock precisely on the indium  $5P_{1/2} \rightarrow 6S_{1/2}$  resonance suggests that we instead use an indium vapor cell and lock directly to the observed absorption line. As discussed in chapter 2, the 410 nm absorption lineshape is a Doppler-broadened Gaussian; as an even function about the desired lock point it is unhelpful, for an increase in transmitted light tells us nothing about which way the laser has drifted in frequency. Accordingly, we wish to derive some sort of *odd* function from this absorption line. Something that looks like its derivative is especially convenient, for then locking to the zero crossing ensures a laser precisely on resonance.

While there are several ways to achieve this,<sup>6</sup> ours involves frequency-modulation (FM) spectroscopy, a technique typically used as a sensitive detection scheme (see, for instance, [19, 33]) but which also happens to be well-suited to the present effort. We send a portion of the 410 nm laser beam, frequency  $\omega_c$ , through an electro-optic phase modulator (EOM) driven at  $\omega_m = 2\pi \times 100$  MHz, pass the modulated beam through a  $\sim 750^\circ\text{C}$  indium vapor cell, and demodulate the detected signal<sup>7</sup> at  $\omega_m$  using an RF lock-in amplifier.<sup>8</sup> The resulting lineshape is derived for low modulation depths in [25] and looks like

$$I_{\text{demod}} \propto T^2(\omega_c + \omega_m) - T^2(\omega_c - \omega_m), \quad (4.3)$$

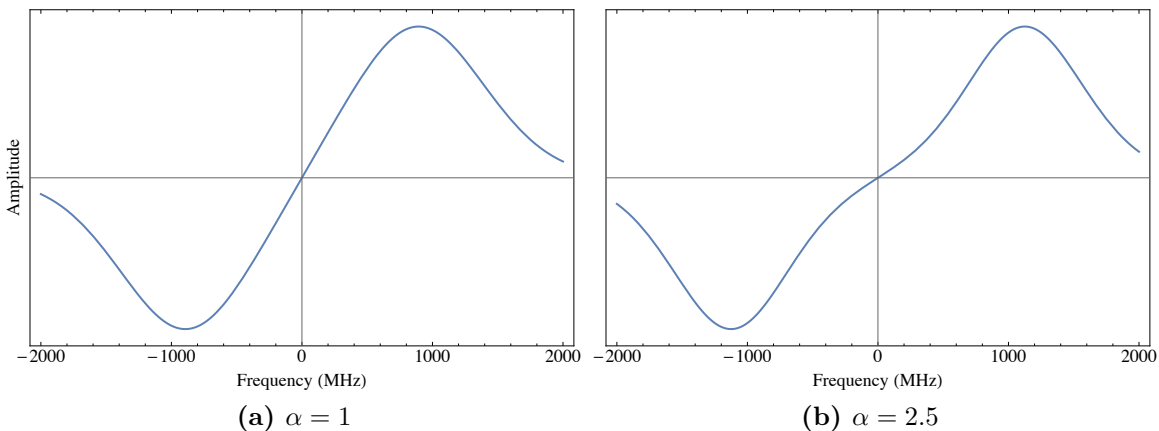
where  $T^2(\omega)$  is the transmitted intensity profile of unmodulated laser light (in this case a Doppler-broadened Gaussian).

Figure 4.5(a) shows a simulation of this signal in the vapor cell for a 'standard' optical depth of  $\alpha = 1$ ; figure 4.5(b), meanwhile, shows the signal for  $\alpha = 2.5$ . As the figure makes clear, the magnitude of the locking slope decreases for increasing optical depths. Because we use the same vapor cell for field-free two-step spectroscopy (see section 4.3.3), this results in a trade-off regarding cell temperature: for larger temperatures we achieve a better two-step signal but a looser lock, and vice-versa. We ultimately choose an oven temperature ( $790^\circ\text{C}$ ) that gives  $\sim 80\%$  absorption ( $\alpha \approx 1.6$ ); this yields as large a two-step signal as possible without venturing unacceptably far into the slope-reducing regime of figure 4.5(b).

---

<sup>6</sup>See [16] for one method used in hyperfine splitting measurements in the Majumder group.

<sup>7</sup>We use a New Focus Model 1601, 1 GHz bandwidth photoreceiver to detect the high frequencies



**Figure 4.5:** Simulations of the demodulated FM 410 nm locking lineshape for experimental vapor cell parameters ( $\omega_m = 100$  MHz and Gaussian width  $\Delta \approx 1.6$  GHz) and two values of the optical depth,  $\alpha$ . Note how increasing optical depth (by increasing temperature) results in a decrease in the locking slope at the zero-crossing lock point.

It turns out that this FM method, all by itself, does not provide a robust enough lock for our purposes. As alluded to above, what we care about is the *slope*, expressed in units of V/MHz, of the locking signal; this allows us to convert from demodulated voltage to frequency. For two equally good locks in voltage space, the one with the larger slope will result in a better frequency-space lock, so we'd like to achieve as steep a slope as possible.<sup>9</sup>

Through what amounted to a happy accident, we discovered that an exceedingly simple way to achieve this was to pass the already-modulated blue beam through an optical chopper, frequency  $\omega_{\text{chop}}$ , before the vapor cell. Demodulation at  $\omega_m$  leaves a signal that looks like that of figure 4.5 multiplied by a square wave at  $\omega_{\text{chop}}$ . Using an analog lock-in, we then demodulate *this* signal at  $\omega_{\text{chop}}$ ; with the proper choice of phase, this picks out the nonzero segments – namely, the desired locking signal – amplifying it in the process to yield a larger slope.<sup>10</sup> A schematic of the complete locking setup is given in figure 4.6, and the observed signal is shown in figure 4.7.

Having achieved a suitable linear signal, we actually effect the lock by feeding this signal into a proportional-integral-differential (PID) controller. Its output, a correction intended to efficiently keep the signal at zero, is input directly to the 410 nm laser's PZT driver, thereby using the ECDL's diffraction grating to stabilize its

inherent in this modulated signal.

<sup>8</sup>Stanford Research Systems SR844.

<sup>9</sup>Admittedly, there is often a trade-off between size of slope and quality of voltage-space lock, so that the quality of the *frequency* lock remains unchanged. Nonetheless, the technique described above exhibits no signs of this less-than-ideal behavior.

<sup>10</sup>To be fair, this is an awfully roundabout way of achieving simple signal amplification. That said, it happened to be convenient for our purposes because of the presence of an unused lock-in in the lab and a chopper wheel (used for the two-step vapor cell signal in section 4.3.3) that was already in the immediate vicinity of the locking beam.

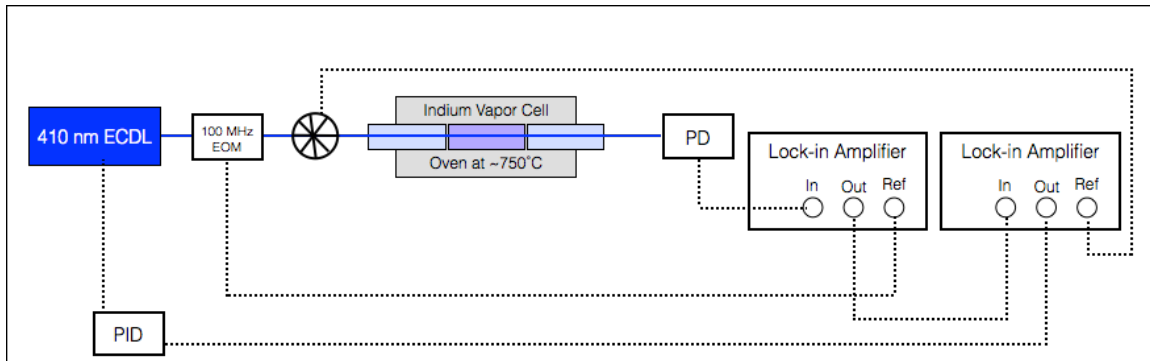


**Figure 4.6:** Schematic diagram of the 410 nm locking setup.

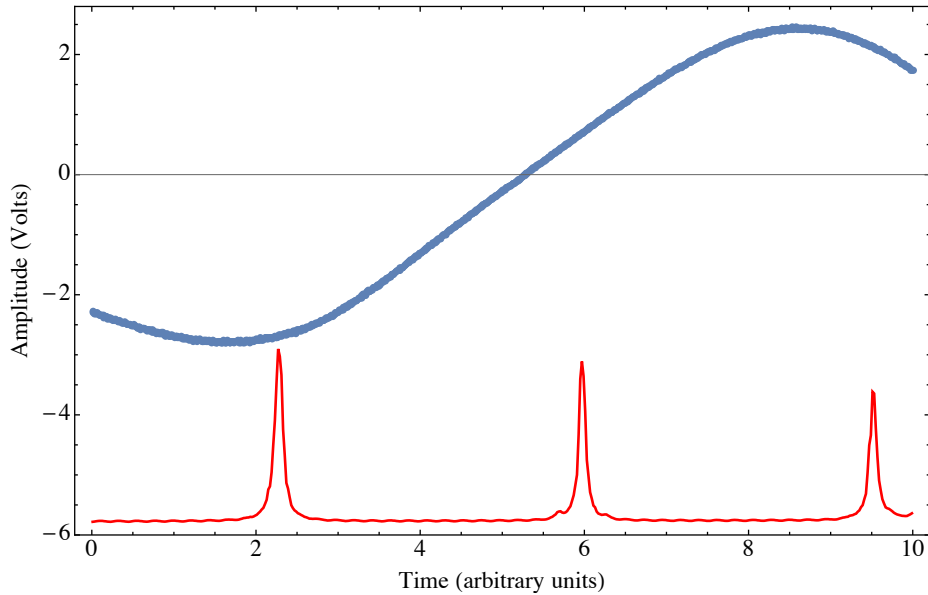


**Figure 4.7:** Observed FM locking signal, along with Fabry-Pérot calibration reference. Using the known value (1000 MHz) of the Fabry-Pérot's free spectral range (FSR), we can calibrate the slope of the locking signal. Here we get roughly 0.25 MHz/mV.

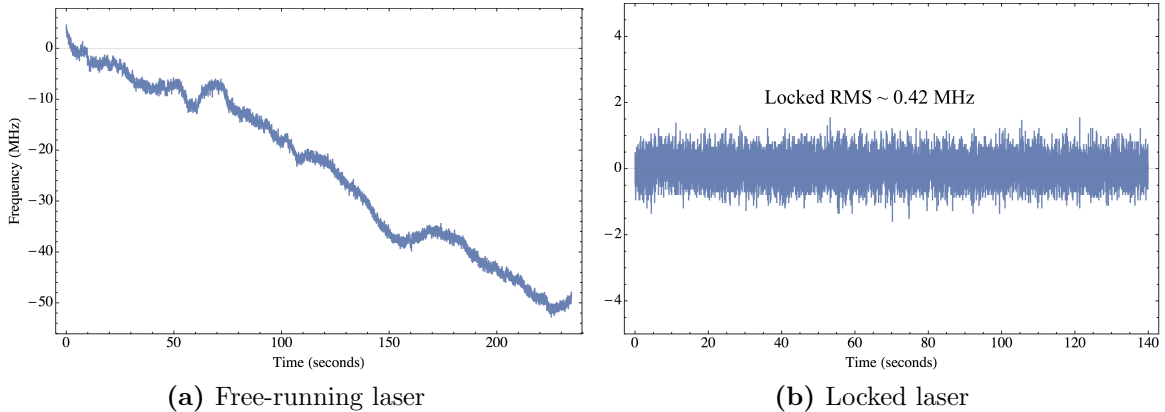


**Figure 4.8:** Locked and unlocked ‘error signals’ for the 410 nm laser. Note carefully the different y-axes for the two plots. The unstabilized laser drifts about 50 MHz over the course of four minutes, while the locked laser exhibits RMS noise fluctuations under 0.5 MHz.

frequency. As shown in figure 4.8, our lock reduces free-running drifts of order 100 MHz to an RMS noise level around 0.5 MHz.

### Stark Shifted Lock Correction

The locking method detailed above is excellent for keeping our 410 nm laser locked to the *unperturbed* indium  $5P_{1/2} \rightarrow 6S_{1/2}$  resonance, but turning on an electric field shifts the location of this resonance, so that our field-free stabilized laser no longer drives zero-velocity-class atoms in the atomic beam. As discussed in section 3.2.1 above, this leads to unacceptable dependences on imprecisely-known Rabi frequencies; we must therefore correct for this shift in the portion of the 410 nm beam sent to the ABU.

A robust method of doing this was developed in [30] and employed in a recent Majumder group measurement of the indium  $6P_{1/2}$  Stark shift [13]. In brief, we pass the ABU portion of the 410 nm laser through two  $\sim 250$  MHz acousto-optic modulators (AOMs, Isomet model 1250C-829A) in succession. With the electric field off, each is driven at precisely 250 MHz; we thus pick out the +1 order beam from the first AOM, pass it through the second AOM, and send the -1 order beam, now back at the original laser frequency, to the atomic beam. With the electric field *on*, however, we need to decrease the blue frequency by an amount (using the first-step

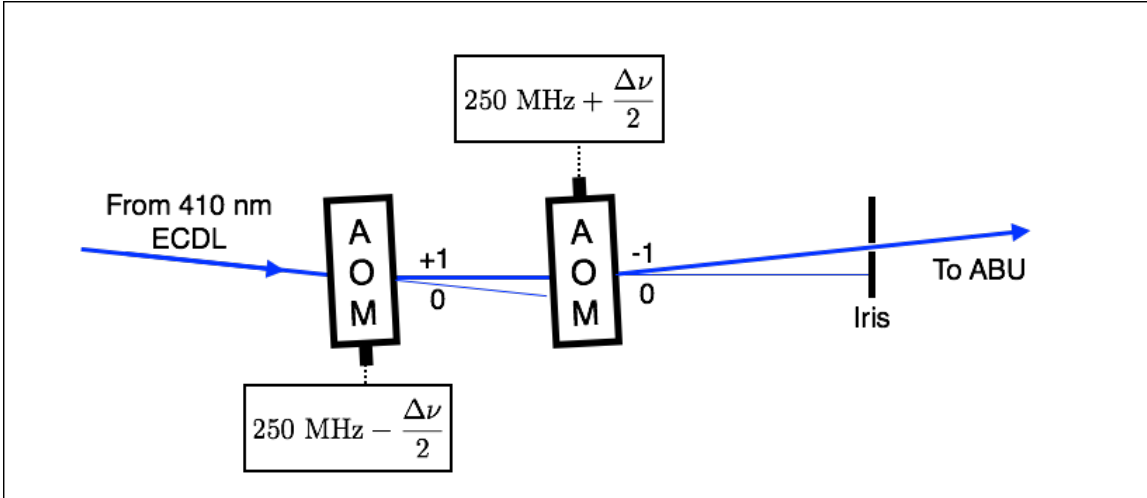


**Figure 4.9:** AOM setup for Stark-shifted locking frequency correction. Note that the angle between the 0 and  $\pm 1$ -order beams scales linearly with AOM drive frequency, so that, as  $\Delta\nu$  becomes nonzero, a decrease in angle between the 0 and +1-order beams at the first AOM is roughly canceled by a parallel increase at the second. Measurements of the physical position of the beam after passing through the ABU confirm that the change in angle between field-on and field-off configurations is indeed negligibly small (it might induce a Doppler shift of  $\sim 0.1$  MHz).

Stark shift measured in [19])<sup>11</sup>

$$\Delta\nu = -k_S \mathcal{E}^2 = -0.12292 \mathcal{E}^2 . \quad (4.4)$$

We can achieve this by *decreasing* the frequency of the first AOM by  $\Delta\nu/2$  and *increasing* the frequency of the second AOM by  $\Delta\nu/2$ . Each AOM thus effects one-half of the desired Stark shift correction, and the beam sent to the ABU remains resonant with the perturbed first-step transition. We have extensively tested the effectiveness of this shift mechanism,<sup>12</sup> finding that the system can shift the blue frequency by at least 40 MHz (the correction required for an 18 kV/cm field) to within 1 MHz of the desired value.

There remains the question of AOM alignment – after all, the diffraction angle of output beams is frequency-dependent. Our solution, shown schematically in figure 4.9, leads to the cancellation, at least at first order, of such frequency-dependent misalignments. Because the applied fractional corrections to AOM frequency are small, any residual misalignment will be negligibly small.

<sup>11</sup>One might worry that the error bar on this value (at the 0.2% level) might contribute a systematic due to our inexact knowledge of the first-step lock correction. To consider this effect we simulate a signal with such a discrepant lockpoint using the machinery of section 3.2.1 and a Mathematica program described in appendix C. We find for fields below 5 kV/cm that the systematic contribution to the Stark shift is well under 0.01 MHz and can accordingly be neglected at our level of precision.

<sup>12</sup>The process, in brief, was to reference the AOM-shifted Fabry-Pérot signal to an unshifted vapor cell resonance.

### 4.3.3 Vapor Cell Reference

Though the meat of the experiment is contained in the atomic beam, it is useful to also monitor two-step excitation to the indium  $7P$  states in a vapor cell. While we cannot apply an electric field to our cell and accordingly only observe an unshifted signal, doing so gives us a much more forgiving (i.e. much higher indium density) environment with which to monitor the two lasers involved in the experiment, and it also supplies an absolute frequency reference from which to measure Stark shifts in the ABU.

The setup represents a rather direct implementation of the two-step spectroscopic method outlined in section 2.2.3. We first chop a collimated portion of the 410 nm laser beam, locked to the  $5P_{1/2} \rightarrow 6S_{1/2}$  resonance as described above, at  $\sim 1$  kHz and align it through the cell. From the opposite direction,<sup>13</sup> we send in a collimated red laser beam, modulated by an EOM at 1000 MHz and precisely overlapped with the blue beam. We scan the red laser over the relevant hyperfine states of either the 690 nm  $6S_{1/2} \rightarrow 7P_{1/2}$  or 685 nm  $6S_{1/2} \rightarrow 7P_{3/2}$  transition. Finally, we detect the red transmission and demodulate with a lock-in amplifier<sup>14</sup> at the blue chopper wheel frequency, picking out only that portion of the light that has interacted with atoms excited to the intermediate state by the 410 nm laser. The result is a Doppler-free spectrum showing the hyperfine structure of the relevant  $7P$  state – two peaks ( $F'' = 4, 5$ ) for the  $7P_{1/2}$  state or three peaks ( $F'' = 3, 4, 5$  or  $4, 5, 6$ , depending on first-step hyperfine transition) for  $7P_{3/2}$  – as well as  $\pm 1000$  MHz frequency sidebands, owing to the red beam’s earlier EOM modulation (see figure 5.1 in the following chapter for a sample spectrum).

The vapor cell spectrum serves several purposes in the context of our experiment. For one, it is a convenient tool in the process of setting up the apparatus and looking for atomic beam signals on a day-to-day basis. Because of the vapor cell’s relatively high optical depths, the signal is fairly easy to observe. Finding this signal, then, is a first step in tuning up the lasers on an everyday basis, and its presence on the oscilloscope tells us that the lasers are functioning properly. It also indicates where in the red laser scan range we should look to find the atomic beam peaks (with the electric field off, the ABU signal is roughly overlapped with that of the vapor cell).

The vapor cell spectrum is also used at various stages of the analysis process. For one, the 1000 MHz sidebands in the signal serve as a frequency calibration reference, thereby playing a crucial role in guaranteeing that the Stark shifts we quote are properly calibrated. Further, because the vapor cell spectrum remains unchanged when we turn on an electric field in the ABU, we can use one or more of its hyperfine peaks as a stable frequency reference from which to measure the Stark shift. For more on both of these processes, see chapter 5.

---

<sup>13</sup>This amounts to what, in a hyperfine splitting measurement like [16] or the past summer’s work, we would call a ‘counter-propagating’ geometry. While the results should not depend on whether we use this or the alternative ‘co-propagating’ configuration, we observe that the former gives sharper, better resolved peaks.

<sup>14</sup>Stanford Research SR810.

### 4.3.4 Atomic Beam Signal

At the heart of our experiment is the necessity of observing an inherently weak transition<sup>15</sup> in a weak sample of atoms in the atomic beam (first-step optical depth  $\alpha \sim 10^{-3}$ ). While the previous version of this experiment [13, 25, 30] employed an extension of the FM spectroscopic scheme used in our locking system to detect small signals from the ABU, our solution to the problem of detecting a yet-smaller signal was to *simplify* the apparatus. Indeed, the present setup dispenses with FM spectroscopy altogether and turns instead to the single-chopper-wheel scheme used in the vapor cell. In particular, modifications made to the apparatus of [13, 30] are as follows:

1. Eliminate FM spectroscopy in favor of a simple chopper wheel approach. While FM techniques should, in principle, lead to better signal detection, it appears that the electronics involved in that setup actually introduced more noise into the spectrum while achieving negligible signal gain.
2. Switch from a chopper wheel in the atomic beam to an external optical chopper, modulating the 410 nm first-step laser beam rather than the source of atoms itself. Because of the difficulties associated with operating a motor under vacuum, the atomic beam-chopper was roughly a factor of two noisier than its optical counterpart. A previous locking system, in which we locked directly to the first-step ABU signal, required this chopper wheel, so this alteration also dictated that we switch to a vapor cell lock.
3. Switch from ‘co-propagating’ laser geometry to ‘counter-propagating’ geometry – i.e. send the blue and red laser beams through the atomic beam in *opposite* directions. Experimentally we observe (and have noticed for some time) that the latter geometry results in taller, narrower peaks than its counterpart.
4. Switch from focused to collimated laser light through the atomic beam. This modification makes some deal of sense, since a collimated beam will interact with more atoms than its focused counterpart. Because of the low density of atoms in the atomic beam, this results in an appreciable change in absorption (most of a focused beam will go unabsorbed because the transition quickly saturates for so few atoms). We estimate that this improved the signal size by at least a factor of two.

The resulting setup is nearly identical to that of the vapor cell. In brief, we chop a beam of  $\sim 0.5$  mW locked, Stark-shift-corrected (see section 4.3.2) 410 nm light at  $\sim 1$  kHz before collimating and sending it through the indium atomic beam. From the opposite side of the ABU, we send in a  $\sim 5$  mW collimated red laser beam, tuned to the proper second-step resonance and precisely overlapped with the counter-propagating blue beam. We then detect this red light with a 10 MHz bandwidth

---

<sup>15</sup>As electric dipole transitions go, at least.

silicon photoreceiver,<sup>16</sup> filtering all but the 1–10 kHz bandwidth in which the chopper wheel frequency falls. Demodulation with a lock-in amplifier<sup>17</sup> at the blue chopper frequency yields a Doppler-free hyperfine spectrum as in the vapor cell.

We have several techniques in place for use in the process of signal optimization. First, before searching for a two-step signal after, say, opening the chamber to replenish the indium supply, we always optimize the first-step, 410 nm transition. Because of the small optical depths of the atomic beam, we cannot see first-step absorption ‘by eye’; instead, we use a chopper wheel to modulate the atomic beam itself, then lock-in demodulate transmitted blue light to find only that part of the blue signal that changes in the presence of atoms. We can then adjust the alignment of the blue beam through the ABU to optimize the size of the signal (a true Voigt profile in this case because the Doppler width [ $\sim 100$  MHz] and natural linewidth [ $\sim 25$  MHz] are roughly comparable in magnitude). This introduces the minor inconvenience of having a static chopper wheel in the atomic beam path as we optimize our two step signal, but it is easily solved by repeatedly turning the wheel on and off and monitoring how that signal changes in doing so. With enough repetitions (typically 10 or 20) we can develop a sense for its maximum amplitude and turn off the wheel in a position that yields such optimal absorption. The wheel’s openings are large enough to allow the entire collimated beam to pass unhindered, so we experience no diminution in signal size due to the wheel’s presence (opening the vacuum chamber has, indeed, revealed that our optimization process left the wheel in a position to allow the full beam through).

A second tool in signal optimization is a pair of irises placed near both windows into the interaction region. After optimizing the first-step transition, we center these irises in the blue beam path and fasten them to the table. We can than visually align the red laser beam through the irises – if done sufficiently precisely (even just by eye, with careful attention to maximizing intensity through the iris), this alignment procedure yields a sufficiently large signal to use in the data-taking process. We realign both beams to the irises each day we collect data – beam paths can drift slightly overnight, and realignment also helps correct for possible systematics that might arise due to imperfect beam overlap. The observed signals, though still fairly noisy, are well-enough resolved to find peak locations to within 1-2 MHz.

## 4.4 Data Collection Process

When we take data we are interested in two broad elements of the experiment: the collection of optical spectra, and the proper control and measurement of electric fields in the ABU. Both processes are automated through a LabView program, which

---

<sup>16</sup>New Focus model 2051.

<sup>17</sup>Stanford Research SR810. The signal is still often inherently noisy, so we require a large time constant – 30 ms for the weaker  $7P_{1/2}$  spectra – and accordingly slow red laser scan period ( $\sim 30$ s) to reduce it to a tolerable level. Spending time optimizing the red laser’s scanning behavior is also critical, since some frequency regions of a given mode are noisier than others.

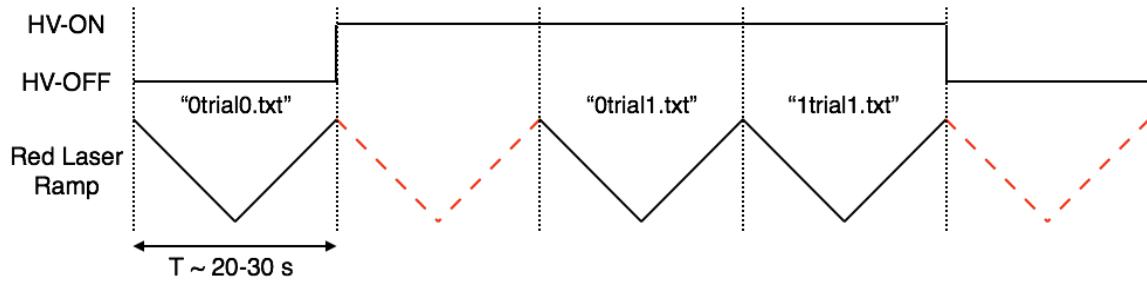


**Figure 4.10:** Outline of the data acquisition procedure for  $7P_{1/2}$  scalar polarizability data. Note that we wait a full scan period to begin collecting data after turning the high voltage on or off to allow the system time to equilibrate (red, dashed laser ramps). Building in an alternation between ‘OFF→ON’ and ‘ON→OFF’ data not only allows for a useful systematic error check but also allows us to skip half as many scans.

interacts with the apparatus via a National Instruments DAQ board and various other USB and serial interfaces.

The collection procedure, schematically outlined in figure 4.10 for  $7P_{1/2}$  scalar polarizability measurements, can be broken into fundamental units that we call ‘scans.’ Each corresponds to one period of the triangle wave driving the red laser PZT – during the analysis process, we will separate these into ‘upscans’ and ‘downscans.’ To measure the Stark shift, we alternately collect scans with the high voltage (HV) system on and off. Further, as a systematic check on long-term laser drifts, we alternate the order in which the voltages are collected, taking a set of two scans in ‘OFF→ON’ succession followed by a set of two scans in ‘ON→OFF’ succession. As shown in figure 4.10, one of every three scans goes uncollected to allow time for the HV system to equilibrate.

In preparation for a collected scan, the LabView program sets the high voltage value, waits 10 seconds for equilibration, and reads the true voltage (which typically differs from the set voltage by  $\sim 1\%$ ) from the Keithley voltmeter. With this value it calculates the necessary 410 nm lockpoint correction (equation 4.4; see section 4.3.2) and adjusts the two AOM frequencies accordingly. Finally, it records the temperature of the indium crucible and collects one scan’s worth of data from (1) the red laser ramp, (2) the red Fabry-Pérot, (3) the vapor cell reference spectrum, and (4) the atomic beam signal. Each of these will be employed in the analysis procedure detailed in chapter 5.

# Chapter 5

## Data Analysis and Preliminary Results

In this chapter we describe the work required to take raw atomic spectra collected per the methods of chapter 4 and come up with values for the polarizabilities of interest in this thesis. The first step is to locate the atomic resonances from these signals in a well-calibrated frequency space. This process is carried out using a suite of MATLAB code and is described in section 5.1. From these locations, coupled with a thorough understanding of the theory detailed in chapters 2 and 3, we can determine polarizabilities. Using such methods we converge upon results for the quantities of interest and conduct error analyses – both statistical and systematic – to arrive at results and associated uncertainties. While we have not yet determined final values for any of the polarizabilities discussed in this thesis, section 5.2 presents preliminary results and error analyses for the  $7P_{1/2}$  scalar polarizability, and section 5.3 does so for the scalar polarizability of the  $7P_{3/2}$  state.

### 5.1 Data Fitting Procedure

In this section we describe the portion of the analysis procedure tasked with taking raw absorption spectra and extracting information about the atomic resonances contained therein. Section 5.1.1 describes the process of analyzing Fabry-Pérot and vapor cell data in order to create a linearized and calibrated frequency axis. Sections 5.1.2 and 5.1.3, meanwhile, describe the process of locating atomic resonances and Stark shifts in vapor cell and atomic beam data, respectively.

#### 5.1.1 Frequency Mapping, Linearization, and Calibration

The establishment of a frequency axis requires a reference in the acquired signal with known frequency. Luckily, we have two such references: the  $\pm 1000$  MHz EOM sidebands in our vapor cell spectra; and the Fabry-Pérot spectra, which have peaks equally spaced by a free spectral range (FSR) of 363 MHz for our cavity. Both can

be used to establish the desired linear frequency axis. For more on the procedure, which we only briefly outline below, see [30].

In short, we use the Fabry-Pérot transmission as a ruler, enforcing that each peak be separated by 363 MHz as a means of establishing a frequency scale. Our raw scans, however, are not entirely linear: hysteretic effects mean that the red laser's diffraction grating does not move precisely with the PZT, which itself does not expand and contract perfectly linearly with voltage. In order to compensate for such nonlinearities, we incorporate a linearization polynomial (typically fifth order) into our fits to the Fabry-Pérot transmission. The best-fit polynomial then acts as a mapping function from the raw  $x$ -axis (composed of integers enumerating the collected data points<sup>1</sup>) to a linearized frequency axis; applying it to the horizontal axis of vapor cell and atomic beam data thus yields a signal with a consistent frequency scale.

Properly *calibrating* this axis remains to be done – 363 MHz is only approximately the cavity FSR, so while the axis is linear after application of the polynomial, extracted splittings will be in error by a factor  $\text{FSR}_{\text{actual}}/363$ . We can correct for such a calibration error using the  $\pm 1000$  MHz EOM sideband splittings in our vapor cell data. Multiplying the Stark shifts extracted from our atomic beam fits by a factor  $C_{\text{EOM}} = 1000/\Delta\nu_{\text{obs}}$ , where  $\Delta\nu_{\text{obs}}$  is the average observed sideband splitting, gives well-calibrated final results. In our data we find  $\Delta\nu_{\text{obs}} \approx 996$  MHz, corresponding to a calibration factor  $C_{\text{EOM}} \approx 1.004$  (and a true FSR closer to 364.5 MHz).

### 5.1.2 Vapor Cell Reference Spectra

After linearizing the frequency axis for a scan, but before extracting a Stark shift from the atomic beam, we need to establish a robust frequency reference. The vapor cell signal provides this<sup>2</sup>; even if the PZT-driven laser frequency drifts somewhat between field-off and field-on scans, the location of the field-free hyperfine resonances in the vapor cell will remain constant.

As discussed in section 2.2.3, the two-step spectroscopic method used in the vapor cell leads to a Doppler-free signal consisting of Voigt profiles at the excited-state hyperfine resonances (along with  $\pm 1000$  MHz sidebands due to EOM phase modulation of the red laser). For the indium  $7P_{1/2}$  state this signal contains six peaks: two ‘main’ peaks corresponding to the  $F'' = 4$  and  $F'' = 5$  hyperfine levels, and four first-order sidebands spaced by 1000 MHz from these hyperfine resonances.

The most obvious way to proceed with extracting peak locations would be to fit to a sum of six Voigt profiles – as good an analytic representation of the observed spectrum as we can find.<sup>3</sup> At the same time, because of the complicated form of the

<sup>1</sup>In practice, we first normalize this raw  $x$ -axis to range from -1 to 1 (see [30] for details), but that does little to change the principle of the procedure.

<sup>2</sup>At least it provides it for indium  $7P_{1/2}$  measurements. We cannot collect vapor cell spectra for high-field  $7P_{3/2}$  measurements (these are necessary to observe a resolved sublevel – see section 3.3) because the red laser scan is centered a full 8 GHz away from the field-free resonances in the cell – well beyond the size of a typical scan range.

<sup>3</sup>Admittedly, the true lineshape behaves more like that presented for a three-level system in

Voigt profile, fits of this sort are inconveniently time-intensive to run.<sup>4</sup> Coupled with the fact that in our particular spectra the Lorentzian component dominates, this suggests that a more effective means of fitting would be to simply use Lorentzian peaks. Extensive work in the Majumder group in recent years has shown that the results of Lorentzian fitting tend to fall in statistical agreement with their Voigt counterparts for these two-step, Lorentzian-dominated spectra. Accordingly, we choose to fit our  $7P_{1/2}$  vapor cell spectrum to a sum of six Lorentzians – this improves the speed of fitting by an order of magnitude and makes no measurable difference in results.

To prepare a vapor cell scan for fitting of this sort we first linearize the frequency axis as described in section 5.1.1 and normalize the amplitude of the largest peak to one for consistency; we then apply a non-linear least squares fit to the agreed-upon sum of six Lorentzians. A representative  $7P_{1/2}$  signal, with corresponding fit, is given in figure 5.1. As can be clearly seen, these signals have high enough signal-to-noise ratios to allow for very precise peak determination. In a scan such as that shown, the fitting program is capable of determining the location of any one of the six peaks to around or under 0.5 MHz.

One advantage of fitting the vapor cell in this way is that we get a measurement of the  $7P_{1/2}$  hyperfine splitting for free. This value, 458.56(03) MHz, has a statistical uncertainty below the 0.01% level and agrees with a dedicated Majumder lab measurement of the same splitting over the summer preceding this thesis (see appendix E and [17]).

### 5.1.3 Atomic Beam Fitting and Stark Shift Determination

We now turn to our atomic beam signals, from which we can actually extract the Stark shifts of interest in this thesis. Aside from a reduced signal-to-noise ratio resulting from a lower density of atoms in the beam, for the  $7P_{1/2}$  state these differ little from our vapor cell spectra. While there are no sidebands (EOM demodulation decreases the size of our already-small peaks, and we don't need sidebands in the ABU since we have already used the vapor cell for frequency calibration), we observe two hyperfine peaks, corresponding to the  $F = 4$  and  $F = 5$  levels.

Unlike in the vapor cell where our interest is in extracting peak locations and splittings within a given spectrum, in the atomic beam our primary concern is rather in finding a *shift* between successive scans. This opens up the possibility of two analysis methods. The first is similar to that employed in the vapor cell, where we fit to

---

section 3.2.1. Nonetheless, we do not observe the Autler-Townes splitting in the vapor cell, and so a Voigt profile is an awfully good approximation – perhaps even better, since equation 3.10 makes no effort to capture the effects of, say, spontaneous emission.

<sup>4</sup>The analytic form of the Voigt profile requires integrating a Gaussian and Lorentzian together, and we need to resort to robust approximation methods to effectively fit it. While these are well-known, they are time-intensive to run, often taking a minute for a fit that would, with Lorentzians, take under a second. Further, at least for our spectra, these fits tend to yield Gaussian and Lorentzian widths that are highly dependent on initial guesses for the fit parameters, so they do not do a much better job of capturing the lineshape anyway.

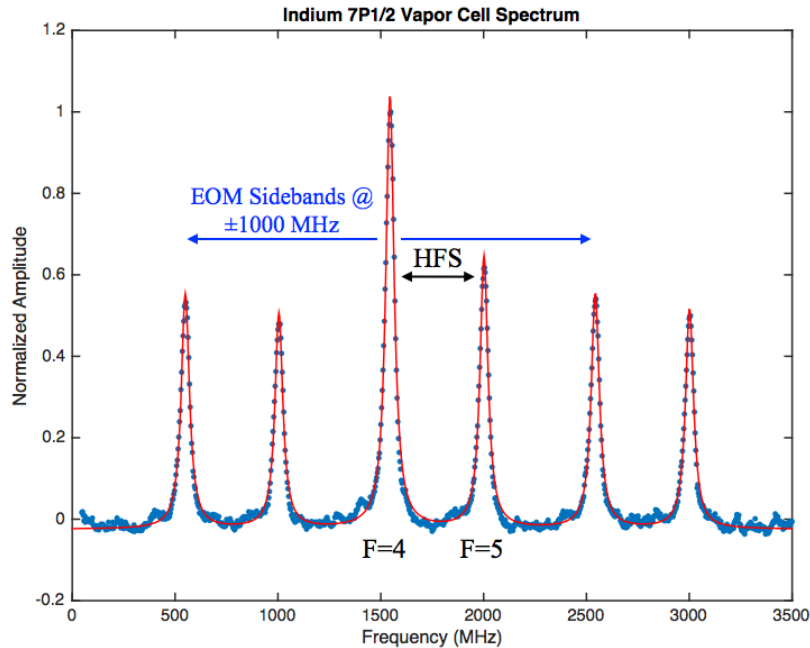


**Figure 5.1:** Observed indium  $7P_{1/2}$  vapor cell spectrum, with fit to a sum of six Lorentzian peaks (red, solid line). The center two peaks are the  $F'' = 4, 5$  hyperfine levels, and the four peripheral peaks are  $\pm 1000$  MHz sidebands resulting from EOM phase modulation of the 690 nm laser. These provide a reference for use in calibrating the frequency axis (section 5.1.1).

an analytic function and determine the Stark shift based on the best-fit peak locations. The second is radically different: rather than assuming an analytic lineshape, we instead simply translate scans along the frequency axis until they ‘overlap.’

### The Lorentzian Fit Method

The first method is similar to that employed in the vapor cell. The two peaks in our collected  $7P_{1/2}$  atomic beam spectra are roughly Lorentzian; so, employing the same reasoning we did for the former case, we simply choose to fit the (linearized and normalized) signal to a sum of two Lorentzian peaks. Such a fit for a representative atomic beam signal is shown in figure 5.2. Uncertainties in the fit can vary widely due to changes in the signal-to-noise ratio for a given scan, but typically our Lorentzian fit can extract peak locations to  $1 - 2$  MHz uncertainty.

To determine the Stark shift, we then take relevant peak differences. In order to account for red laser drifts from scan to scan, we reference each of the field-off and field-on peaks to a particular vapor cell resonance – this serves as a stable frequency reference since there is no field applied in the cell. We can then extract the Stark shift for peak  $n$  in the atomic beam using

$$\Delta f_n = k_S \mathcal{E}^2 = (f_{n,\text{on}} - f_{0,\text{on}}) - (f_{n,\text{off}} - f_{0,\text{off}}) , \quad (5.1)$$

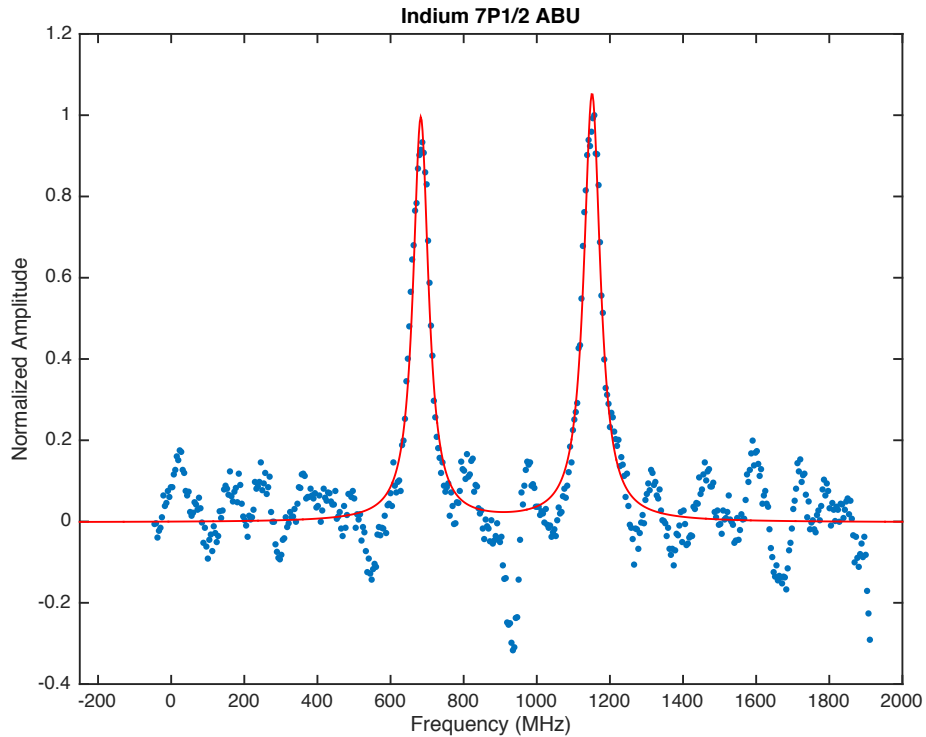


**Figure 5.2:** Indium  $7P_{1/2}$  atomic beam signal, with fit to a sum of two Lorentzians (solid red line). The two peaks correspond (from left to right) to the  $F = 4$  and  $F = 5$  hyperfine levels. Despite the decreased signal-to-noise ratio when compared with vapor cell data, this particular fit was capable of extracting peak locations to under one MHz uncertainty.

where ‘on’ and ‘off’ correspond to field-on and field-off scans, and  $f_0$  is the location of the vapor cell reference peak in the relevant scan.

This approach has several advantages. For one, we can calculate the shift for each hyperfine peak separately; checking how well they agree provides a good test of systematic errors. We can also choose which vapor cell peak to reference, allowing for a further test of potential systematics. Finally, using the Lorentzian fit method we can extract a value for the  $7P_{1/2}(F = 4 - 5)$  hyperfine splitting from the atomic beam. We hope that this value agrees with the one measured in the vapor cell and, perhaps more importantly, with our dedicated measurements of this value from the summer preceding this thesis (appendix E and [17]). Confirming such agreement inspires confidence in our ability to properly fit the atomic beam signal.

### The Overlap Method

Our second approach to Stark shift determination in the  $7P_{1/2}$  state differs dramatically from the Lorentzian fit method. Its principle derives from the complicated dependence of the true lineshape on Rabi frequencies (equation 3.10) – if we don’t know the precise analytical lineshape, it asks, are we making unsustainable compromises by fitting to Lorentzians?

The solution proposed by the overlap method is to ignore the particular lineshape entirely. We know that it remains unchanged when we turn the field on (assuming a Stark-shift corrected 410 nm lock – see section 3.2.1), so we can extract the Stark shift by translating, say, the field-on signal along the frequency axis until it ‘overlaps’ with the field-off signal, minimizing the sum of squared differences between the two. The amount by which we have translated the field-on signal to reach the point of optimal overlap is the Stark shift.

In practice, we effect this fitting method by defining an interpolating function for each of the two scans under consideration (field-off and field-on, respectively), referencing the zero of each frequency axis to a vapor cell hyperfine peak in order to account for scan-to-scan red laser drifts.<sup>5</sup> Following [25, 30], if we call the field-free interpolating function  $\mathcal{A}(f)$ , then the field-on interpolating function looks something like  $\mathcal{A}(f - s)$ , where  $s = k_S \mathcal{E}^2$  is the Shift shift. Now we shift the field-on interpolation by an amount  $\delta$  and compute chi-squared ( $\chi^2$ ) values, so that

$$\begin{aligned}\chi^2(\delta) &= \sum_{\text{all } f} \{\mathcal{A}(f) - \mathcal{A}(f - (s - \delta))\}^2 \\ &\approx \sum_{\text{all } f} \{\mathcal{A}(f) - \mathcal{A}(f) + \mathcal{A}'(f)(s - \delta)\}^2 \\ &= (s - \delta)^2 \sum_{\text{all } f} \mathcal{A}'(f)^2 \propto (s - \delta)^2\end{aligned}\tag{5.2}$$

where in the second step we have expanded for small  $s - \delta$ , since we expect  $\delta$  to be very near the Stark shift when our functions are maximally overlapped. Near  $\delta = s$ , then,  $\chi^2(\delta)$  looks quadratic and is minimized at  $\delta = s$ . In practice, noisy data make it so that this minimum is not *zero*; nonetheless, it still holds true that, at least on average, minimizing  $\chi^2(\delta)$  will yield a value for  $\delta$  equal to the Stark shift.

We extract this value by iterating over values of  $\delta$  in our fitting program and each time calculating a chi-squared value using a set of equally spaced points along the interpolation functions. We save these  $\chi^2$  values as a function of  $\delta$  and then apply a quadratic fit to the region of this curve near the expected Stark shift. We then determine the vertex of the parabolic fit – this is our Stark shift. Figure 5.3 shows a plot of the two interpolating functions in their ‘maximally-overlapped’ configuration, and figure 5.4 shows a fit to the quadratic portion of the chi-squared curve for one scan.

While the advantage of this approach is that it assumes no specific form for the observed atomic beam lineshapes, the fact that we do not fit individual peaks means that we cannot extract a hyperfine splitting or compare the Stark shift of the two peaks individually as in the Lorentzian fit approach. We can, however, choose which vapor cell peak to reference, allowing something in the way of systematic error analysis.

---

<sup>5</sup>Note that here we *do not* normalize our spectra, unlike in the Lorentzian fit case. Normalizing will inevitably alter the relative sizes of the two signals we wish to compare, thereby somewhat distorting the comparison between raw signals that we really want to make.

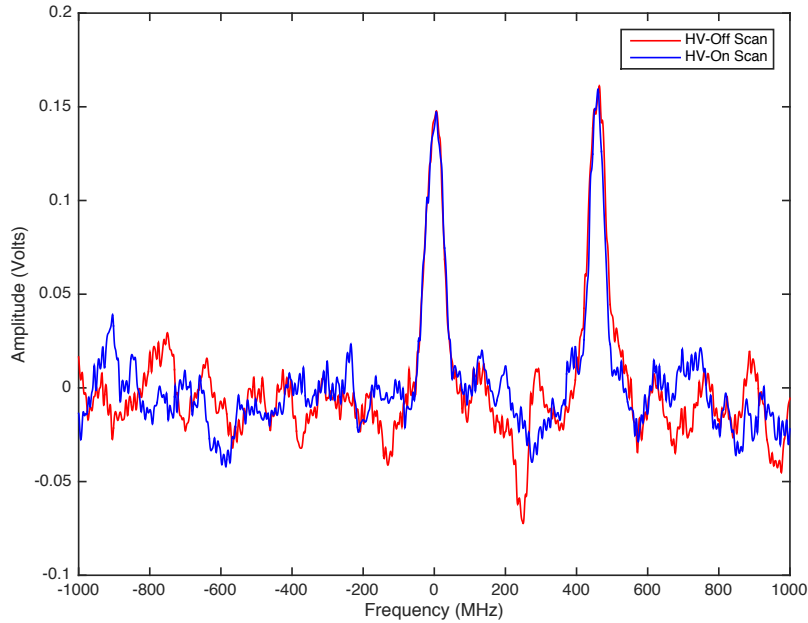


**Figure 5.3:** Field-off and field-on  $7P_{1/2}$  atomic beam signals in their ‘maximally overlapped’ configuration, determined by minimizing the sum of squared differences (chi-squared value) between two interpolating functions representing the signals. Note that, despite the noisiness of the baseline, the program appears to do a good job of overlapping the peaks, at least to the eye. While the baseline noise should average out over many scans, we do vary the size of the ‘window’ surrounding the two peaks as a check on systematics.

Most importantly, this gives us an alternative to the Lorentzian approach; examining the extent to which the two methods agree or disagree will factor in below as a useful check on systematics.

## 5.2 Preliminary $7P_{1/2}$ Results and Error Analysis

Having analyzed collected spectra to extract calibrated Stark shift values, our task is now to combine these results and determine a value for the scalar polarizability, along with associated uncertainties. We can divide this process into two parts: the determination of center values and statistical errors, and the consideration of potential systematic errors.

### 5.2.1 Determination of Center Values and Statistical Errors

We can take two approaches to finding center values for our Stark shift measurements. The first is to plot a histogram of shift values and – because we assume a well-behaved Normal distribution of results – fit this histogram to a Gaussian. From here we can extract a mean shift and an associated standard deviation; the standard error in our mean result is then simply  $\sigma/\sqrt{N}$ , where  $N$  is the number of values contained in the

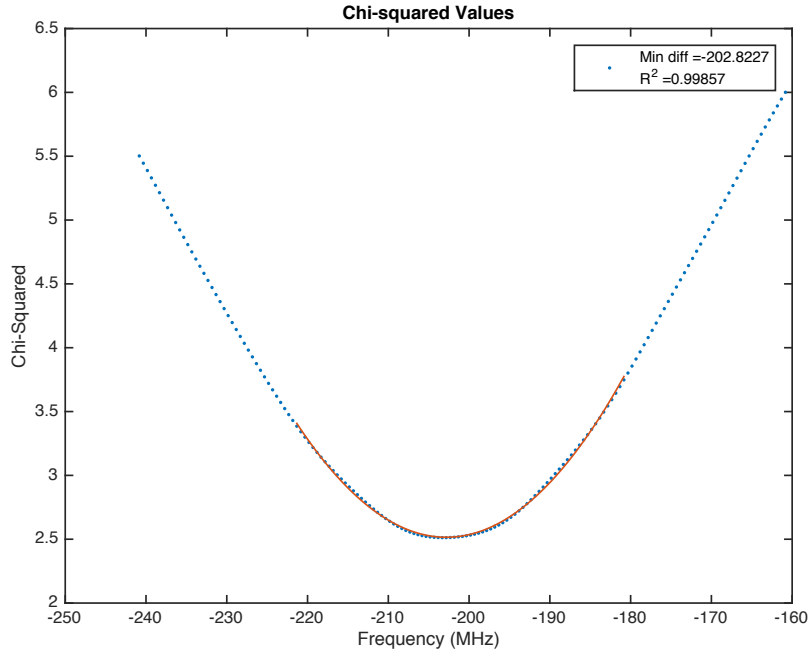


**Figure 5.4:** Curve of chi-squared values against shift frequency for the overlap method with  $\mathcal{E} \approx 3$  kV/cm. We fit the region near its minimum to a second-order polynomial (solid red curve), then determine its vertex – this is the Stark shift. We can typically find the location of this minimum to an uncertainty of anywhere from 1 to 5 MHz, depending on the noise level of the atomic beam scans in question.

histogram.

The second approach involves weighting individual data points based on the quality (i.e. standard deviation) of their respective fits, and computing a weighted mean and error according to

$$\overline{\Delta\nu}_{\text{weighted}} = \frac{\sum_i \Delta\nu_i / \sigma_i^2}{\sum_i 1/\sigma_i^2} \quad (5.3)$$

$$\sigma_{\text{weighted}}^2 = \frac{1}{\sum_i 1/\sigma_i^2} \quad (5.4)$$

In this latter process we also correct the errors to bring the reduced chi-squared value,  $\text{Red}\chi^2 = \chi^2/(N - 1)$ , equal to 1,<sup>6</sup> effectively adjusting the errors to account for underestimates of the observed scatter about the mean. For purposes of comparing datasets with different experimental parameters, we first typically apply one of these methods to each set of  $\sim 24$  scans to calculate center values and errors for each. We then analyze the center values and errors of these sets together, taking a (weighted) ‘mean of means’ to arrive at a final value.

In order to extract a number for the Stark shift constant we can apply either of these methods to find the mean shift for a given field and divide through by the

---

<sup>6</sup>This is effected by computing chi-squared – i.e. the sum of squared differences from the mean – and multiplying the computed errors by  $\sqrt{\text{Red}\chi^2} = \sqrt{\chi^2/(N - 1)}$ .

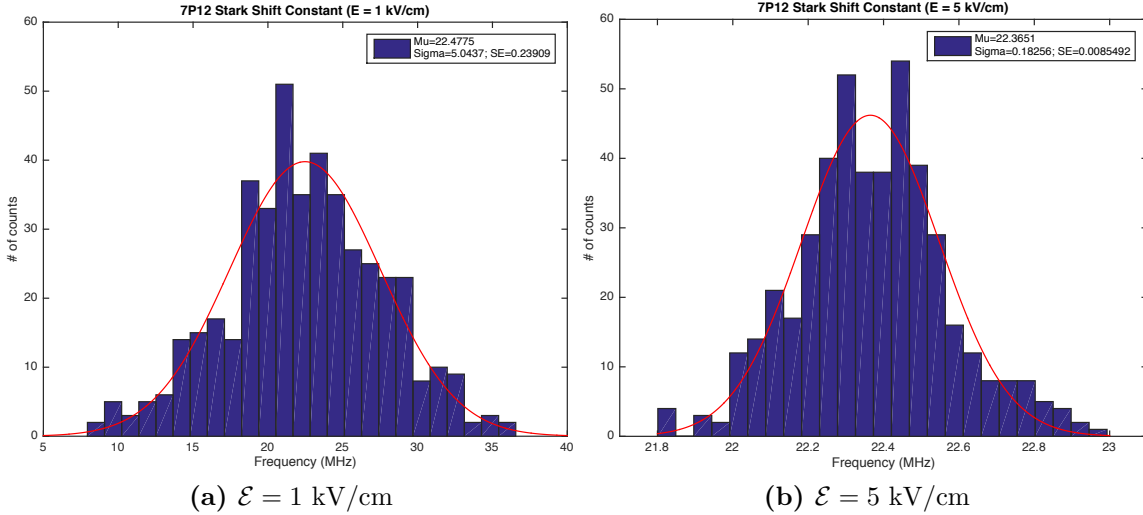


**Figure 5.5:** Histograms of  $\sim 500 k_S$  values, at representative electric fields of  $E = 1 \text{ kV/cm}$  and  $E = 5 \text{ kV/cm}$ , extracted from the week's worth of data considered in this thesis. Each is fit to a Gaussian (solid red line) in order to extract a mean and standard error ( $\sigma/\sqrt{N}$ ). While the centers of the two histograms agree, their widths differ greatly (notice the relative scales of the two frequency axes). The greater precision of the  $E = 5 \text{ kV/cm}$  data arises because we divide measured splittings, in that case, by  $E^2 = 25 \text{ (kV/cm)}^2$  to arrive at  $k_S$ .

magnitude of the field squared. This yields  $k_S$  values for each in a series of electric fields separately. Figure 5.5 shows histograms of all such values for two representative electric fields of  $E = 1 \text{ kV/cm}$  and  $E = 5 \text{ kV/cm}$ . The spread of the  $E = 5 \text{ kV/cm}$  data is smaller than that for  $1 \text{ kV/cm}$  because we divide through by the field squared to extract the Stark shift constant.

Alternatively, we can account for all fields at the same time. To do so, we plot our observed shifts as a function of electric field squared and fit a line to the data; its slope will be the the Stark shift constant. Such a fit is shown in figure 5.6.

### 5.2.2 Consideration of Systematic Errors

Our next task is to consider errors resulting from changes in experimental and analytic parameters. These considerations do not factor in to our statistical uncertainties, but they do reflect irregularities in our data and analysis that make us less confident in the precision of the result. We can organize these errors into several categories.

#### Binary Experimental Parameters

When we collect data, we divide our data in two ways: (1) by the direction of the laser scan ('upscan' vs. 'downscan') and (2) by the order in which we collect field-off and field-on scans ('off  $\rightarrow$  on' vs. 'on  $\rightarrow$  off'). We can analyze data in these configurations separately and compare results. Discrepancies in results between scan

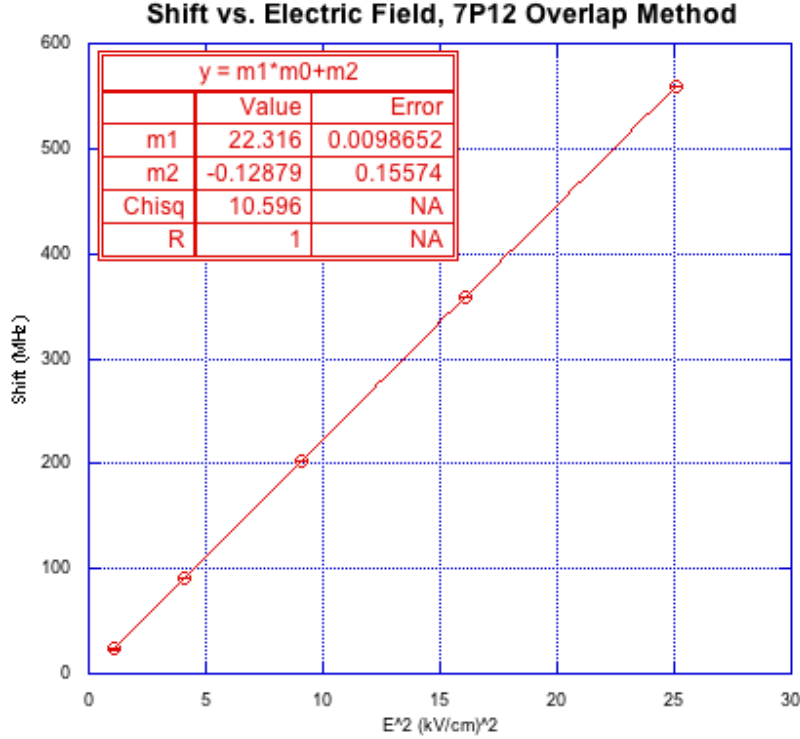


**Figure 5.6:** Plot of measured Stark shifts against electric field squared for indium  $7P_{1/2}$  data,  $\mathcal{E} = 1\text{-}5 \text{ kV/cm}$ . The linear fit yields a Stark shift of  $22.316(16)$  MHz after applying a chi-squared error correction, and the y-intercept is consistent with zero, as expected.

directions can reflect some error in our ability to properly linearize the frequency axis, or perhaps some scan dependent peak asymmetry (such as an overlong lock-in time constant), and so adding in a systematic corresponding with the scan direction can help account for such problems. Similarly, comparing results for field ‘off → on’ and ‘on → off’ configurations addresses potential concerns like long-term voltage drifts in the apparatus. In both cases, if we find a statistically resolved discrepancy we append a systematic error to our result according to

$$\delta\nu_{\text{binary}} = \frac{1}{2} |k_{S1} - k_{S2}| ,$$

where  $k_{S1}$  and  $k_{S2}$  are Stark shift constants corresponding to the two binary parameters in question. A plot of these binaries, for overlap method results, is shown in figure 5.7.

### Continuous Experimental Parameters

During the data collection process we choose to vary laser polarizations and laser powers (over roughly a factor of four). For the  $7P_{1/2}$  state these parameters should

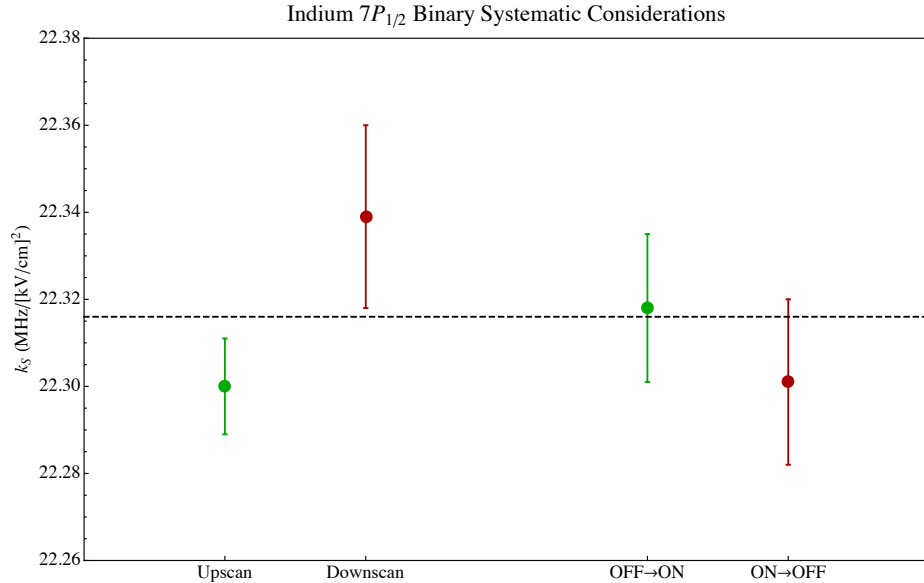


**Figure 5.7:** Plot of Stark shift constants for two binary parameters, analyzed using the overlap method. Note that the ‘off → on’ and ‘on → off’ values are in good agreement, while the ‘upscan’ and ‘downscan’ values disagree, leading us to append a systematic error to our final value.

not affect our results,<sup>7</sup> and so correlations between extracted Stark shift and either power or polarization must be taken into account as reflecting systematic errors we have not properly eliminated in the experiment.

A further systematic to consider in the context of Stark shift measurements is the correlation of  $k_S$  with applied electric field. Because we have already divided through by the field-squared in determining  $k_S$ , this relationship should be constant; if we observe a trend in the data it might suggest a non-quadratic term in the shift.<sup>8</sup> We must account for this as reflective of an inability to analytically determine the polarizability via the second-order perturbative approach demonstrated in section 3.1. A plot of  $k_S$  against  $\mathcal{E}$  is given in figure 5.8 for overlap method results. We see only what appear to be random fluctuations about the overall mean. A plot for Lorentzian method results similarly shows no trend.

---

<sup>7</sup>Changing laser powers will, as we have seen, change the lineshape – see section 3.2.1 – but the fact that these lineshapes nonetheless remain symmetric should mean that this has no effect on our ability to find their centers. At the very least, such discrepancies will subtract out when we calculate shifts, since field-on and field-off peaks have the same lineshape. Laser polarizations and powers *do* impact  $7P_{3/2}$  lineshapes in a meaningful way, and so we must take them into account during analysis for that state.

<sup>8</sup>Of particular concern are linear terms, indicating that we have begun to move into the high-field linear Stark shift regime.

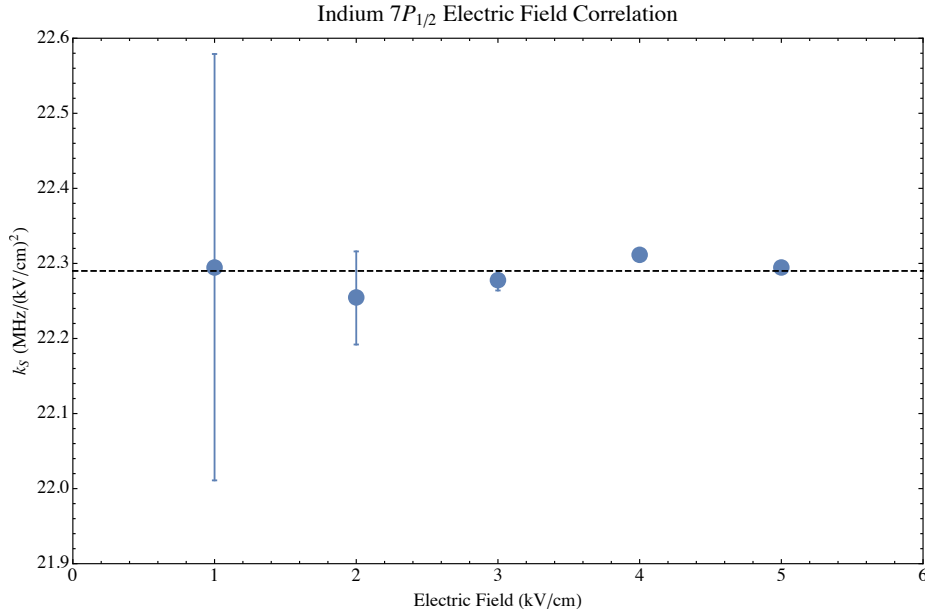


**Figure 5.8:** Plot of Stark shift constants against electric field for overlap method data. We observe no trend, suggesting that we need not worry about unwanted correlations between  $k_S$  and the field.

### Analysis-Level Systematics

During the analysis process we encounter further systematics for inclusion in the final error budget. Several address the degree to which we are able to properly create a calibrated, linear frequency axis. By comparing EOM sideband splittings across the range of the vapor cell scan we can quantify residual non-linearities that remain after the Fabry-Pérot fitting process. For our data the four sideband splittings agree to within 0.3 MHz, but we include a small systematic to account for this difference nonetheless. A similar systematic captures calibration uncertainty by considering run-to-run variations in the calibration factor  $\mathcal{C}_{\text{EOM}}$ .

Finally, because we have two means of extracting the Stark shift – the Lorentzian method and the overlap method – we can compare their results and apply a systematic related to any discrepancies. It turns out that these values differ by roughly 0.05 MHz, so we add a systematic of half this magnitude to our error budget (the factor of one-half comes in because we expect the true Stark shift to lie somewhere between these two values).

### 5.2.3 Preliminary $7P_{1/2}$ Scalar Polarizability Results

Table 5.1 shows a preliminary value and error budget for the indium  $7P_{1/2}$  Stark shift constant,  $k_S$ . As of now the statistical error is larger than many of our systematics; as we continue to collect data we hope to improve our statistics and, in the process, shed light on yet more possible systematic effects.

<b>Stark Shift (MHz/[kV/cm]<sup>2</sup>)</b>	22.344
<b>Statistical Error</b>	0.020
<b>Systematic Error Sources</b>	
Laser scan direction	0.020
Scan linearization	0.003
Frequency calibration	0.005
Fitting method	0.028
Electric field calibration	0.001
<b>Combined Error Total (MHz/[kV/cm]<sup>2</sup>)</b>	0.040

**Table 5.1:** Preliminary result, with statistical and systematic error budget, for the indium  $7P_{1/2}$  Stark shift constant,  $k_S$ .

We can convert this value to a scalar polarizability using equation 3.12 along with lower-state polarizability measurements and calculations from [11, 19]. Doing so, we obtain  $\alpha_0 = 1.8064(32) \times 10^5 a_0^3$ . This value is currently an order of magnitude more precise than the theory value of  $1.8632(460) \times 10^5 a_0^3$  given in [22], which – as figure 5.9 makes clear – it slightly undershoots. It is interesting to note that the  $\sim 3\%$  disagreement between our value and the theory is roughly matched by the  $3\%$  disagreement, in the same direction, between a recent measurement of the  $6P_{1/2}$  scalar polarizability and a similar theory calculation (see [11, 13], as well as appendix A and figure 1.1). This suggests a systematic tendency of this particular model to overestimate  $P$  state scalar polarizabilities in three-valence systems like indium.

Referring to the discussion in section 3.2.1, we can also determine a value for the reduced dipole matrix element between the  $7P_{1/2}$  and nearby  $6D_{3/2}$  state using this scalar polarizability measurement. Inserting our  $\alpha_0(7P_{1/2})$  into equation 3.14, we find  $\langle 6D_{3/2} || d || 7P_{1/2} \rangle = 21.16(4)$  atomic units. Given the difficultly of direct experimental measurements of matrix elements, it is remarkable to be able to attain such a value, at the 0.2% level, from a Stark shift measurement.

### 5.3 Preliminary $7P_{3/2}$ Scalar Polarizability Results

As discussed in section 3.3.1, we can extract the scalar polarizability of the  $7P_{3/2}$  state of indium by measuring shifts of the fully resolved  $|4, 4\rangle$  hyperfine sublevel at high fields near 15 kV/cm. Accordingly, we collect data with the apparatus described in chapter 4 but with the 685 nm, second step laser tuned roughly 8 GHz below the field-free  $6S_{1/2} \rightarrow 7P_{3/2}$  resonance so as to observe the Stark-shifted spectrum. Figure 5.10 shows an observed atomic beam signal under such a configuration; we clearly see three peaks – one corresponding to the  $|4, 4\rangle$  sublevel, one to the  $|4, 3\dots 0\rangle$  and  $|5, 5-4\rangle$  sublevels (we call this the ‘composite’ peak), and a third, wider profile for the

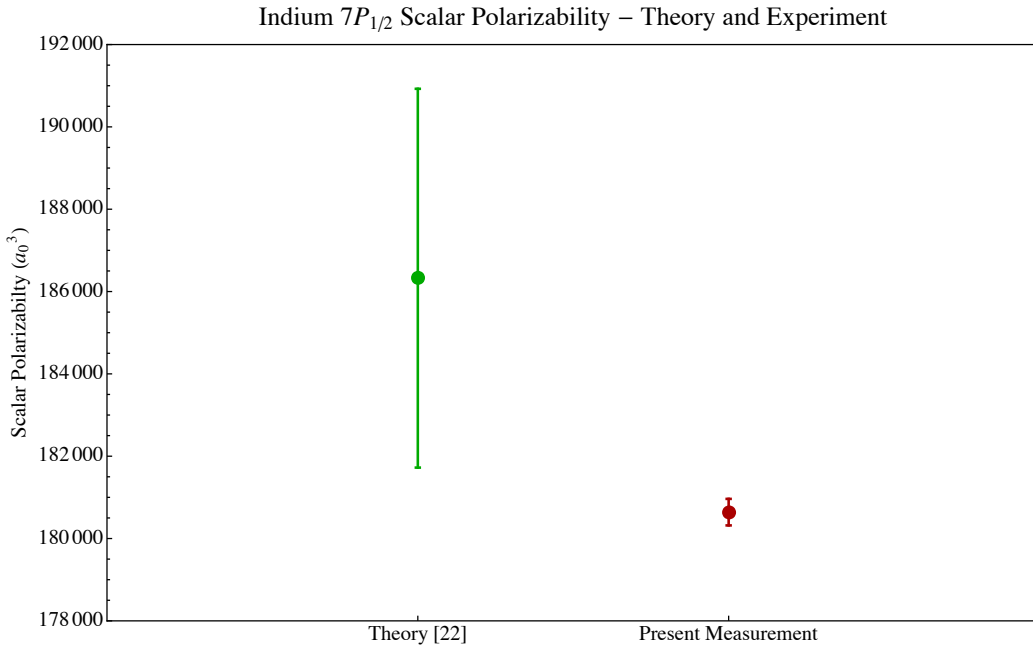


**Figure 5.9:** Comparison of theoretically calculated and experimentally measured values for  $\alpha_0(7P_{1/2})$ . The presently measured value undershoots the theory calculation by roughly 3% and improves upon the precision of the theory value by an order of magnitude.

remaining  $F = 5$  and  $F = 6$  sublevels. This matches our qualitative expectation from the simulation shown in figure 3.4. By alternately collecting such signals at various voltages (we choose 14, 15, and 16 kV – see figure 5.11) and measuring the shift of the  $|4, 4\rangle$  peak, we can extract a scalar polarizability per equation 3.20. Though our interest is in the  $|4, 4\rangle$  level alone, we choose to fit to both lower peaks in figure 5.10 because of their reasonably close proximity, throwing out the ‘messy’ upper peak for cleanliness.<sup>9</sup> From such a fit (to a sum of two Lorentzians as shown in figure 5.12) we can extract the location of the resolved hyperfine peak and compare with its location at other voltages.

There is a notable problem with this approach. Because the red laser is far detuned from the field-free resonances, we have no vapor cell signal with which to work. Though the polarizabilities themselves are extracted from the atomic beam, we have previously used the vapor cell signal as a stable frequency reference for calibration and Stark shift determination.

We address one issue by using the Fabry-Pérot cavity as a frequency reference (by, say, setting zero frequency to the location of the first peak). While not inherently as stable as an atomic resonance, the cavity is thermally isolated in an insulated box. Previous work has shown that such cavities exhibit short-term thermal fluctuations of order a few MHz, but no long-term drift [30]. Accordingly, we might expect referencing to the cavity to introduce more noise into our data but not, in the long

<sup>9</sup>See appendix D for more on the MATLAB code used to do this.

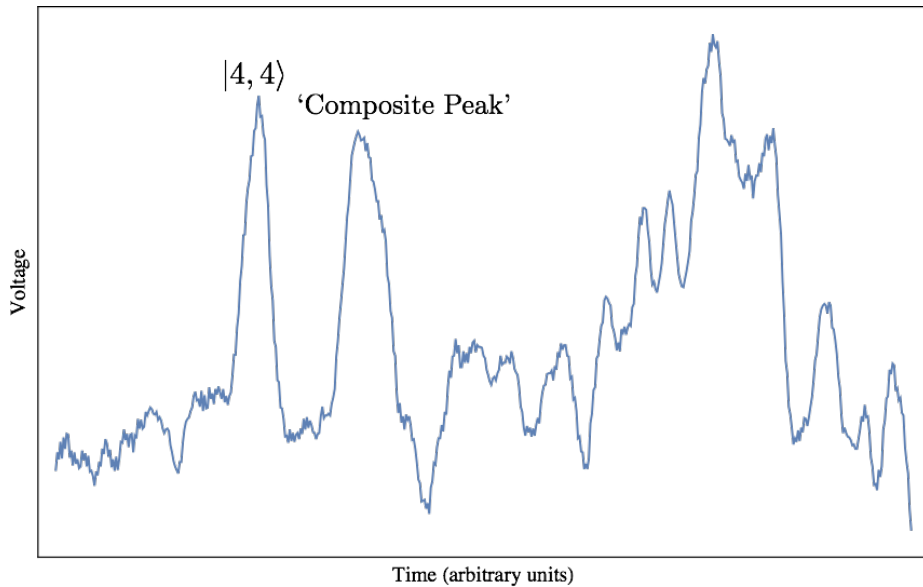


**Figure 5.10:** Indium  $7P_{3/2}$  atomic beam signal at  $\mathcal{E} = 15 \text{ kV/cm}$ . The leftmost peak is the  $|4, 4\rangle$  hyperfine sublevel, the middle peak is the ‘composite’ peak containing several  $F = 4$  and  $F = 5$  hyperfine sublevels, and the rightmost profile is a (somewhat noisy) collection of many  $F = 5$  and  $F = 6$  levels.

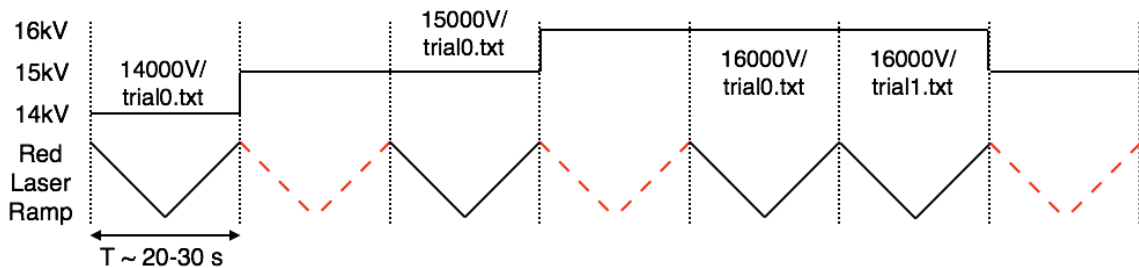


**Figure 5.11:** Schematic of the data acquisition procedure for indium  $7P_{3/2}$  scalar polarizability data. Red, dashed scans are those for which we do not collect data and instead allow the field to equilibrate. Note that this procedure alternates the order in which we apply voltages (i.e.  $14 \rightarrow 15 \rightarrow 16 \text{ kV}$ , followed by  $16 \rightarrow 15 \rightarrow 14 \text{ kV}$ ), allowing for a useful systematic error check.

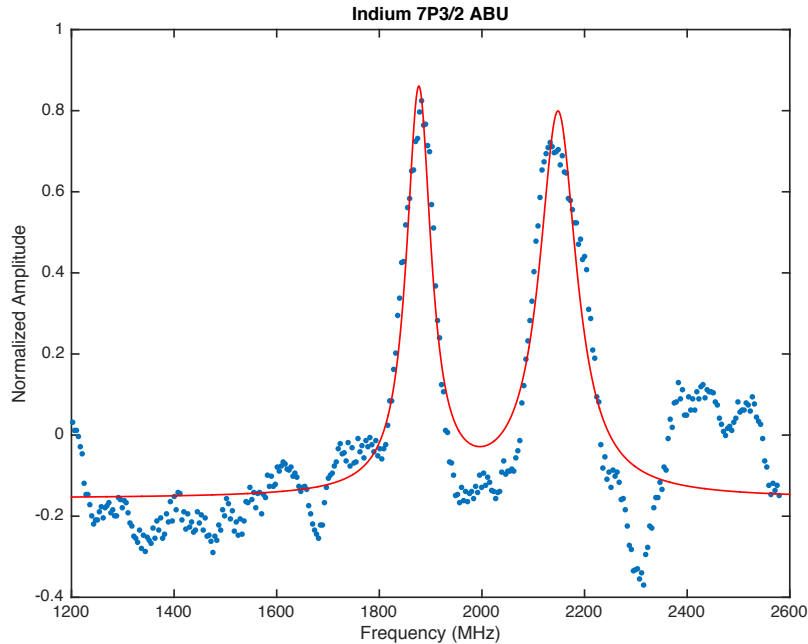


**Figure 5.12:** Fit to the  $|4, 4\rangle$  and ‘composite’ peaks of the  $7P_{3/2}$  atomic beam signal at  $\mathcal{E} = 15$  kV/cm. The fitted function (solid red line) is a sum of two Lorentzians. This particular signal is the same shown in figure 5.10, with the higher-frequency resonance profile excluded from the fit.

term, to introduce any significant systematic errors.

The problem of frequency calibration can be addressed by interspersing our high-field atomic beam data collection with field-free data collection in the vapor cell. From the sidebands in these vapor cell spectra we can extract a calibration factor for application to high-field ABU data.<sup>10</sup>

We have collected a small quantity of data ( $\sim 30$  scans) at each of 14, 15, and 16 kV/cm. In each case we determined peak shifts (of order 1100 MHz) to roughly 2 MHz statistical uncertainty. Diagonalizing the Stark mixing matrix in equation 3.7 and numerically solving for the scalar polarizability (equation 3.20), we come up with a value limited to  $\sim 1\%$  uncertainty by the imprecision of the tensor polarizability theory value [22]. The result is  $\alpha_0(7P_{3/2}) = 2.852(30) \times 10^5 a_0^3$  MHz. This agrees with the theory calculation in [22] but is a factor of 4 more precise. While we need to collect much more data and consider systematic errors, it is unlikely that the presently quoted error bar will much change, as uncertainty in the tensor polarizability will almost certainly be the dominant systematic.<sup>11</sup>

---

<sup>10</sup>Admittedly, the red laser is scanning over a different frequency range during field-free and high-field data collection, so one might wonder whether the calibration is truly the same. Tuning the laser by the 8 GHz necessary to switch regimes, however, should at most negligibly alter the Fabry-Pérot alignment, so it is reasonable to assume that the FSR remains constant to our level of precision.

<sup>11</sup>Experience tells us that most experimental systematic errors in our polarizability measurements are at or below the 0.1% level – an order of magnitude smaller than the former error.

Level	Experiment	Theory	Comparison
$6S_{1/2}$	1049.5(6.2) [19]	1056(27) [11]	+0.6% (CC)
		1042 [11]	-0.7% (CI+All)
$6P_{1/2}$	7590(37) [13]	7817(155) [11]	+3.0% (CC)
		7513 [11]	-1.0% (CI+All)
$7P_{1/2}$	$1.8064(32) \times 10^5$	$1.8632(460) \times 10^5$ [22]	+3.1% (CC)
$7P_{3/2}$	$2.852(30) \times 10^5$	$2.985(136) \times 10^5$ [22]	+4.7% (CC)

**Table 5.2:** Comparison of scalar polarizability measurements in the Majumder lab with relevant theory calculations. The ‘CC’ method treats indium as a hydrogenic system, with the outer  $p$  electron acting in effect as a single valence. The ‘CI + All’ method, meanwhile, attempts to consider interactions between all three  $ns^2p^1$  valence electrons (see [11] for more on these theoretical approaches). We note that the  $6S_{1/2}$  and  $7P_{3/2}$  values agree within their error bars, but we include comparisons to the *center* of the error bar in these cases for completeness. Note that the ‘CC’ approach systematically overestimates measured polarizabilities while the ‘CI+All’ method underestimates them. All values quoted are in atomic units ( $a_0^3$ ).

It is interesting to note that, as in the  $6P_{1/2}$  and  $7P_{1/2}$  cases, our measured scalar polarizability undershoots the center of the theory error bar by several percent (though they do agree within their error bars). This trend, for a series of recent Majumder group polarizability measurements in indium, is summarized in table 5.2.

# Chapter 6

## Ongoing and Future Work

Though we have made significant progress towards measurements of the indium  $7P$  polarizabilities over the course of this thesis, none of these measurements is complete. In this chapter we discuss the present state of affairs in each polarizability measurement, outlining the future work required to wrap up this line of experiments.

### 6.1 Continuing Scalar Polarizability Work

Our indium  $7P_{1/2}$  and  $7P_{3/2}$  scalar polarizability measurements have been left at different points in the data collection and analysis process; below, we outline the work left to do on these two projects.

#### 6.1.1 $7P_{1/2}$ Scalar Polarizability

Our measurement of the  $7P_{1/2}$  scalar polarizability is at the most advanced stage of those presently considered. We have roughly 2000 scans of data – corresponding to 1000 Stark shift determinations – and already have statistical errors at a tolerable ( $\sim 0.1\%$ ) level. Our concern at this point is the consideration of *systematic* errors, a process that requires that we collect more data. While the data we have already taken are sufficient for consideration of such binary parameters as scan direction and field collection order, they consist of only a small range of laser powers and polarizations, insufficient for robust consideration of these continuous variables. Furthermore, it is typical in two-step indium measurements to consider a systematic associated with the ‘first-step hyperfine transition’ (i.e. the particular ground and first-excited hyperfine levels we couple). All data considered in this thesis were taken along the  $5P_{1/2}(F=4) \rightarrow 6S_{1/2}(F'=5)$  first-step transition, so we hope to soon collect data along the analogous  $F=5 \rightarrow F'=4$  transition as well. This requires a retuning of the 410 nm laser by 20 GHz, a modest value easily attainable with a small ( $\sim 0.5^\circ\text{C}$ ) temperature adjustment to the diode.

Given the amount of data we were able to collect in one week’s time over the course of the present thesis, we expect that the remaining data collection for our

$7P_{1/2}$  measurement will take no more than a few weeks. These future data should cover a range of polarizations and laser power ratios (varying over perhaps a factor of 4), as well as several scan speeds (being careful not to go so fast as to effect peak asymmetry due to the length of the lock-in time constant). We also hope to duplicate this range of experimental parameters in several sets of data collected along the  $5P_{1/2}(F=5) \rightarrow 6S_{1/2}(F'=4)$  first-step transition. We expect that these measurements will not dramatically alter the value for  $\alpha_0$  quoted in this thesis, though they will likely decrease our statistical error bar and allow for the more complete consideration of important systematics.

### 6.1.2 $7P_{3/2}$ Scalar Polarizability

The completion of this measurement requires that we take significantly more data. Though the small quantity of data collected for this thesis gave a reasonable result with a statistical error well below the dominant, tensor polarizability-related theory uncertainty, we would like to collect many more scans under varying experimental conditions (electric fields, laser powers, polarizations, *etc.*) in order to more fully consider systematic effects. If we are able to make a measurement of the tensor polarizability (see section 6.2, below) we can hope to achieve a final error below the 1% level; otherwise, we hope only to decrease statistical and systematic uncertainties to a point where they do not contribute significantly on top of the theory error.

As part of this process we would like to further characterize the stability of the Fabry-Pérot cavity, and hence its suitability as a frequency reference for Stark shift measurements. Further, because we currently achieve EOM sideband calibration only in the field-free vapor cell environment, it is important that we develop a method, going forward, of determining the extent to which frequency axis calibration and linearization change near the  $\sim 8$  GHz Stark shifted resonances we probe in the measurement.<sup>1</sup>

## 6.2 $7P_{3/2}$ Tensor Polarizability Work

Our work towards the measurement of a tensor polarizability is at a much earlier stage in development than either scalar polarizability measurement. Present work is still devoted to theory and the search for a viable method of experimental measurement using the lineshape simulation tools developed in chapter 3. We can divide this work into two parts; one concerns improvements to the many-level theory used for lineshape simulation, and the other is devoted to the consideration of potential techniques for polarizability extraction.

---

<sup>1</sup>While Fabry-Pérot realignment with frequency should be minimal and therefore not affect our frequency calibration, it is very possible that the linearization properties of our laser depend on the particular properties of its (frequency-dependent) lasing mode. The FP fitting procedure should take care of linearization in any event, but it would be nice to have a means of determining residual ‘scan linearity’ systematics.

## Improvements to Theoretical Lineshape Treatment

While our current approach to lineshape simulation is ‘correct’ in that it treats the sixty-level quantum mechanical system of our atoms without obvious error, it is not entirely complete. In particular, if our interest is in simulating lineshapes, we must account for all relevant physical processes, one of which is due to *spontaneous emission*. Though in a two level system we can easily account for this effect by adding a homogenous linewidth corresponding to lifetime broadening (section 2.2.2), in our more complicated system the effect of these decays is not so obvious.<sup>2</sup>

One rather simplistic approach to treating spontaneous emission is to consider it in terms of probability losses, whereby the total probability of the system decreases over time – this occurs, in our case, if the majority of spontaneous emission results from decay to states *outside* the sixty levels under consideration. In this case, for the states which spontaneously decay (i.e all but the  $5P_{1/2}$  ground states) we simply make the replacement

$$E_n \rightarrow E_n - \frac{i\Gamma_n}{2} ,$$

where  $E_n$  is the energy of state  $|n\rangle$  and  $\Gamma_n$  is its decay rate [37].

Unfortunately, in our system it appears that many decay pathways return to the same lower states, meaning that the easy approach does not apply. To effectively account for spontaneous emission in our lineshape simulations we will then have to resort to a more complicated (and rigorous) formulation of the process using density matrices. We leave this challenging problem to the future reader.

Finally, it would be worth considering the effect of the lock-in amplifier on our lineshapes. Because of the finite time constant used to reduce noise in the signal, we might consider a means of accounting for a ‘smoothing’ of closely spaced and only barely resolved peaks as a result of such filtering. Again, we leave this problem for future consideration.

Our last extension to the theoretical method outlined in section 3.2.2 and appendix B.2.2 is to consider arbitrary polarizations rather than the linear ones assumed in the present work. While an idealized version of our experimental setup would allow for perfectly linear laser polarizations, imperfections in our optics necessarily lead to inhomogeneous phase shifts between various components of light. Our beams must then in general be described as *elliptically* polarized. To account mathematically for this, we decompose our polarization in the spherical basis (equation B.23) so that it becomes a sum of linear, right-circular, and left-circular polarizations, described by coefficients  $c_q$ :

$$\vec{\varepsilon} = \varepsilon(c_{-1}\hat{e}_{-1} + c_0\hat{e}_0 + c_1\hat{e}_1)$$

The dipole matrices in equation B.27 then become, in this most general case,

$$\langle F'm'_F | \mathbf{d}_{mn} | Fm_F \rangle = c_0 d_{mnF'm'_FFm_F,0} + c_{-1} d_{mnF'm'_FFm_F,-1} + c_1 d_{mnF'm'_FFm_F,+1} \quad (6.1)$$

---

<sup>2</sup>For one, there are multiple decay pathways from the excited states in our system, some of which are to states *outside* the system.

with dipole matrix elements  $d$  given in equation B.25. With this formulation, we can consider arbitrary elliptical polarizations in order to properly treat imperfections in our laser polarization.

### Consideration of Extraction Methods

With a set of numerical simulation tools in place, we turn to the problem of actually extracting tensor polarizabilities from our data. One preliminary attempt is detailed in appendix B.3. While this nicely exemplifies the methods we intend to employ in this work going forward, its approach – to measure the splitting between the  $|4, 4\rangle$  and ‘composite’ peaks at high field near 15 kV/cm – is probably intractable because of a quick divergence in the  $\alpha_2$  error bar for even modest uncertainties in the measured splitting. In all likelihood, we will need to develop another method of extraction.

One approach is to look for another splitting to measure, using the  $|4, 4\rangle$ –‘Composite’ and this other (as-yet-undetermined) splitting in a complementary manner. In particular, each will likely yield its own value for the tensor polarizability, with some error bar. If there is a range within the error bar of each in which the tensor polarizabilities from both splittings agree, we can use this range of agreement to narrow down the true value of the tensor polarizability.

Consulting figure 3.2, we notice that there is no other splitting we can find involving one fully resolved component. The next best thing is to at least avoid the large cluster of  $F = 5$  and  $F = 6$  levels at higher energies. To do so, we can switch to the  $F = 5 \rightarrow F' = 4$  first-step lock and excite the  $F'' = 3, 4, 5$  hyperfine levels in the  $7P_{3/2}$  state. This leaves a spectrum with three clusters of peaks, which we label as: (1)  $|4, 4\rangle$  and all  $|3, 3\dots 0\rangle$  sublevels, (2)  $|4, 3\dots 0\rangle$  and  $|5, 5-4\rangle$  sublevels, (3)  $|5, 3\dots 0\rangle$  sublevels. We can then measure, say, the splitting between clusters (2) and (3), performing lineshape corrections like those described in section B.3 to roughly locate a single sublevel. From there, we can then extract a tensor polarizability by diagonalizing the relevant matrices and numerically solving. Comparing values extracted from these various splittings will hopefully allow us to more precisely pinpoint a value for the tensor polarizability.

# Appendix A

## Atomic Units, Polarizabilities, and Corrections to the Literature

In this brief appendix we discuss the system of atomic units (a.u.) preferred by AMO theorists for its convenient numerical properties. Unfortunately, conversions between experimentally-necessary SI units and the former are not quite trivial, and because we quote polarizability results in atomic units the system merits a brief treatment.

The system simplifies numerical calculations by setting four common quantities equal to one:

Dimension	Quantity	Symbol
Mass	Electron Mass	$m_e$
Charge	Elementary Charge	$e$
Angular Momentum	Plank's Constant (Reduced)	$\hbar$
Electric Constant	Coulomb Force Constant	$1/(4\pi\epsilon_0)$

**Table A.1:** The four quantities taken to be one in atomic units. Reproduced from [33].

Various combinations of these four quantities can be used to form any other unit of interest. In particular, one finds a natural unit of length

$$a_0 = \frac{(4\pi\epsilon_0)\hbar^2}{m_e e^2} \text{ (Bohr Radius)} \quad (\text{A.1})$$

and a natural unit of energy

$$E_H = \frac{m_e e^4}{(4\pi\epsilon_0)^2 \hbar^2} = \frac{e^2}{(4\pi\epsilon_0) a_0} \text{ (Hartree Energy).} \quad (\text{A.2})$$

To express the polarizability in atomic units, we first recall that its natural units are  $(\text{Energy})/(\text{Electric Field})^2$ . Noting that the combination of atomic units resulting in electric field is  $e/(4\pi\epsilon_0)a_0^2$ , this gives a unit of polarizability:

$$E_H \left( \frac{(4\pi\epsilon_0)a_0^2}{e} \right)^2 = \frac{e^2}{(4\pi\epsilon_0)a_0} \frac{(4\pi\epsilon_0)^2 a_0^4}{e^2} = (4\pi\epsilon_0)a_0^3. \quad (\text{A.3})$$

Evidently, in atomic units, the polarizability is proportional to the cube of the Bohr radius. In practice, polarizabilities are quoted in units of  $a_0^3$ , dropping the electric coefficient for cleanliness. To convert to our preferred experimental units,  $\text{kHz}/(\text{kV/cm})^2$ , we simply plug in SI values in equation A.3, divide by  $h$  to put the numerator in units of frequency, and multiply by the requisite powers of ten. This results in conversion factors

$$1 \ a_0^3 = 0.248832 \frac{\text{kHz}}{(\text{kV/cm})^2} \quad (\text{A.4})$$

$$1 \ \frac{\text{kHz}}{(\text{kV/cm})^2} = 4.01878 \ a_0^3. \quad (\text{A.5})$$

We note that there is a factor of two in the definition of polarizability (equation 3.3) that one must heed when converting between Stark shifts in SI and polarizabilities in a.u.<sup>1</sup> The conversion factors found above agree with those seen in [26], but *not* with a series of previous Majumder group theses and publications including [13, 19, 25, 33]. This rather unfortunate oversight suggests that corrections are necessary in two recent group publications, which quote the correct SI Stark shift but convert to atomic units incorrectly. Table A.2 lists the relevant corrected values, derived following precisely the discussions in [13, 19] but with appropriate conversion factors.

Paper	Quantity	Value
Ranjit <i>et. al.</i> (2013) [19]	$k_S$	$-122.92(33) \ \text{kHz}/(\text{kV/cm})^2$
	$\Delta\alpha_0$	$988.0(2.7)a_0^3$
	$\tau(6P_{3/2})$	$57.32(46) \ \text{ns}$
	$\tau(6P_{1/2})$	$64.49(52) \ \text{ns}$
Augenbraun <i>et. al.</i> (2016) [13]	$k_S$	$-813.7(4.5) \ \text{kHz}/(\text{kV/cm})^2$
	$\alpha_0(6P_{1/2})$	$7590(37)a_0^3$
	$\langle 5D_{3/2}    d    6P_{1/2} \rangle$	$9.93(6) \ \text{a.u.}$

**Table A.2:** Measured Stark shifts from two recent Majumder group publications, along with corrected values of polarizabilities, lifetimes, and matrix elements derived therein.

---

<sup>1</sup>Accordingly, to convert from a Stark shift in  $\text{kHz}/(\text{kV/cm})^2$  to a polarizability in  $a_0^3$ , one must multiply by twice the factor in equation A.5, or 8.038.

# Appendix B

## Atomic Theory Results

In this appendix we present the mathematical details behind theory results and derivations mentioned in the body of the thesis.

### B.1 Broadened Lineshapes

In the following sections we derive lineshapes and linewidths for the various broadening mechanisms discussed in section 2.2.2 of the thesis.

#### B.1.1 Doppler Broadening

The most dominant source of broadening in our single step vapor cell transitions arises from the Doppler effect, wherein an absorption line is broadened due to the statistical variation in atomic velocities along the incident laser radiation. Following [38], we assume this spread of atomic velocities to follow Maxwell-Boltzmann statistics. Accordingly, we can write down an expression for the number density of atoms with velocities between  $v$  and  $v + dv$ :

$$n(v)dv = \frac{N}{\sqrt{\pi}} \sqrt{\frac{m}{2kT}} e^{-mv^2/2kT} dv , \quad (\text{B.1})$$

where  $N$  is the density of *all* atoms in the relevant state,  $m$  is the atomic mass,  $T$  is the temperature, and  $k$  is the Boltzmann constant.

We now retrieve the familiar first-order Doppler relation between speed and frequency (equation 2.8),

$$\omega_{\text{atom}} = \omega_{\text{laser}} \left(1 - \frac{v_z}{c}\right) ,$$

where  $\omega_{\text{laser}}$  is the laser frequency in the lab frame,  $v_z$  is the speed of a given atom with respect to the laser propagation direction, and  $\omega_{\text{atom}}$  is the observed frequency in the atom frame. We can, of course, rewrite this Doppler relation in a manner more enlightening for our purposes. Namely, if  $\omega_0$  is the atomic resonance, we require an incident laser frequency of

$$\omega = \omega_0 \left(1 + \frac{v_z}{c}\right) \quad (\text{B.2})$$

for absorption to occur.

Substituting equation B.2 into the Maxwell distribution (equation B.1 above) yields a distribution for the number density of atoms per unit *frequency* in the interval  $\omega$  to  $\omega + d\omega$ :

$$n(\omega)d\omega = \frac{N}{\sqrt{\pi}} \frac{c}{\omega_0} \sqrt{\frac{m}{2kT}} e^{-mc^2(\omega-\omega_0)^2/2kT\omega_0^2} d\omega .$$

Of course, the number of atoms on resonance per unit frequency is proportional to the absorbed laser power, and we can then write an expression for transmitted intensity,

$$I(\omega) = I_0 e^{-mc^2(\omega-\omega_0)^2/2kT\omega_0^2} , \quad (\text{B.3})$$

which is a Gaussian with full width at half maximum

$$\Delta = 2\sqrt{\ln 2}\sigma = \frac{\omega_0}{c} \sqrt{\frac{8kT \ln 2}{m}} . \quad (\text{B.4})$$

### B.1.2 Lifetime Broadening

We now consider the origin of the so-called ‘natural linewidth,’ a finite limit on the width of a resonance given by the uncertainty principle. Once again following [38], we begin by considering a classical model of atom-light interactions. Specifically, we treat the excited electron as a damped harmonic oscillator (with charge  $e$ , mass  $m$ , damping constant  $b$ , and resonance frequency  $\omega_0 = \sqrt{k/m}$ ) driven by laser radiation with electric field amplitude  $E_0$ :

$$m\ddot{x} + b\dot{x} + kx = qE_0 e^{i\omega t} .$$

This is solved by the expression

$$x = \frac{qE_0 e^{i\omega t}}{m(\omega_0^2 - \omega^2 + i\gamma\omega)} , \quad (\text{B.5})$$

where here  $\gamma = b/m$ . In particular, because the damping of such an oscillator is related to decays from the upper state with characteristic lifetime  $\tau$ ,  $\gamma$  is equal to  $1/\tau$  as in section 2.2.2.

We now recall a bit of electrostatics. First we note that the induced dipole moment in the atom due to the oscillating charge described above is given by

$$\vec{p} = q\vec{x} . \quad (\text{B.6})$$

Next, we consider the *total* polarization,  $\vec{P}$ , which can be expressed as a sum of all dipole moments per unit volume:

$$\vec{P} = N\vec{p} = \epsilon_0(\epsilon - 1)\vec{E} , \quad (\text{B.7})$$

where  $N$  is the number of oscillating charges per unit volume and  $\epsilon$  is the relative dielectric constant (the latter equality reflects another standard expression for the total

polarization). Finally, we combine equations B.5-B.7 to find an index of refraction for the atomic sample

$$n(\omega) \approx \epsilon^{1/2} \approx 1 + \frac{Nq^2}{2\epsilon_0 m(\omega_0^2 - \omega^2 + i\gamma\omega)}, \quad (\text{B.8})$$

where we have used the relations  $n = \sqrt{\epsilon\mu}$  with  $\mu \approx 1$  for most media, as well as taken  $n^2 - 1 = (n+1)(n-1) \approx 2(n-1)$  for  $n$  close to 1.

Finally, we recall that *absorption* is proportional to the imaginary part of this (complex) index of refraction<sup>1</sup>. Accordingly, we find a function for the absorption of light,

$$\alpha(\omega) = \frac{Nq^2}{c\epsilon_0 m} \frac{\gamma\omega}{(\omega_0^2 - \omega^2)^2 + \gamma^2\omega^2},$$

which reduces, near an atomic resonance where  $|\omega_0 - \omega| \ll \omega_0$ , to

$$\alpha(\omega) = \frac{Ne^2}{4\epsilon_0 mc} \frac{\gamma/2}{(\omega_0 - \omega)^2 + (\gamma/2)^2}. \quad (\text{B.9})$$

This is a *Lorentzian* profile, with full width at half maximum

$$\gamma = \frac{1}{\tau}$$

for transitions to a state with lifetime  $\tau$ .

### B.1.3 Power Broadening

We finally consider the further broadening of absorption lines due to finite laser power. Once again, this brief derivation follows the discussion in [38].

We begin by considering a two-level system, with the transition between states  $|a\rangle$  and  $|b\rangle$  having a natural linewidth  $\gamma$ . We introduce laser radiation with electric field amplitude  $E_0$  and frequency  $\omega$ , which induces Rabi oscillations of resonant frequency  $\Omega_R$  between states in the system. Without derivation, we quote the probability of populating the upper state,  $|b\rangle$ , under such circumstances [38]:

$$|b(\omega, t)|^2 = \frac{\Omega_R^2}{(\omega_{ab} - \omega)^2 + \Omega_R^2} \times \sin^2 \left( \frac{1}{2} \sqrt{(\omega_{ab} - \omega)^2 + \Omega_R^2} t \right). \quad (\text{B.10})$$

Though this result is quoted without derivation, we can make some sense of its form. The time-independent part is a Lorentzian characterizing the probability of excitation as a function of laser frequency. The sinusoidal term represents oscillations between states. These occur at precisely  $\Omega_R/2$  on resonance and at greater frequencies for off-resonant laser radiation.

---

<sup>1</sup>The real part is related to *dispersion*.

We now take into consideration the finite lifetime of state  $|b\rangle$ ,  $\tau = 1/\gamma$ , and evaluate the resulting *mean* probability of  $|b\rangle$  being populated:

$$P_b(\omega) = \langle |b(\omega, t)|^2 \rangle = \int_0^\infty \gamma e^{-\gamma t} |b(\omega, t)|^2 dt . \quad (\text{B.11})$$

This integral results in a lineshape of the form:

$$P_b(\omega) = \frac{1}{2} \frac{\Omega_R^2}{(\omega_{ab} - \omega)^2 + \gamma^2(1 + S)} , \quad (\text{B.12})$$

a Lorentzian with width

$$\gamma_{\text{Power}} = \gamma\sqrt{1 + S} , \quad (\text{B.13})$$

where  $S = \Omega_R^2/\gamma^2$ .

## B.2 Many-Level Systems

### B.2.1 The Wigner-Eckart Theorem and Polarization Selection Rules

In the course of our lineshape simulation work in the  $7P_{3/2}$  state of indium, it became apparent that knowledge of *relative* transition amplitudes of various magnetic hyperfine sublevels,  $m_F$ , would be critical to a complete understanding of the problem and its solutions. Luckily, this is a problem with a simple solution: application of the *Wigner-Eckart theorem*. Below, we briefly motivate and present this important theorem specifically as it relates to the dipole operator describing atomic transitions.

We begin by recalling the standard formulation for coupling between two angular momenta. Given coupled angular momenta  $\vec{J}_1$  and  $\vec{J}_2$ , we can define the *total* angular momentum

$$\vec{J} = \vec{J}_1 + \vec{J}_2 , \quad (\text{B.14})$$

the eigenvalues of which obey the usual constraints:  $|J_1 - J_2| \leq J \leq J_1 + J_2$  and  $M = M_1 + M_2$ . We can then express coupled basis states,  $|JM\rangle$ , in terms of the uncoupled basis states according to:

$$\begin{aligned} |JM\rangle &= \sum_{M_1, M_2} |J_1 M_1\rangle |J_2 M_2\rangle \langle J_1 M_1, J_2 M_2| JM\rangle \\ &= \sum_{M_1, M_2} |J_1 M_1\rangle |J_2 M_2\rangle (-1)^{J_1 - J_2 + M} \sqrt{2J + 1} \begin{pmatrix} J_1 & J_2 & J \\ M_1 & M_2 & -M \end{pmatrix} \end{aligned} \quad (\text{B.15})$$

where the first of these (completely equivalent) formulations is in terms of the Clebsch-Gordan coefficients, and the second is written in terms of 3-j symbols (see, for instance, appendix A.2 of [37]).

Now we imagine something similar (though perhaps strange-sounding): coupling an operator,  $\hat{T}_q^k$ , with an angular momentum basis state to form a new state, which

we will call  $|\beta KQ\rangle$ .<sup>2</sup> We then find a change of basis analogous to that of equation B.15:

$$|\beta KQ\rangle = \sum_{q,M} \hat{T}_q^k |\gamma JM\rangle \langle JM, kq | KQ \rangle \quad (\text{B.16})$$

We can invert this relation in the standard way,

$$\hat{T}_q^k |\gamma JM\rangle = \sum_{K,Q} |\beta KQ\rangle \langle JM, kq | KQ \rangle ,$$

and then take matrix elements in the  $J$  basis:

$$\begin{aligned} \langle \gamma' J' M' | \hat{T}_q^k | \gamma JM \rangle &= \sum_{K,Q} \langle \gamma' J' M' | \beta KQ \rangle \langle JM, kq | KQ \rangle \\ &\propto \langle JM, kq | J' M' \rangle , \end{aligned} \quad (\text{B.17})$$

where the proportionality results from the orthogonality of the  $J$  basis states – i.e. the sum ‘picks out’  $|KQ\rangle = |J'M'\rangle$ . It turns out that the proportionality constant is related to the *reduced matrix element*, given by

$$|\langle \gamma' J' || \hat{T}^k || \gamma J \rangle|^2 = \sum_{MM'q} |\langle \gamma' J' M' | \hat{T}_q^k | \gamma JM \rangle|^2 , \quad (\text{B.18})$$

so that proportionality B.17 becomes

$$\langle \gamma' J' M' | \hat{T}_q^k | \gamma JM \rangle = \frac{\langle \gamma' J' || \hat{T}^k || \gamma J \rangle}{\sqrt{2J' + 1}} \langle JM, kq | J' M' \rangle$$

(B.19)

This is the Wigner-Eckart theorem, and its beauty is that it reduces the problem of calculating  $(2J + 1)(2J' + 1)$  angular momentum-basis matrix elements to one of finding a *single* reduced matrix element. The remaining pieces can then be simply evaluated by application of the Clebsch-Gordan coefficients.

It turns out that  $\hat{T}_q^k$  is an *irreducible tensor operator* of rank  $k$ , defined by a set of transformation properties that we will not detail here.<sup>3</sup> The standard electric dipole operator used to describe E1 atomic transitions is, conveniently, such an operator – with rank  $k = 1$  – and so equation B.19 becomes, for this specific case:

$$\langle \gamma' J' M' | D | \gamma JM \rangle = \frac{\langle \gamma' J' || D || \gamma J \rangle}{\sqrt{2J' + 1}} \langle JM, 1 q | J' M' \rangle \quad (\text{B.20})$$

---

<sup>2</sup>This treatment is based on one found in appendix A of [37]. Though this notation is currently a bit cryptic, it will later make some amount of sense. If a bit more concreteness is desired, it is nice to know that we will ultimately take  $\hat{T}_q^k$  to be the electric dipole operator and the state  $|\beta KQ\rangle$  to be the one excited in a dipole transition.

<sup>3</sup>See any advanced quantum mechanics text, or something similar like [37], for details.

Here,  $q$  is related to the polarization of the exciting radiation in the following way:<sup>4</sup>

$$\begin{aligned}\sigma^+ \rightarrow q = +1 && (\text{Right-circular polarization, } \Delta M = +1) \\ \pi \rightarrow q = 0 && (z \text{ polarization, } \Delta M = 0) \\ \sigma^- \rightarrow q = -1 && (\text{Left-circular polarization, } \Delta M = -1)\end{aligned}$$

One way to think of this is in terms of the addition of photon and atomic angular momenta. Photons are spin-1, and (for example)  $\sigma^+$  photons have  $M_{\sigma^+} = +1$ , so absorption of a  $\sigma^+$  photon by state  $|JM\rangle$  yields a state with  $M' = M + 1$ .<sup>5</sup> Indeed, the Clebsch-Gordan coefficients go to zero unless  $M' = M + q$  and therefore convey in mathematical terms this physically-motivated selection rule.

This gives us the tools we need to predict relative transition probabilities of magnetic sublevels for a given total angular momentum state. Namely, regardless of the value of the reduced dipole matrix element, relative line strengths for a given polarization can be found by simply squaring the Clebsch-Gordan coefficients in equation B.20. This proves an invaluable tool for the lineshape simulation work described in chapter 3.

### B.2.2 The Generalized Three-Level Hamiltonian

In this section we derive the Hamiltonians used in our theory work in chapter 3 (equations 3.8 and 3.15). A similar derivation was detailed in [25]; here we generalize from the purely three-level system of that work to a two-laser system with three gross levels but many sublevels.

We begin by writing down the Hamiltonian, perhaps in the presence of an electric field but free of laser radiation, for our atomic system. In the hyperfine basis given by  $|nLJFm_F\rangle$ , it is block diagonal and takes the form

$$H_0 = \begin{pmatrix} \mathbf{E}_1 & 0 & 0 \\ 0 & \mathbf{E}_2 & 0 \\ 0 & 0 & \mathbf{E}_3 \end{pmatrix} \quad (\text{B.21})$$

where the  $\mathbf{E}_n$  matrices represent energies of the three ‘gross’ states  $|nLJ\rangle$ .<sup>6</sup> They are often diagonal, and for  $J = 1/2$  simply take the form  $(E_n^{(0)} - \frac{1}{2}\alpha_0(n)\mathcal{E}^2)\mathbb{I}$ , where  $E_n^{(0)}$  is the unperturbed energy of the state. For the indium  $7P_{3/2}$  state, however,  $\mathbf{E}_3$  is given by equation 3.7 (plus a term defining the field-free hyperfine splitting) and is not diagonal due to Stark mixing of hyperfine levels.

We next apply two laser fields of near-resonant light,  $\omega_1 \approx (E_2 - E_1)/\hbar$  and  $\omega_2 \approx (E_3 - E_2)/\hbar$ , with electric field amplitudes  $\vec{\epsilon}_1$  and  $\vec{\epsilon}_2$ , respectively. This leads

<sup>4</sup>These relations become clear when we write  $D$  in the spherical basis (see equations B.23 below), though this section has dragged on enough already and so we will spare the details.

<sup>5</sup>More generally, for absorption of a photon with  $M_\gamma = q$ , the new state has  $M' = M + q$ .

<sup>6</sup>We only include one  $F$  level for each of states 1 and 2, but because of the Stark-induced hyperfine mixing in state 3, we need all  $F$  levels there.

to an interaction Hamiltonian given by

$$H_{\text{int}} = \vec{\varepsilon}_1 \cdot \mathbf{d} \cos(\omega_1 t) + \vec{\varepsilon}_2 \cdot \mathbf{d} \cos(\omega_2 t) = \vec{\varepsilon}_1 \cdot \mathbf{d} e^{i\omega_1 t} + \vec{\varepsilon}_2 \cdot \mathbf{d} e^{i\omega_2 t} + \text{c.c.} \quad (\text{B.22})$$

where  $\mathbf{d} = -\sum_i e\mathbf{r}_i$  is the electric dipole operator.

In order to write down the  $\vec{\varepsilon} \cdot \mathbf{d}$  matrix elements, we first decompose the  $\vec{\varepsilon}_n$ 's in the so-called spherical basis:

$$\begin{aligned} \hat{e}_{q=1} &= -\frac{1}{\sqrt{2}}(\hat{e}_x + i\hat{e}_y) && (\sigma^+ \text{ polarization}) \\ \hat{e}_{q=0} &= \hat{e}_z && (\pi \text{ polarization}) \\ \hat{e}_{q=-1} &= \frac{1}{\sqrt{2}}(\hat{e}_x - i\hat{e}_y) && (\sigma^- \text{ polarization}). \end{aligned} \quad (\text{B.23})$$

Assuming linearly polarized light<sup>7</sup> at an angle  $\theta$  from the  $z$  axis, this decomposition yields.

$$\begin{aligned} \vec{\varepsilon} &= \varepsilon \cos \theta \hat{e}_z + \varepsilon \sin \theta \hat{e}_x \\ &= \varepsilon \cos \theta \hat{e}_0 + \frac{\varepsilon}{\sqrt{2}} \sin \theta (\hat{e}_{-1} - \hat{e}_1) \\ &= \cos \theta \vec{\varepsilon}_0 + \frac{1}{\sqrt{2}} \sin \theta (\vec{\varepsilon}_{-1} - \vec{\varepsilon}_1) \end{aligned} \quad (\text{B.24})$$

In view of the Wigner-Eckart theorem (section B.2.1), we know that the matrix elements of  $H_{\text{int}}$  will be related to a reduced dipole matrix element multiplied by a Clebsch-Gordan coefficient (or, equivalently,<sup>8</sup> a three-j symbol). Because reduced dipole matrix elements are typically written in the  $|J\rangle$  basis, we need some way to convert into our  $|F\rangle$  basis. It turns out that this is accomplished by way of a 6-j symbol (see appendix A.3 of [37]), so that

$$\begin{aligned} \langle \gamma' F' m'_F | \vec{\varepsilon}_q \cdot \mathbf{d} | \gamma F m_F \rangle &= \varepsilon \langle \gamma' J' || d || \gamma J \rangle (-1)^{I+J+F+1} \sqrt{(2F+1)(2F'+1)} \left\{ \begin{matrix} J & 1 & J' \\ F' & I & F \end{matrix} \right\} \\ &\times (-1)^{F-M} \left( \begin{matrix} F & 1 & F' \\ -m_F & q & m'_F \end{matrix} \right) \\ &\equiv \varepsilon d_{\gamma' J' \gamma J F' m'_F F m_F, q} \end{aligned} \quad (\text{B.25})$$

where the 3-j symbol plays the role of the Clebsch-Gordan coefficient in the Wigner-Eckart theorem of equation B.19, and  $I = 9/2$  for indium.

Returning to equation B.22, we now write  $H_{\text{int}}$  in matrix form. It is 0 on the diagonals because the lasers induce no interaction between an eigenstate and itself,

---

<sup>7</sup>The beams begin linearly polarized and interact exclusively with  $\lambda/2$  plates and other optics that, in principle, can at most rotate this linear polarization. That said, there is certainly some degradation of polarization due to imperfect optics. We'll ignore this unpolarized (or at least elliptically polarized) background for present purposes.

<sup>8</sup>Up to a sign, of course.

and there is no dipole mixing between states  $|1\rangle$  and  $|3\rangle$  by  $\Delta l$  selection rules (even if these weren't dipole-excluded, the lasers are so far off the 1-3 resonance that those off-diagonal elements would be nearly zero anyway). Accordingly, equation B.22 becomes

$$H_{\text{int}} = (\varepsilon_1 e^{i\omega_1 t} + \varepsilon_2 e^{i\omega_2 t} + \text{c.c.}) \begin{pmatrix} 0 & \mathbf{d}_{21} & 0 \\ \mathbf{d}_{21}^\dagger & 0 & \mathbf{d}_{32} \\ 0 & \mathbf{d}_{32}^\dagger & 0 \end{pmatrix} \quad (\text{B.26})$$

where the dipole matrices,  $\mathbf{d}_{mn}$ , are composed of the dipole matrix elements in equation B.25 such that

$$\langle F'm'_F | \mathbf{d}_{mn} | Fm_F \rangle = \cos \theta d_{mnF'm'_FFm_F,0} + \frac{\sin \theta}{\sqrt{2}} (d_{mnF'm'_FFm_F,-1} - d_{mnF'm'_FFm_F,+1}) \quad (\text{B.27})$$

We now have a Hamiltonian given by  $H_{\text{full}} = H_0 + H_{\text{int}}$ . To simplify it into a somewhat tractable form, we adopt the standard practice of transforming into a rotating frame and employing the rotating wave approximation. In particular, we define a unitary operator,

$$\hat{U}_0 = \begin{pmatrix} \mathbb{I} & 0 & 0 \\ 0 & e^{-i\omega_1 t} \mathbb{I} & 0 \\ 0 & 0 & e^{-i(\omega_1 + \omega_2)t} \mathbb{I} \end{pmatrix}, \quad (\text{B.28})$$

and new set of ‘rotating’ eigenstates,  $|\phi\rangle$ , such that  $|\psi\rangle = \hat{U}_0 |\phi\rangle$ . We can then solve for these new eigenstates and energies by inserting the latter relation into the time-dependent Schrödinger equation for  $|\psi\rangle$ , so that

$$i\hbar \left( \frac{\partial \hat{U}_0}{\partial t} |\phi\rangle + \hat{U}_0 \frac{\partial |\phi\rangle}{\partial t} \right) = H_{\text{full}} \hat{U}_0 |\phi\rangle \quad (\text{B.29})$$

Rearranging gives us an effective Schrödinger equation for  $|\phi\rangle$ :

$$i\hbar \frac{\partial |\phi\rangle}{\partial t} = H_{\text{eff}} |\phi\rangle, \quad (\text{B.30})$$

where

$$H_{\text{eff}} = \hat{U}_0^\dagger H_{\text{full}} \hat{U}_0 - i\hbar \hat{U}_0^\dagger \frac{\partial \hat{U}_0}{\partial t} = H_0 + \hat{U}_0^\dagger H_{\text{int}} \hat{U}_0 - i\hbar \hat{U}_0^\dagger \frac{\partial \hat{U}_0}{\partial t} \quad (\text{B.31})$$

(since  $[H_0, \hat{U}_0] = 0$ ). We can then simply do out the matrix multiplications, which without too much difficulty simplify to

$$H_{\text{eff}} = \begin{pmatrix} \mathbf{E}_1 & 0 & 0 \\ 0 & \mathbf{E}_2 - \hbar\omega_1 & 0 \\ 0 & 0 & \mathbf{E}_3 - \hbar(\omega_1 + \omega_2) \end{pmatrix} + (\varepsilon_1 e^{i\omega_1 t} + \varepsilon_2 e^{i\omega_2 t} + \text{c.c.}) \begin{pmatrix} 0 & e^{-i\omega_1 t} \mathbf{d}_{21} & 0 \\ e^{i\omega_1 t} \mathbf{d}_{21}^\dagger & 0 & e^{-i\omega_2 t} \mathbf{d}_{32} \\ 0 & e^{i\omega_2 t} \mathbf{d}_{32}^\dagger & 0 \end{pmatrix} \quad (\text{B.32})$$

Because  $\omega_1$  and  $\omega_2$  are large and far-detuned from one another, we now invoke the rotating wave approximation and drop terms oscillating at  $2\omega_1$ ,  $2\omega_2$ ,  $\omega_1 + \omega_2$ , and  $\omega_1 - \omega_2$ . The result is a much-simplified Hamiltonian that takes the form

$$H_{\text{RWA}} = \begin{pmatrix} \mathbf{E}_1 & \varepsilon_1 \mathbf{d}_{21} & 0 \\ \varepsilon_1 \mathbf{d}_{21}^\dagger & \mathbf{E}_2 - \hbar\omega_1 & \varepsilon_2 \mathbf{d}_{32} \\ 0 & \varepsilon_2 \mathbf{d}_{32}^\dagger & \mathbf{E}_3 - \hbar(\omega_1 + \omega_2) \end{pmatrix} \quad (\text{B.33})$$

Now we do some cleanup, first for the  $7P_{3/2}$  state, then for the  $7P_{1/2}$ .

### $7P_{3/2}$ Hamiltonian

Here, we have the mapping  $|1\rangle \rightarrow 5P_{1/2}(F=4)$ ,  $|2\rangle \rightarrow 6S_{1/2}(F'=5)$ , and  $|3\rangle \rightarrow 7P_{3/2}(F''=3,4,5,6)$ . For the lower two states, we separate the unperturbed diagonal energies from the (scalar component of) the Stark shift, so that  $E_n = E_n^{(0)} + \delta_n$ , where  $\delta_n = -\frac{1}{2}\alpha_0(n)\mathcal{E}^2$ .  $\mathbf{E}_3$ , meanwhile, can be split into several components. The first is the hyperfine Hamiltonian,  $V_{\text{hf}}$ , which tells us the (field-free) energy differences between  $E_3^{(0)}$  and the  $F'' = 3, 4, 5, 6$  hyperfine levels.<sup>9</sup>

Next, we separate the effect of the tensor polarizability from the scalar polarizability. In particular, we define  $V_{\text{tens}}$  as given by (from equation 3.7)

$$\langle Fm_F | V_{\text{tens}} | F'm_F \rangle = -\frac{1}{2}\alpha_2\mathcal{E}^2 \langle Fm_F | Q | F'm_F \rangle \quad (\text{B.34})$$

The remainder of equation 3.7 captures the scalar polarizability, which we add in as  $\delta_3$ .

We also note that  $\varepsilon\mathbf{d}$  looks like a Rabi frequency; we can therefore simplify the notation by taking  $\Omega_1 = \varepsilon_1 \mathbf{d}_{21}/\hbar$  and  $\Omega_2 = \varepsilon_2 \mathbf{d}_{32}/\hbar$ .

Since we only care about relative energies, we choose to subtract off  $E_1^{(0)} + \delta_1$  from the diagonal, yielding a matrix of the form:

$$H_{\text{RWA}} = \begin{pmatrix} 0 & \Omega_1 & 0 \\ \Omega_1^\dagger & \mathbf{E}_2^{(0)} - \mathbf{E}_1^{(0)} + (\delta_2 - \delta_1) - \hbar\omega_1 & \Omega_2 \\ 0 & \Omega_2^\dagger & \mathbf{E}_3^{(0)} - \mathbf{E}_1^{(0)} + \mathbf{V}_{\text{hf}} + (\delta_3 - \delta_1) \\ & & + \mathbf{V}_{\text{tens}} - \hbar(\omega_1 + \omega_2) \end{pmatrix} \quad (\text{B.35})$$

Finally, we define the laser detunings,  $\Delta_1 = \hbar\omega_1 - (E_2^{(0)} - E_1^{(0)})$  and  $\Delta_2 = \hbar\omega_2 - (E_3^{(0)} - E_2^{(0)})$ . The final result is given by<sup>10</sup>

$$H_{7P_{3/2}} = \begin{pmatrix} 0 & \Omega_1 & 0 \\ \Omega_1^\dagger & -\Delta_1 + (\delta_2 - \delta_1) & \Omega_2 \\ 0 & \Omega_2^\dagger & -\Delta_2 - \Delta_1 + (\delta_3 - \delta_1) + \mathbf{V}_{\text{hf}} + \mathbf{V}_{\text{tens}} \end{pmatrix}, \quad (\text{B.36})$$

---

<sup>9</sup>The hyperfine Hamiltonian can be found, for instance, in [24]. We use values for the  $a$ ,  $b$ , and  $c$  constants measured over the summer; they are tabulated in appendix E.

<sup>10</sup>Up to a factor of  $\hbar$ , which we now drop so as to express the Hamiltonian in (more convenient) frequency units.

where the first diagonal block is a  $9 \times 9$  matrix, the second diagonal block is an  $11 \times 11$  matrix, and the third diagonal block is a  $40 \times 40$  matrix.

### **7P<sub>1/2</sub> Hamiltonian**

For the  $7P_{1/2}$  state, because we don't need to worry about magnetic sublevels, the problem does reduce to a true three-level system. Accordingly, we take all the 'Rabi matrices' in equation B.36 to scalar Rabi frequencies, defined the usual way (e.g.  $\Omega_1 = \varepsilon_1 d_{21}/\hbar$ ), and reduce the block matrices on the diagonal to scalar quantities. Finally, because we only consider one hyperfine level at a time in this case and there is no tensor polarizability in the  $7P_{1/2}$  state, we drop both the hyperfine and tensor Hamiltonians from the third diagonal in equation B.36. The result:

$$H_{7P_{1/2}} = \begin{pmatrix} 0 & \Omega_1 & 0 \\ \Omega_1 & -\Delta_1 + (\delta_2 - \delta_1) & \Omega_2 \\ 0 & \Omega_2 & -\Delta_2 - \Delta_1 + (\delta_3 - \delta_1) \end{pmatrix} \quad (\text{B.37})$$

## **B.3 Efforts Towards 7P<sub>3/2</sub> Tensor Polarizability Extraction**

As a first significant application of the theory derived above, we here consider one potential approach to the extraction of a tensor polarizability from indium  $7P_{3/2}$  atomic beam data. The most effective means of determining this polarizability is to look at peak splittings for a single value of the electric field. Because the scalar polarizability causes all peaks to shift by the same amount, it drops out; any splittings are therefore due solely to the (well-known) hyperfine Hamiltonian and the effect of the tensor polarizability.

While the obvious choice is to measure a splitting between two fully resolved hyperfine sublevels, the simulation in figure 3.4 shows that there are no two such levels. We therefore turn to the next best option: measuring a splitting between the fully resolved  $|4, 4\rangle$  sublevel and the 'composite' peak (made up of the  $|4, 3\dots 0\rangle$  and  $|5, 5-4\rangle$  levels).

While solving for the analytic lineshapes of these two peaks in our 60-level system is non-trivial at best, and impossible at worst, we can numerically simulate them for different Rabi frequency ratios ( $\Omega_2/\Omega_1$ ), laser polarizations, and electric fields using equations 3.17 and 3.18. Mathematica code for doing so is given in appendix C.

Our problem, of course, is to determine how to extract a tensor polarizability from these atomic spectra. This is always done through use of a program that fits our spectra to some functional form. Here, however, we do not have an analytical form for the observed lineshapes. Instead, we (not quite arbitrarily) *pick* a function and simply fit our peaks. The hope is that whichever function we choose will at least be close to the true lineshape.

It turns out that a Lorentzian lineshape fits the bill rather decently. We use such a function to fit simpler two-step spectra in the Majumder lab (including all vapor

cell data, as well as atomic beam data for the  $7P_{1/2}$  polarizability measurements in this thesis), and its symmetric nature means that it will do a decent job of extracting the observed line center even if the lineshape is wildly non-Lorentzian.

Below we outline the results of such fits for each of the two peaks from which we hope to extract a tensor polarizability. Unless otherwise specified, we assume a Rabi frequency ratio  $\Omega_2/\Omega_1 \approx 1.2$  – roughly what we expect given our experimental laser powers and beam widths, combined with reduced dipole matrix element calculations in [8] – and scale that ratio to give fits whose linewidths accord with those we measure in the laboratory. We also take the scalar and tensor polarizabilities to be the center values given by recent theoretical calculations [22]. Both parameters can be easily modified for future simulation work.

### The Resolved $|\mathbf{F}, \mathbf{m}_\mathbf{F}\rangle = |4, 4\rangle$ Sublevel

The simple peak to simulate and fit, of course, is the fully resolved  $|4, 4\rangle$  level. While it is not, in general, Lorentzian, it is very nearly symmetric in most cases, so that the Lorentzian (a symmetric function) does a tolerable job of extracting its center, typically within 0.5 MHz of the true second-step resonance location. That said, for certain polarizations the Lorentzian fitting method yields a center value well over one MHz away from the expected resonance location; we accordingly hope to find a method to mitigate the potential influence of such extraordinary experimental parameters – after all, in the lab we do not precisely know our laser polarizations and cannot simply choose an optimal value.<sup>11</sup> Figure B.1 gives an example of the way the lineshape differs for different polarizations.

One solution – that which we explore at present – is to take data at a series of polarizations whose *relative* angles with respect to the  $z$  axis are known. In particular, we can rotate the polarization of one our beams by  $90^\circ$  by rotating an associated  $\lambda/2$  plate through a  $45^\circ$  angle. If we accordingly pick out two orthogonal blue polarizations and two orthogonal red polarizations using this method and take data in all *four* possible configurations, we can reduce the error bar on this peak’s location below 0.5 MHz.<sup>12</sup>

Of course, the way to entirely eliminate the need to consider the subtleties of the lineshape is to take data at several fields near 15 kV/cm and measure only shifts in the location of the peak. Because the lineshape does not change so long as we maintain a resonant first-step laser lock, systematic discrepancies in the fitting program’s ability to find the true resonance will subtract out in such a measurement. Looking forward, we might hope to arrive at a means of tensor polarizability extraction that relies on such a differential measurement.

---

<sup>11</sup>We do not precisely know our Rabi frequencies, either, but for present purposes we will restrict our discussion to polarization.

<sup>12</sup>We obtain this conservative value by simulating and fitting spectra for four sets of laser polarizations, comprised of the possible combinations of two ‘types’ of orthogonal polarization:  $\theta_1 = 0$  and  $\theta_2 = \pi/2$ , or  $\theta_1 = \pi/4$  and  $\theta_2 = -\pi/4$ . We expect these four combinations to capture, reasonably well, most types of behavior obtainable within the possible space of orthogonal polarizations.

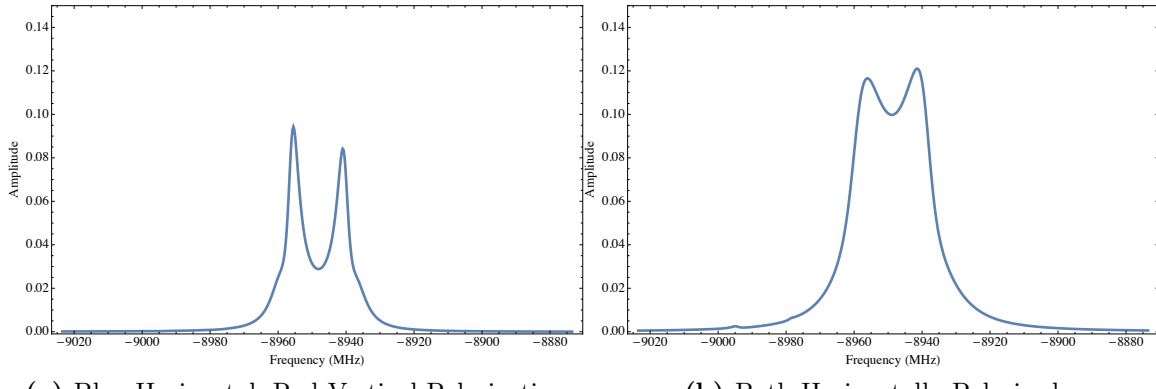


**Figure B.1:** Mathematica simulations of the indium  $7P_{3/2}$ ,  $|F, m_F\rangle = |4, 4\rangle$  lineshape at  $\mathcal{E} = 15$  kV/cm for  $\Omega_2/\Omega_1 = 1.2$  and two sets of laser polarizations. Fitting each to a Lorentzian (which, as the Autler-Townes splitting in the simulations makes clear, does not have the same functional form but is at least symmetric) yields a center value that differs from the expected resonance locations by  $\sim 0.4$  MHz in the mixed-polarization case and  $\sim 0.15$  MHz in the horizontally polarized case.

### The ‘Composite’ Peak

The more challenging work involves the other peak in our hoped-for splitting measurements used to extract a tensor polarizability. This peak is a composite, containing each of the (unresolved)  $|5, 5\rangle$ ,  $|5, 4\rangle$ ,  $|4, 3\rangle$ ,  $|4, 2\rangle$ ,  $|4, 1\rangle$ , and  $|4, 0\rangle$  hyperfine sublevels (see figure B.2).

Here we take the same approach as that employed for the  $|4, 4\rangle$  sublevel – namely, to mitigate the influence of those extraordinary polarizations that lead to atypical fitted peak locations, we take data in four different configurations allowing for two orthogonal polarizations in each laser beam. The added challenge here is that there is no well-defined value we *expect* to observe. One guess might be the mean of the six constituent peak locations, but their asymmetric placement and varying amplitudes makes this value less than robust.

Actually making simulations and fitting those peaks tells a different story: it turns out that it is the location of the  $|F, m_F\rangle = |5, 4\rangle$  peak that most closely captures the behavior of the fit-extracted peak center (see table B.1). From these simulations we find, for  $\mathcal{E} = 15$  kV/cm, that we need simply apply a correction of  $\delta\nu \approx -2.5(6.8)$  MHz to move from the location of the fitted resonance to that of the  $|5, 4\rangle$  resonance.<sup>13</sup>

---

<sup>13</sup>The size of the error bar would indicate that the locations of extracted and predicted resonances are statistically equivalent; we still apply this correction, though, since on average it will improve the agreement of the two values. We have also neglected variations in Rabi frequency and the assumed tensor polarizability at present; a more complete future treatment will also take these into account when assigning an error bar to  $\delta\nu$ .

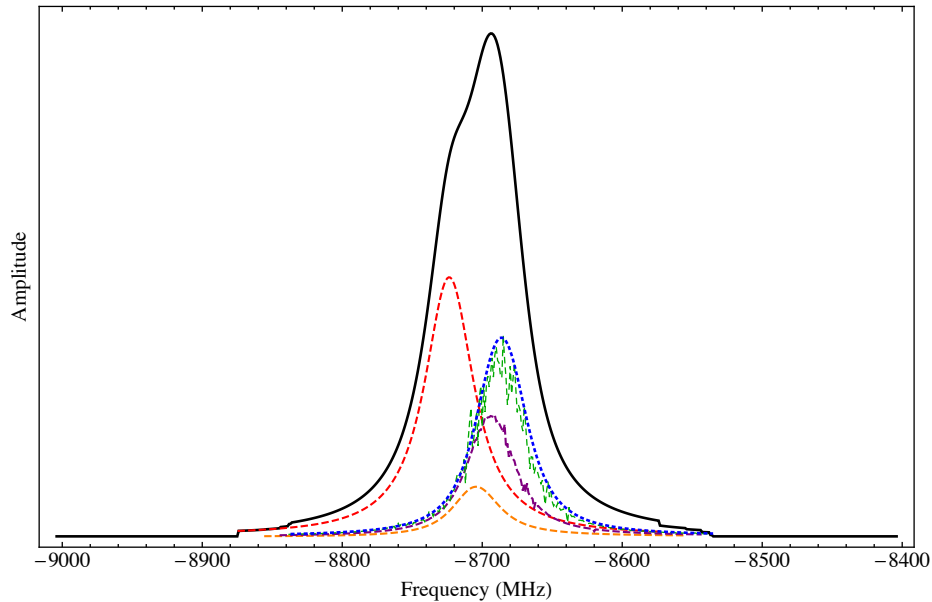


**Figure B.2:** Simulated indium  $7P_{3/2}$  ‘composite’ peak for two vertically polarized lasers at  $\mathcal{E} = 15$  kV/cm. Also shown are the individual constituent peaks:  $|F, m_F\rangle = |5, 5\rangle$  (excluded for this set of polarizations by  $m_F$  selection rules),  $|5, 4\rangle$ ,  $|4, 3\rangle$ ,  $|4, 2\rangle$ ,  $|4, 1\rangle$ , and  $|4, 0\rangle$ .

Polarization	Extracted Val. (MHz)	Diff. from Expected
$\{0, \frac{\pi}{2}\}, \{0, \frac{\pi}{2}\}$	-8714.28	9.28
$\{0, \frac{\pi}{2}\}, \{\frac{\pi}{4}, -\frac{\pi}{4}\}$	-8720.87	2.64
$\{\frac{\pi}{4}, -\frac{\pi}{4}\}, \{\frac{\pi}{4}, -\frac{\pi}{4}\}$	-8726.72	-3.21
$\{\frac{\pi}{4}, -\frac{\pi}{4}\}, \{0, \frac{\pi}{2}\}$	-8722.28	1.23
<b>Mean</b>	-8721.04	2.47
<b>Expected Val.</b>	-8723.51	

**Table B.1:** Averaged fit results to the composite peak for several sets of polarizations,  $\mathcal{E} = 15$  kV/cm. In each row, we simulate the peak for all four possible combinations of polarizations outlined in the left-hand column, and average these four values to get the number in the center column. We then compare with the expected resonance location of the  $|5, 4\rangle$  hyperfine sublevel. Accordingly, for 15 kV/cm data, we can expect to apply a correction of -2.47 MHz, with an error bar of roughly  $9.28 - 2.47 \approx 6.8$  MHz, to go from our extracted peak center to the location of the  $|5, 4\rangle$  resonance.

### Tensor Polarizability Determination

Having extracted a rough value for the difference  $\Delta\nu \equiv \nu(|54\rangle) - \nu(|44\rangle)$ , we now turn to the problem of determining the tensor polarizability. Because both levels have  $m_F = 4$ , we need only consider one  $Q$  matrix from equation 3.7, and because our measurements consist in peak *splittings* only, we can drop the scalar polarizability term. The resulting Hamiltonian (also accounting for hyperfine structure), is given by:

$$\langle F, m_F = 4 | V_{\text{tens,hf}}(\mathcal{E}) | F', m_F = 4 \rangle = \langle F | V_{\text{hf}} | F' \rangle - \frac{1}{2} \alpha_2 \mathcal{E}^2 \langle F, 4 | Q | F', 4 \rangle , \quad (\text{B.38})$$

or

$$V_{\text{tens,hf}}^{(4)}(\mathcal{E}) = \begin{pmatrix} \langle 6 | V_{\text{hf}} | 6 \rangle - \frac{1}{22} \alpha_2 \mathcal{E}^2 & 2\sqrt{\frac{3}{55}} \alpha_2 \mathcal{E}^2 & -\frac{3}{11} \sqrt{\frac{2}{5}} \alpha_2 \mathcal{E}^2 \\ 2\sqrt{\frac{3}{55}} \alpha_2 \mathcal{E}^2 & \langle 5 | V_{\text{hf}} | 5 \rangle + \frac{1}{10} \alpha_2 \mathcal{E}^2 & \frac{1}{5} \sqrt{\frac{6}{11}} \alpha_2 \mathcal{E}^2 \\ -\frac{3}{11} \sqrt{\frac{2}{5}} \alpha_2 \mathcal{E}^2 & \frac{1}{5} \sqrt{\frac{6}{11}} \alpha_2 \mathcal{E}^2 & \langle 4 | V_{\text{hf}} | 4 \rangle + \frac{49}{110} \alpha_2 \mathcal{E}^2 \end{pmatrix} \quad (\text{B.39})$$

We can numerically diagonalize this Hamiltonian to yield energy eigenvalues  $E_4(\alpha_2 \mathcal{E}^2)$ ,  $E_5(\alpha_2 \mathcal{E}^2)$ , and  $E_6(\alpha_2 \mathcal{E}^2)$  corresponding to the  $F'' = 4, 5, 6$  hyperfine levels, respectively. In order to extract a tensor polarizability from  $\Delta\nu$ , the (corrected) splitting between the ‘pure’ and ‘composite’ peaks discussed above, we then numerically solve the equation

$$\Delta\nu = E_5(\alpha_2 \mathcal{E}^2) - E_4(\alpha_2 \mathcal{E}^2) \quad (\text{B.40})$$

for  $\alpha_2$ . This is accomplished by way of a simple Mathematica program.

This result, unfortunately, is not particularly well-behaved. As shown in figure B.3, for errors in our splitting measurement above the true value, the resulting error in  $\alpha_2$  diverges. Specifically, for a value of  $\Delta\nu$  at the  $\sim 3\%$  level (limited by the challenging nature of resonance extraction discussed above), the result for  $\alpha_2$  varies from the true value by 50% at the low end of the error bar up to 350% on the upper end of the error bar. In order to improve upon the current theory error of  $\sim 15\%$  [22], either we need to improve our measurement of  $\Delta\nu$  to under 0.5% or find a new method altogether.

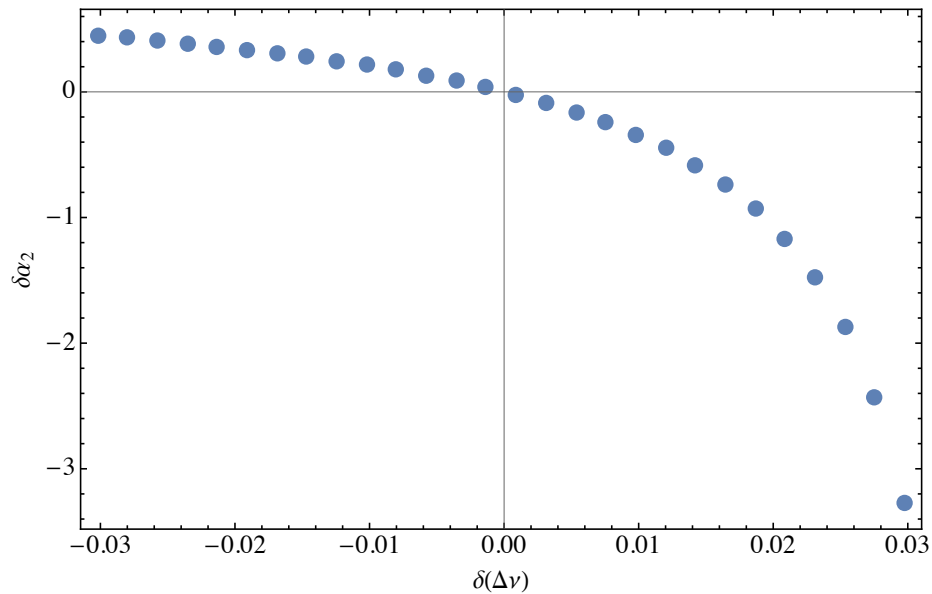


**Figure B.3:** Plot of fractional errors,  $\delta\alpha_2$ , in the extracted tensor polarizability value as a function of  $\delta(\Delta\nu)$ , the fractional error in the ‘pure–composite’ peak splitting whose determination is outlined above. For  $\delta(\Delta\nu) > 0$ ,  $\delta\alpha_2$  quickly diverges – this behavior is untenable unless we can restrict  $\delta(\Delta\nu)$  to under 0.5%.

# Appendix C

## Mathematica Simulations

In this chapter we outline, and provide code samples for, the Mathematica programs used to simulate lineshapes and extract polarizabilities in this thesis. Much of this work requires that we diagonalize reasonably large Hamiltonians, and Mathematica proves a capable tool for doing so. Nearly all of this work is numerical in nature and could, in principle, be done in another program like MATLAB. While doing so would likely make for a worthwhile future project, we experience no significant reductions in speed while adding convenience (at least for the present author) in using Mathematica.

### C.1 Three-Level Lineshapes

Our first significant use of Mathematica code in this thesis is to simulate the three level lineshapes we expect for our  $7P_{1/2}$  data. Such work was carried out two theses ago in [25], and our present code is only slightly modified from that prior implementation. In section 4.3.2 (note 11) we do briefly consider systematic errors due to the imprecision in our knowledge of the first step  $5P_{1/2} \rightarrow 6S_{1/2}$  Stark shift. Here we introduce an error (comparable to the size of the first step  $k_S$  error bar) that leads to a discrepancy between the ‘true’ Stark shift and the 410 nm laser AOM correction. Code for simulating such lines is given in figure C.1. A version of this code can be found on the lab server under the path `Z:\Nathaniel\Lineshape Fit Testing\7PLineshapeTests.nb`. In the same folder is a MATLAB script used to fit these simulated lines to Lorentzians, in order to emulate the behavior of our fitting program for real data.

### C.2 Generalized Three-Level Lineshapes

The majority of the Mathematica work over the course of this thesis went into various considerations of the  $7P_{3/2}$  state, owing to complications arising from the tensor polarizability. We began by writing code to diagonalize the Stark Hamiltonian and make

```

Ez = 5; (* External electric field in kV/cm *)
Ω1 = 10; (* Assumed Rabi frequency for blue laser *)
Ω2 = 15; (* Assumed Rabi frequency for red laser *)
δ21 = -.12292 Ez^2; (* Using value of ks from Nathan Schine -- error bar is 0.00033*)
δ31 = -23.174 Ez^2; (*from Safronova theory*)
err21 = -0.00033; (*error in true value of δ21 (compared to AOM value)*)
Δ1 = δ21; (*assumed 410 nm AOM correction*)
Hrwa[Δ_] :=
  {{0, Ω1, 0},
   {Ω1, (δ21 + err21 * Ez^2) - Δ1, Ω2},
   {0, Ω2, δ31 - Δ - Δ1}}; (* 7P1/2 Hamiltonian, Δ=variable detuning *)

probCompile = {};
Do[
  {vals, vecs} = Eigensystem[Hrwa[Δ]]; (* Numerically find eigensystem *)
  prob3 = Sum[Abs[{0, 0, 1}.vecs[[i]] vecs[[i]].{1, 0, 0}]^2, {i, 1, 3}];
  (*Find t-averaged probability of excitation *)
  AppendTo[probCompile, {Δ, prob3}], (*Compile into a list *)
  {Δ, δ31 - 150, δ31 + 150, 2}];
probFull = Interpolation[probCompile]; (* This is the resonance curve *)
simMax = x /. NMaximize[{probFull[x], δ31 - 50 ≤ x ≤ δ31 + 50}, x][[2]];
(*This is the location of the maximum of the resonance peak *)
Print["simMax = " <> ToString[simMax]];
Print["δ31-δ21 = " <> ToString[δ31 - δ21]];
ListPlot[probCompile, PlotRange → All]

```

**Figure C.1:** Mathematica code used to simulate three level lineshapes for use in, say, the AOM systematic calculations carried out in section 3.2.1. Here we define  $\delta_{21} \equiv \delta_2 - \delta_1$  (and  $\delta_{31}$  similarly). Adapted from [25].

the level splitting diagram in figure 3.2. This is contained in the Mathematica folder on the lab server (`Z:\Nathaniel\Mathematica\`), in the file `Tensor Polarizability Theory and Simulations.nb` (with the relevant code under the heading, “Numerical Approach (for simulation purposes)”).

At present, we briefly describe the code used to implement the 60-level Hamiltonian of section 3.2.2 and simulate the resulting second-step lineshapes. The following is contained in the file, `MultiLevelSystems.nb`.

We begin by defining the Hamiltonian (equation 3.15), which we can hope to do in a slightly more streamlined manner than simply entering all  $60^2$  elements ‘by hand.’ This code is presented in figure C.2. We define each of the blocks of the matrix individually. The first two diagonal blocks are themselves diagonal and admit use of the `IdentityMatrix` command. To form the third diagonal, we use a `Table` command with the  $Q$  matrix (see equation 3.7) from [28] and the hyperfine Hamiltonian from [24] for  $V_{\text{tens}}$  and  $V_{\text{hf}}$ , respectively. The off-diagonal dipole blocks are defined according to equations B.25 and B.27 using the 3-j and 6-j symbols; they can be created using nested `Table` commands. We finally assemble the full Hamiltonian using the `ArrayFlatten` command.

We simulate lineshapes using the same approach as in the three-level case, using a `Do` loop to diagonalize the Hamiltonian for a range of red laser detunings. Using this approach, we can look for the probability of excitation from the ground state (consisting of equal populations in all nine  $m_F$  levels) to *one* excited state,  $|F, m_F\rangle$ . We then use a series of nested `Do` loops to simulate lines for all sublevels; to find the *total* observed lineshape, we add these individual lineshapes, using a command we call `PeaksCombine`. The result is a list, called `FullSpec`, that can be easily plotted with a `ListPlot`. The complete command, which we call `SimSpectrum` (figure C.3), takes as inputs the electric field, the two laser Rabi frequencies (defined as the electric field times the  $J$ -basis reduced dipole matrix element), two scalar polarizability differences ( $\delta\alpha_{021} \equiv \alpha_0(6S_{1/2}) - \alpha_0(5P_{1/2})$ , and  $\delta\alpha_{031} \equiv \alpha_0(7P_{3/2}) - \alpha_0(5P_{1/2})$ ), a tensor polarizability, two laser polarization angles, a step size for detuning calculations, and a range over which to evaluate a given  $m_F$  line. Because of the length of time these calculations take, we typically choose to evaluate each sub-peak over a range about its resonance – the hope is that it will be close enough to zero outside this range that setting it exactly equal to zero at these points (this is what `PeaksCombine` does in part) will have a negligible impact on the overall lineshape. To find the resonance about which to set this range, we use a command called `vselect` which diagonalizes the combined Stark and hyperfine Hamiltonian to determine hyperfine level locations at a given field (figure C.4). While the code in figure C.3 is set up to simulate *all* transitions, it can easily be modified to look at some subset of peaks (e.g. the resolved  $|4, 4\rangle$  peak, or the ‘composite’ peak discussed in section 3.2.2).

```

(*Define the Stark mixing Hamiltonian, Q, as well as the hyperfine Hamiltonian, Vhf*)
QGeneral[F_, Fprime_, M_, J_, i_] := 
$$\left(\frac{(J+1)(2J+1)(2J+3)}{J(2J-1)}\right)^{1/2} (-1)^{i+J+F-Fprime-M} ((2F+1)(2Fprime+1))^{1/2}$$

ThreeJSymbol[{F, M}, {2, 0}, {Fprime, -M}] SixJSymbol[{F, 2, Fprime}, {J, i, J}];
Q[F_, Fprime_, M_] := QGeneral[F, Fprime, M, 3/2, 9/2];
z[f_, i_, j_] := f (f+1) - i (i+1) - j (j+1);
VhfsGeneral[f_, i_, j_, a_, b_, c_] :=

$$\frac{1}{2} a * z[f, i, j] + \frac{3 z[f, i, j] (z[f, i, j] + 1) - 4 i (i+1) j (j+1)}{4 i (2 i - 1) 2 j (2 j - 1)} b +$$


$$\frac{1}{c * i (i-1) (2 i - 1) j (j-1) (2 j - 1)}$$


$$\left(10 \left(\frac{1}{2} z[f, i, j]\right)^3 + 20 \left(\frac{1}{2} z[f, i, j]\right)^2 + z[f, j, i] (-3 i (i+1) j (j+1) + i (i+1) + j (j+1) + 3) -$$


$$5 i (i+1) j (j+1)\right);$$

Vhfs[F_] := VhfsGeneral[F, 9/2, 3/2, 32.18, 22.63, 0.04];

(*define the diagonal blocks of the full Hamiltonian*)
Elmat[F_] := 0 * IdentityMatrix[2 F + 1];
E2mat[Fprime_, Δ1_, δα021_, ε_] := 
$$\left(-\Delta 1 - \frac{1}{2} \delta\alpha021 * \epsilon^2\right) * IdentityMatrix[2 Fprime + 1];
E3mat[M_, Δ1_, Δ2_, δα031_, α2_, ε_] :=
Table[Table[If[F == Fprime, -Δ1 - Δ2 + Vhfs[F] -  $\frac{1}{2} \delta\alpha031 * \epsilon^2$  -  $\frac{1}{2} \alpha2 * \epsilon^2 Q[F, Fprime, M]$ , - $\frac{1}{2} \alpha2 * \epsilon^2 Q[F, Fprime, M]$ ], {F, Max[Abs[M], 3], 6}], {F, Max[Abs[M], 3], 6}];
E3mat[Δ1_, Δ2_, δα031_, α2_, ε_] :=
ArrayFlatten[Table[Table[If[n == M, E3mat[M, Δ1, Δ2, δα031, α2, ε], 0], {n, 6, -6, -1}], {M, 6, -6, -1}]];

(*define the off diagonal, dipole interaction blocks*)
DipMat21[Ω1_, q_, F1_, F2_] :=
Ω1 *
Table[Table[(-1)^ $\frac{9}{2}+1/2+F1+1$   $\sqrt{(2 F1 + 1) (2 F2 + 1)}$  SixJSymbol[{1/2, 1, 1/2}, {F2, 9/2, F1}] (-1)^F1-m1
ThreeJSymbol[{F1, -m1}, {1, q}, {F2, m2}], {m2, F2, -F2, -1}], {m1, F1, -F1, -1}];
DipMat32[Ω2_, q_, F2_] :=
Ω2 *
Table[
Flatten[
Table[Table[(-1)^ $\frac{9}{2}+1/2+F2+1$   $\sqrt{(2 F2 + 1) (2 F3 + 1)}$  SixJSymbol[{1/2, 1, 3/2}, {F3, 9/2, F2}] (-1)^F2-m2
ThreeJSymbol[{F2, -m2}, {1, q}, {F3, m3}], {m3, F3, -F3, -1}], {m2, F2, -F2, -1}]];
(*Generalize these dipole blocks for arbitrary linear polarization, using |x> =  $\frac{1}{\sqrt{2}} (\sigma^- - \sigma^+) |*$ )
DipMat21Gen[Ω1_, θ_, F1_, F2_] :=
Cos[θ] DipMat21[Ω1, 0, F1, F2] +  $\frac{\sin[\theta]}{\sqrt{2}}$  (DipMat21[Ω1, -1, F1, F2] - DipMat21[Ω1, 1, F1, F2]);
DipMat32Gen[Ω2_, θ_, F2_] := Cos[θ] DipMat32[Ω2, 0, F2] +  $\frac{\sin[\theta]}{\sqrt{2}}$  (DipMat32[Ω2, -1, F2] - DipMat32[Ω2, 1, F2]);
(*define the full Hamiltonian*)
HRWA[Δ1_, Δ2_, Ω1_, Ω2_, δα021_, α2_, ε_, θ1_, θ2_] :=
ArrayFlatten[{Elmat[4], DipMat21Gen[Ω1, θ1, 4, 5], E2mat[5, Δ1, δα021, ε], DipMat32Gen[Ω2, θ2, 5]},
{ConjugateTranspose[DipMat21Gen[Ω1, θ1, 4, 5]], E2mat[5, Δ1, δα021, ε], DipMat32Gen[Ω2, θ2, 5]},
{0, ConjugateTranspose[DipMat32Gen[Ω2, θ2, 5]], E3mat[Δ1, Δ2, δα031, α2, ε]}]];$$

```

**Figure C.2:** Mathematica code used to define the generalized three level Hamiltonian (equation 3.15) for use in lineshape simulations. The Stark mixing  $Q$  matrix (see equation 3.7) is given in [28], and the hyperfine Hamiltonian is given in, for instance, [24]. We input for the hyperfine  $a$ ,  $b$ , and  $c$  constants the values recently measured in our group (appendix E and [17]).

```

(*creates vector corresponding to upper excited state, for calculation of transition probability*)
ExcitedVec[F_, m_] :=
  If[Abs[m] == 6, If[m == 6, Flatten[{Table[0, {n, 1, 20}], 1, Table[0, {n, 22, 60}]}], 
    Flatten[{Table[0, {n, 1, 59}], 1}], 
  If[Abs[m] == 5, If[m == 5, Flatten[{Table[0, {n, 1, F + 16}], 1, Table[0, {n, F + 18, 60}]}], 
    Flatten[{Table[0, {n, 1, 52 + F}], 1, Table[0, {n, 54 + F, 60}]}]], 
  If[Abs[m] == 4, If[m == 4, Flatten[{Table[0, {n, 1, F + 19}], 1, Table[0, {n, F + 21, 60}]}], 
    Flatten[{Table[0, {n, 1, 50 + F}], 1, Table[0, {n, 52 + F, 60}]}]], 
    Flatten[{Table[0, {n, 1, 23 + 4 (3 - m) + F}], 1, Table[0, {n, 25 + 4 (3 - m) + F, 60}]}]]]];
PeaksCombine[peaks_, vmin_, vmax_, step_] := (*frequencies in peaks MUST be integer multiples of 'step'!!*)
Module[{peaksnew, fullspectrum},
  Do[peaksnew[m] = Table[If[n ≥ peaks[[m, 1, 1]] && n ≤ peaks[[m, Length[peaks[[m]]], 1]],
    peaks[[m, 1 + (n - peaks[[m, 1, 1]])/step]], {n, 0}], {n, vmin, vmax, step}],
  {m, 1, Length[peaks]}];
  fullspectrum = Table[{n, Sum[peaksnew[m][[(n - vmin)/step + 1, 2]], {m, 1, Length[peaks]}]}, 
  {n, vmin, vmax, step}];
  Return[fullspectrum];
];

SimSpectrum[Ez_, Ω1_, Ω2_, δα021_, δα031_, α2_, θ1_, θ2_, step_, range_] :=
Module[{finalvec, initialvec, Hrwa, rangelow, rangehigh, vals, vecs, probexc},
Clear[probCompile]
Do[Print["F=" >> ToString[Flevel]];
Do[
  finalvec = ExcitedVec[Flevel, mlevel];
  initialvec = 1/3 Flatten[{Table[1, {n, 1, 9}], Table[0, {n, 1, 51}]}];
  (*initial state -- assumes equal thermal population in all m sublevels*)
  Hrwa[Δ_] = HRWA[-1/2 δα021 * Ez^2, Δ, Ω1, Ω2, δα021, δα031, α2, Ez, θ1, θ2]; (* Rotating wave Hamiltonian,
  Δ=variable detuning, 410nm transition always on resonance *)
  rangelow =
    Round[(vselect[Ez, δα031 - δα021 (*correction to get to δα032, which we actually measure*),
      α2, Flevel, mlevel] - range/2), step];
  (*compute lineshape over window of size 'range'*)
  rangehigh = Round[(vselect[Ez, δα031 - δα021, α2, Flevel, mlevel] + range/2), step];
  probCompile[Flevel, mlevel] = {};
  Do[(* iterate through Δ values to make lineshape for one mp level*)
    {vals, vecs} = Eigensystem[Hrwa[Δ]]; (* Numerically find eigensystem *)
    probexc = Sum[Abs[finalvec.vecs[[i]] vecs[[i]].initialvec]^2, {i, 1, 60}];
    (*Find t-averaged probability of excitation *)
    AppendTo[probCompile[Flevel, mlevel], {Δ, probexc}], (*Compile into a list *)
    {Δ, rangelow, rangehigh, step}];
  Print["m=" >> ToString[mlevel]];
  {mlevel, -Flevel, Flevel}],
{Flevel, 4, 6}];
Fpeaks = Table[Table[probCompile[F, m], {m, -F, F}], {F, 4, 6}];
FullSpec = PeaksCombine[Join[Fpeaks[[1]], Fpeaks[[2]], Fpeaks[[3]]], Round[-1/2 δα031 * 15^2 - 1000, step],
Round[-1/2 δα031 * 15^2 + 1000, step], step];
];

```

**Figure C.3:** Mathematica code used to simulate  $7P_{3/2}$  lineshapes for use in the tensor polarizability extraction work detailed in section 3.2.2. ExcitedVec and PeaksCombine are both called in SimSpectrum, which is the command we actually to simulate a line.

```
(*define the combined Stark/hyperfine Hamiltonian for a given m_F value*)
Vm[ε_, α0_, α2_, m_] := 
$$\left(-\frac{1}{2} \alpha_0 * \epsilon^2\right) \text{IdentityMatrix}[6 - \text{Max}[\{\text{Abs}[m], 3\}] + 1] +$$


$$\frac{1}{2} \alpha_2 * \epsilon^2 \text{Table}[\text{Table}[Q[F, Fprime, m], {F, 6, \text{Max}[\{\text{Abs}[m], 3\}], -1}], {Fprime, 6, \text{Max}[\{\text{Abs}[m], 3\}], -1}];$$

(*select the proper eigenvalue – taking F=6 to be the largest energy and F=3 to be the smallest*)
vselect[ε_, α0_, α2_, F_, m_] := If[F == 6, Max[Eigenvalues[Vm[ε, α0, α2, m]]],
```

$$\begin{aligned} &\text{If}[F == 5, \\ &\quad \text{If}[\text{Abs}[m] == 5, \text{Min}[\text{Eigenvalues}[\text{Vm}[\epsilon, \alpha_0, \alpha_2, m]]], (*\text{pick out second highest eigenvalue}*) \\ &\quad \text{Max}[\text{Select}[\text{Select}[\text{Eigenvalues}[\text{Vm}[\epsilon, \alpha_0, \alpha_2, m]], \# < \text{Max}[\text{Eigenvalues}[\text{Vm}[\epsilon, \alpha_0, \alpha_2, m]]] \&], \\ &\quad \#\text{ > Min}[\text{Eigenvalues}[\text{Vm}[\epsilon, \alpha_0, \alpha_2, m]]] \&]], \\ &\quad \text{If}[F == 4, \\ &\quad \text{If}[\text{Abs}[m] == 4, \text{Min}[\text{Eigenvalues}[\text{Vm}[\epsilon, \alpha_0, \alpha_2, m]]], \\ &\quad (*\text{pick out second lowest eigenvalue}*) \\ &\quad \text{Min}[\text{Select}[\text{Select}[\text{Eigenvalues}[\text{Vm}[\epsilon, \alpha_0, \alpha_2, m]], \# < \text{Max}[\text{Eigenvalues}[\text{Vm}[\epsilon, \alpha_0, \alpha_2, m]]] \&], \\ &\quad \#\text{ > Min}[\text{Eigenvalues}[\text{Vm}[\epsilon, \alpha_0, \alpha_2, m]]] \&]], \\ &\quad \text{If}[F == 3, \text{Min}[\text{Eigenvalues}[\text{Vm}[\epsilon, \alpha_0, \alpha_2, m]]]] \\ &\quad ] \\ &\quad ] \\ &\quad ] \\ &\quad ];\end{aligned}$$

**Figure C.4:** Mathematica code used to pick out the energy of a given  $|F, m_F\rangle$  level under application of an electric field of magnitude  $\mathcal{E}$  kV/cm.

```
(*Stark mixing Hamiltonian, m_F=4*)
V4 = 
$$\left(-\frac{1}{2} \alpha_0 * \epsilon^2\right) \text{IdentityMatrix}[3] + \text{DiagonalMatrix}[\{\text{Vhf6}, \text{Vhf5}, \text{Vhf4}\}] -$$


$$\frac{1}{2} \alpha_2 * \epsilon^2 \text{Table}[\text{Table}[Q[F, Fprime, 4, 3/2, 9/2], {F, 6, 4, -1}], {Fprime, 6, 4, -1}];$$

(*Full Stark/hyperfine Hamiltonian*)
Vtenshf = V4 + 
$$\frac{1}{2} \alpha_0 * \epsilon^2 \text{IdentityMatrix}[3];$$

vals = Eigenvalues[Vtenshf];
(*scalar polarizability extraction*)
Δα0[ε1_, ε2_, ΔEmeas_, α2_] :=

$$\frac{((\text{vals}[[1]] /. \{\text{Vhf4} \rightarrow \text{Vhfs}[4], \text{Vhf5} \rightarrow \text{Vhfs}[5], \text{Vhf6} \rightarrow \text{Vhfs}[6], \alpha_2 \rightarrow \alpha_2, \epsilon \rightarrow \epsilon_1\}) -$$


$$(\text{vals}[[1]] /. \{\text{Vhf4} \rightarrow \text{Vhfs}[4], \text{Vhf5} \rightarrow \text{Vhfs}[5], \text{Vhf6} \rightarrow \text{Vhfs}[6], \alpha_2 \rightarrow \alpha_2, \epsilon \rightarrow \epsilon_2\}) - \Delta E_{\text{meas}}) / (\epsilon_1^2 - \epsilon_2^2);$$


```

**Figure C.5:** Mathematica code used to solve for the  $7P_{3/2}$  scalar polarizability given a measured  $|4, 4\rangle$  Stark shift,  $\Delta E_{\text{meas}}$ , between two electric fields  $\mathcal{E}_1$  and  $\mathcal{E}_2$ . The  $Q$  matrix and hyperfine Hamiltonian ( $\text{Vhfs}$ ) are defined as in the code in figure C.2.

### C.3 $7P_{3/2}$ Scalar Polarizability Extraction

As discussed in section 3.3.1 we extract a scalar polarizability by measuring the Stark shift of the resolved  $|4, 4\rangle$  sublevel at high field and inputting measured values to equation 3.20. This equation also requires that we numerically evaluate eigenvalues for the Stark mixing Hamiltonian; code for doing so is given in figure C.5. This can also be found in the `PolarizabilityExtraction` notebook in the author’s Mathematica folder on the lab server. Also contained in this notebook is code for implementing equation B.40 to extract a tensor polarizability.

# Appendix D

## MATLAB Code

In this appendix I will describe the suite of MATLAB code used for data analysis in this thesis. It is similar in design to code used in previous work and borrows much from, in particular, Allison Carter '16 [30] (to whose code the present author also contributed significantly) and Ben Augenbraun '15 [25]. This in turn traces back to thesis students and postdocs in the earlier 2010s, including those working on the hyperfine splitting measurements in thallium published in [16].

The process by which this code was developed – namely, by taking a previous iteration of code and modifying it to serve one's present purposes – means that it has inevitably become rather inelegant. While it does what it is intended to do, it is filled with code blocks that did, at some point, but no longer do serve any real purpose and others that are either particularly inefficient or particularly tedious. While I have attempted to remedy some of these issues over the course of the year, there are other points at which I have likely contributed to the problem. While by no means a pressing issue, a thorough reworking of this code could be a potential future project in the lab.

I have divided my code into two parts: one for  $7P_{1/2}$  Stark shift measurements, which is directly based on that used in [13, 25, 30] for the  $6P_{1/2}$  state; and a second for  $7P_{3/2}$  high-field measurements. Each has its own folder on the Majumder lab file server in the Z:\Nathaniel\MATLAB\ directory.

### D.1 $7P_{1/2}$ Stark Shift Code

#### D.1.1 Fitting of Raw Data

The main body of code is used to take the text files output from the LabView data collection program and fit the data contained therein to extract peak locations and/or Stark shifts. These files should be in a directory of the form [parent directory]\Date\Set Number\Voltage\Scan Direction\n2trialn3.txt, formatted as in, for instance, Z:\Nathaniel\Indium ABU Data\7P12\Thu, Apr 13, 2017\Set1\1kV\upscan\2trial0.txt. In the filename itself, n2 corresponds to the scan

number and `n3` conveys the electric field configuration, so that `2trial0.txt` is the field-free scan of the second on-off pair, and `2trial1.txt` is the field-on scan from the same pair. Each individual data file contains several header lines detailing experimental parameters (date and time obtained, crucible temperature, and measured voltage), as well as data column headers. The body of data consists in five columns, as follows: (1) point number, (2) red laser PZT voltage ramp, (3) Fabry-Pérot signal, (4) vapor cell signal, and (5) atomic beam signal.

The MATLAB code itself is contained in the folder `\Indium ABU Code 2017\7P12\`, and the master program, from which all the analysis is run, is `IndiumFittingABU12.m`. It allows the user to input several parameters, including the date and number of the dataset, the type of fit method (Lorentzian or overlap), and the linearization polynomial order; as well as more practical concerns like whether to save data (one might not want to for diagnostic purposes) or whether to display figures while fitting (again, viewing them is good for diagnostic purposes, but the code runs much faster when this feature is off).

The program proceeds into three `for` loops: the first selects upscans vs. down-scans, the second iterates through scan numbers, and the third iterates through field-off and field-on configurations. After having chosen the specific file for fitting by means of these loops, it proceeds to call a number of scripts to perform the fitting and associated tasks.

The first task is to obtain the measured voltage, a critical step in extracting meaningful Stark shift values. The program does this by means of a script, `FindMeasuredVoltage`, that combs through the header for the measured voltage and converts this into a double-precision value, `voltage_real`. We then proceed through the fitting process proper.

## Data Import and Preparation

We begin by importing the text data into a useable format: the script `getdataIndium` uses a `textscan` command to import the five data columns into an array. We then call `downsampleAndNormalizeIndium`, which inverts the time axis on downscan data to put them in order of *increasing* frequency,<sup>1</sup> downsamples the data to roughly 1000 data points (rarely necessary), normalizes the  $x$ -axis,<sup>2</sup> and normalizes the Fabry-Pérot and vapor cell data so that the amplitude of the largest peak is one. When using the Lorentzian fit method we also normalize atomic beam data, though we refrain from doing this for the overlap method – in this latter case, our goal is to compare raw lineshapes, and normalizing separately might change their relative shapes/sizes in an undesirable way. This program also attempts to remove ‘spikes’ in the data – electronic artifacts that lead to large, sharp ‘false peaks’ – though the present

---

<sup>1</sup>Is it important to note that, because of the location of the PZT in our particular laser, an upscan in voltage is actually a downscan in frequency, and vice-versa. We actually name our files in terms of the *voltage* scan direction, so it’s really the upscans that we invert to put in order of increasing frequency.

<sup>2</sup>See, for instance, [30] for the formula by which we normalize this axis.

implementation is not always effective.

### Fabry-Pérot Fitting and Scan Linearization

We next call the script, `FabryPerotFittingIndium_Airy`, which, as the name might imply, fits the Fabry-Pérot signal to an Airy function. To do this, it first calls `symppeaksIndium`, which finds each of the peaks in the spectrum and excludes those that fall too close to the edge of the scan. It then fits a linearization polynomial, of order `polyorder`, to a plot of peak point number vs. peak frequency (i.e. the FSR times the peak number). The resulting polynomial is used as an initial guess in the Airy function fit – doing this seems to significantly improve the quality of the fit over initial guesses of, for instance, zero for the higher order terms in the polynomial. After fitting, we save the linearization polynomial as a variable, `p`, for later use.

### Vapor Cell Fitting

We next fit the vapor cell data, using the script `LorentzianFitIndium`. We start by establishing the frequency axis, applying the linearization polynomial `p` to the raw (but normalized) vapor cell point number axis. We then use `symppeaksIndium` to find the six peaks in the spectrum and use these as initial guesses for a fit to a sum of six Lorentzians.<sup>3</sup> We then save the peak amplitudes, centers and widths, as well as the standard deviation for all quantities, in a vector, `Z`.

### Atomic Beam Fitting: Lorentzian Method

In the case of the Lorentzian method, we next fit the atomic beam signal to a sum of two Lorentzians, using a script, `LorentzianFitABU`, that takes the same approach as the vapor cell fitting program. Because atomic beam signals tend to have lower signal-to-noise ratios than their vapor cell counterparts, this process is slightly more challenging, and so we often also call the function `FindAbuPeaksIndium`, which varies the input parameters to `symppeaksIndium` in an effort to find two peaks. There are typically one or two scans in a set of 50 that `LorentzianFitABU` is simply unable to fit; we exclude these scans from later analysis. The results (peak heights, widths, centers, and standard deviations) are saved in a vector called `ZA`.

After fitting a set of field-free spectra, we save the vapor cell and atomic beam `Z` vectors, as well as the recorded voltage, and proceed to fit the field-on spectra from the same scan number. After doing so, provided none of the vapor cell or atomic beam fits failed, we call `WriteToFile_Full`; this saves field-on and field-off vapor cell and atomic beam fit data, as well as measured voltages (and a parameter called

---

<sup>3</sup>Sometimes, depending on the quality of the data, it is difficult to pick out the six peaks. If `symppeaksIndium` does not immediately find six peaks, we call a script, `FindHfsPeaksIndium`, which iterates through various averaging values (this ‘smooths out’ the signal to remove small spikes that could be mistaken for peaks) and minimum peak heights in an effort to find them.

`onoff`, used to determine whether data for this scan were taken in the OFF→ON or ON→OFF configuration<sup>4)</sup> to a text file for use in later analysis.

### Atomic Beam Fitting: Overlap Method

When using the overlap method, after fitting vapor cell data we re-zero the frequency axis to the location of the vapor cell reference peak by subtracting that peak's location from  $a_0$ , the constant term in the linearization polynomial. We then linearize the atomic beam frequency axis with this offset polynomial and save this axis and the atomic beam data for later use. We do the same for the field-on data.

Next, we define an interpolation axis over some convenient window surrounding the two peak locations (-1000 MHz to 1000 MHz is our typical choice). We then call `OverlapEvaluation`, which defines interpolating functions for both ABU signals and carries out the overlap method as detailed in section 5.1.3, determining chi-squared values for various shifts and then fitting a second-order polynomial to the minimum of the chi-squared curve. We finally save vapor cell fit data, overlap method shift results, voltages, and the `onoff` parameter to a text file using `WriteToFile_Overlap`.

### D.1.2 Final Analysis

After fitting raw data as described above, we have a variety of options regarding determination of final values. In our case, we use a script, called `ResultsTable` for Lorentzian data and `ResultsTableOverlap` for overlap data, to collect raw data into one place. Using this program, we can manually select each of the data sets we wish to consider for final analysis, running the code for each one to append sideband splittings, hyperfine splittings, and Stark shifts to a CSV file.<sup>5</sup> After analyzing all relevant sets in this way, we set the `findaverages` option to 1, calling a script called `TabulateAverages` that finds (weighted) averages of each column, yielding final values for the datasets in question. From here, we can view the results in spreadsheet format and use Excel, Google Sheets, KaleidaGraph, and/or other simple programs to evaluate overall Stark shifts and consider systematic errors.

## D.2 $7P_{3/2}$ Polarizability Code

Because of the preliminary stage of analysis in which we find ourselves for  $7P_{3/2}$  data, this code is not as well developed as its  $7P_{1/2}$  counterpart. Much of it is similar to the latter, of course; the differences are that there is no vapor cell data to consider and that the atomic beam signals at fields near 15 kV/cm look dramatically different than their low-field counterparts.

---

<sup>4</sup>This is determined by looking at the scan number: even numbers are OFF→ON and odd numbers are the opposite.

<sup>5</sup>Here we can use the weighted average approach or the histogram approach, though the former is more robust in data sets as small as ours.

Raw data files for  $7P_{3/2}$  scans are saved and formatted similarly to their  $7P_{1/2}$  counterparts. The only difference is that, because here all data are taken with the electric field on, filenames are simply given by (e.g.) `trial5.txt` – there is no need to distinguish field-on and field-off scans here.

The analysis is run through a program, `IndiumFittingABU32.m`, in the folder `\Indium ABU Code 2017\7P32\HighFieldABU\`. Because, for scalar polarizability analysis, we care about Stark shifts in the  $|4, 4\rangle$  level between fields, the program fits and saves two spectra, at different fields, for each scan number (e.g. it might fit `trial2.txt` for 15 kV and then `trial2.txt` for 16 kV – as explained in section 5.3, we take data for these different fields in direct succession).

We start by calling `FindMeasuredVoltage`, `getDataIndium`, `downsampleAndNormalizeIndium`, and `FabryPerotFittingIndium_Airy` as before. Because we have no vapor cell signal to work with, we instead reference directly to the Fabry-Pérot, simply enforcing that the first Fabry-Pérot peak in each relevant scan is set to the same value (typically either 0 or 363 MHz). We then select a window of each atomic beam scan containing the two peaks we wish to fit ( $|4, 4\rangle$  and ‘composite’)<sup>6</sup> and fit to a sum of two Lorentzians. Using `WriteToFile_Full`, we then save the fit results and voltages to a text file for later analysis.

We can use a variant of this program to fit individual scans (without comparing two voltages) in order to extract splittings for tensor polarizability determination. This program proceeds as above, except that there’s no need to worry about Fabry-Pérot referencing; here we save data for only one scan at a time.

We have implemented a short program, `SimpleResults`, for determination of the preliminary values quoted in this thesis. In the future, we will need to expand on this program to allow for the consideration of more data sets and the evaluation of systematic errors.

---

<sup>6</sup>The process for selecting this window is currently to enter the frequencies at which to cut by hand – it would be worthwhile, in the future, to design a means of automating this process.

## Appendix E

# Indium 7P Hyperfine Splitting Measurements

In this appendix we briefly describe a series of hyperfine splitting measurements in the indium  $7P_{1/2}$  and  $7P_{3/2}$  states, taken over the first summer of this thesis. The experiment is remarkably similar to that described in [16]. A recent thesis [34] and an arXiv paper [17] from this summer (during which we also measured hyperfine splittings and isotope shifts in thallium) provide further details on the present series of measurements.

### E.1 Experimental Setup

The experimental setup for this series of measurements is nearly identical to that employed in the vapor cell portion of our polarizability experiment. In particular, we lock the first-step, 410 nm laser to the  $5P_{1/2} \rightarrow 6S_{1/2}$  resonance in a supplementary oven, using an AOM-based subtraction technique described in detail in [16].<sup>1</sup> We then overlap a 685-690 nm diode laser, modulated at 1000 MHz by an EOM, with the 410 nm beam through a vapor cell, in either the same ('co-propagating') or opposite ('counter-propagating') direction as the first-step beam. We chop the first-step laser light and lock-in demodulate the red absorption signal at the chopper frequency to observe a hyperfine spectrum with high signal-to-noise (see figures E.1-E.2). A schematic diagram of the experimental apparatus is shown in figure E.3.

### E.2 Analysis Method

We linearize and calibrate our data using precisely the method of the  $7P_{1/2}$  scalar polarizability analysis above: a Fabry-Pérot spectrum is used for linearization (typi-

---

<sup>1</sup>While this paper describes an experiment involving the two thallium isotopes, the locking mechanism used in our indium measurements has a single locking slope, corresponding to the one relevant indium isotope.

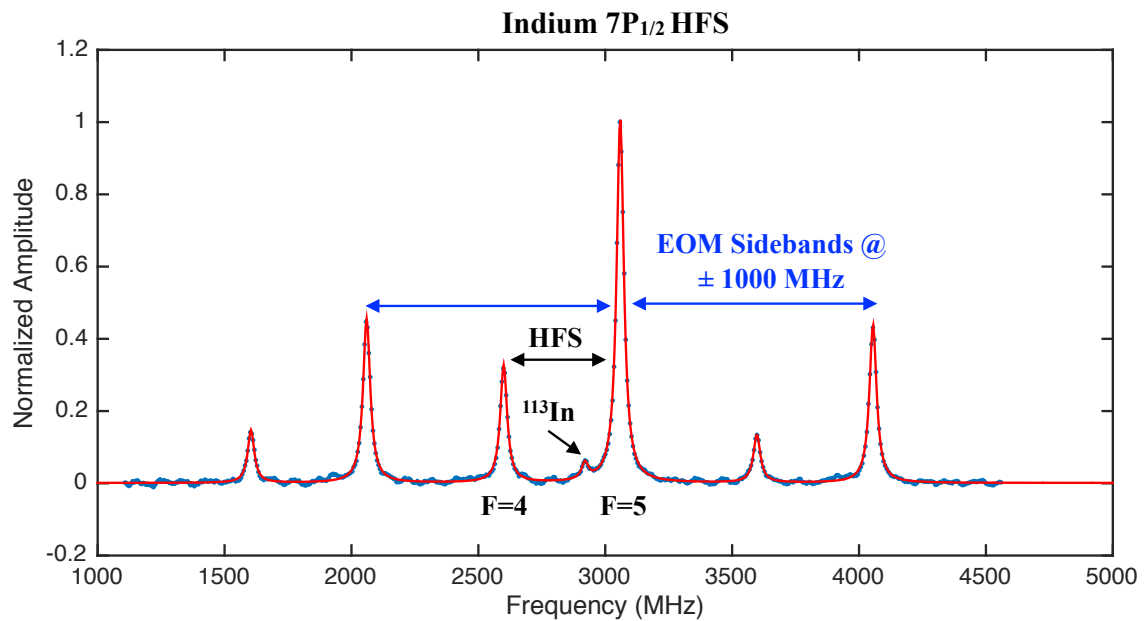


**Figure E.1:** Observed  $7P_{1/2}$  hyperfine signal (blue) with fit to sum of Lorentzians (red)

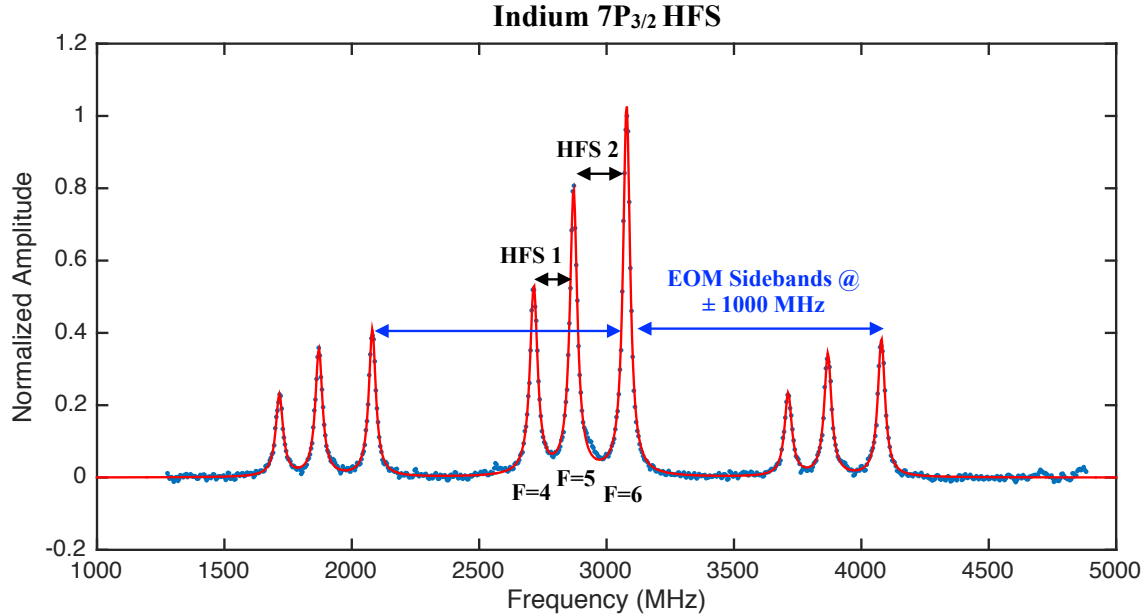


**Figure E.2:** Observed  $7P_{3/2}$  hyperfine signal (blue) with fit to sum of Lorentzians (red). Shown here is the signal corresponding to the first-step  $F = 4 \rightarrow F' = 5$  transition; that for the  $F = 5 \rightarrow F' = 4$  transition looks similar.

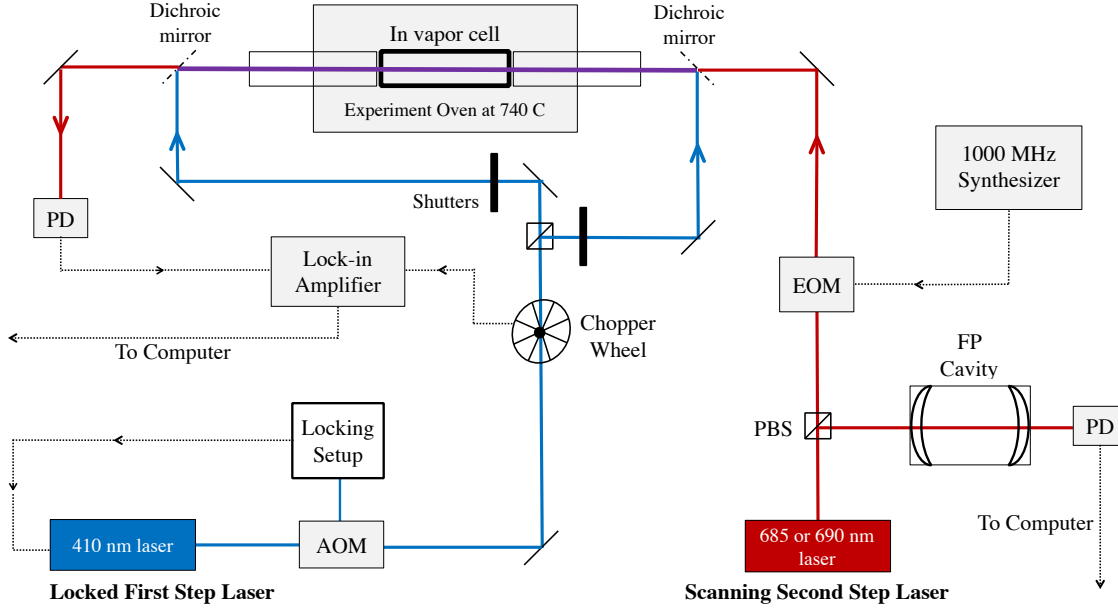


**Figure E.3:** Schematic of the experimental setup for hyperfine splitting measurements

cally with a fifth-order polynomial), and the  $\pm 1000$  MHz sidebands in our hyperfine signals are used for frequency calibration. We then fit our hyperfine spectra to simple sums of Lorentzians – six peaks for  $7P_{1/2}$  data and nine peaks for  $7P_{3/2}$  data – in order to extract peak locations and calculate hyperfine splittings.

### E.3 Extraction of Splittings and Statistical Errors

Having accumulated splittings from many raw scans, our next task is to consolidate these many sets of scans into a single value with a statistical error bar. There are several ways to do this.

The first means of combining the data is the most obvious: for a given splitting, simply pool together every value from every scan and find the mean and standard error. This can be done using the typical statistical formulas for mean and standard error, but another illuminating approach is to plot a histogram of the data. If the statistics are behaving themselves (and there is no reason to expect that they are not), the histogram should resemble a Normal distribution, and we can therefore fit a Gaussian function to the histogram to extract  $\mu$  and  $SE = \sigma/\sqrt{N}$ .

As it turns out, this method *underestimates* the standard error of the data. A glance at the histogram might indicate why: while we are treating all scans as a single set of Normally-distributed data, in reality what we have are a collection of data taken on different days and under different conditions (laser powers, polarizations, scan periods, *etc.*). Thus the histogram represents not so much one Normal distribution as the sum of many Gaussians, each with its own mean and standard deviation. The

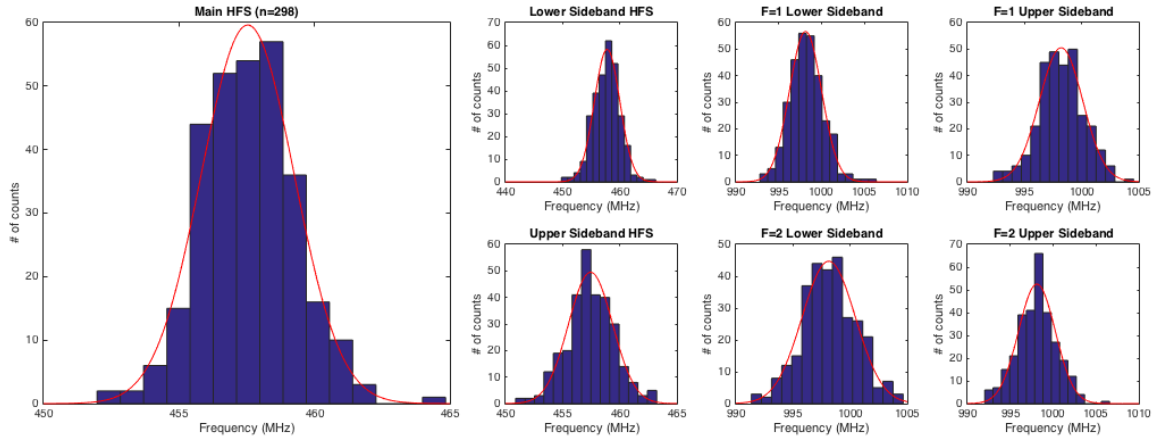


**Figure E.4:** Histograms, with Gaussian fits, of the various splittings of interest in one set of  $7P_{1/2}$  scans. The three leftmost histograms reflect the three HFS values explicit in a given scan (splittings  $1 \rightarrow 2$ ,  $3 \rightarrow 4$ , and  $5 \rightarrow 6$ ). Here their center values differ by a fraction of a MHz. The four rightmost histograms reflect the four sideband splittings in a given scan. Here these four splittings differ by at most 0.2 MHz, and their average value of 998.1 MHz leads to a calibration factor of  $\mathcal{C}_{EOM} = 1.0019$ .

means and standard deviations of each of these are comparable, meaning that the overall shape is roughly Normal, but the tails of the overall histogram will be too wide, and a Gaussian fit will inevitably underestimate the error.

Rather than pool together all data for a specific transition immediately and take a mean and standard deviation, we group the data by run, finding a mean and error bar for each run of order 100 scans and only then combining many runs to achieve a final result. This approach has two advantages: it enables us to obtain more accurate error bars than the single-histogram method, and it allows us to compare runs of data taken under different experimental conditions in order to test for systematics (more on this in section E.4).

There are two approaches we can take towards finding the relevant splittings and errors for these individual runs. The first proceeds as above: plot a histogram, fit to a Gaussian, and extract the mean and standard error from that fit (figure E.4).<sup>2</sup> The second method takes into account the fact that some scans fit more cleanly than others, resulting in less uncertainty. If we trust these scans more than noisier ones, we can take a weighted average,

$$\overline{\Delta\nu}_{\text{weighted}} = \frac{\sum_i \Delta\nu_i / \sigma_i^2}{\sum_i 1/\sigma_i^2}, \quad (\text{E.1})$$

<sup>2</sup>It is worth noting that these histograms do not typically consist of every scan from a particular run. Because some scans contain erroneous “spikes” and others have peaks whose locations prove elusive to the fitting program, we first eliminate all data beyond 4 standard deviations from the mean before making the histogram. In a Normal distribution, scans beyond  $4\sigma$  should hardly ever appear, so throwing them out amounts to eliminating the erroneous ones. We typically exclude 1-3% of the scans in a given run in this manner.

and compute a corresponding error,

$$\sigma_{\text{weighted}}^2 = \frac{1}{\sum_i 1/\sigma_i^2}, \quad (\text{E.2})$$

using values for  $\sigma_i$  corresponding to errors computed in the MATLAB fit.

After computing splitting values and errors from each individual set of scans using either the histogram method or the weighted average method, we combine these sets – typically by taking a weighted average (equations E.1 and E.2) of values computed from each set. The result is a final splitting value and statistical error reflecting several thousand scans of raw data.

## E.4 Consideration of Systematic Errors

What makes measurements of the sort performed in the Majumder group interesting is not only their statistical precision but also their accuracy, and ensuring accuracy requires thorough tests of potential systematic errors. Accordingly, we take data under many distinct experimental conditions, and while our final result is a reflection of all such data, we must carefully consider the potential errors in our measurement due to systematics. Below we outline several of the most significant sources of systematic error and explain the process through which we calculate a corresponding error to attach to the final result.

### Laser Propagation Direction

While taking data we alternately record scans in which the blue and red lasers pass in the same direction (co-propagating) and in opposite directions (counter-propagating) through the indium vapor cell. Though changing this propagation might shift the peaks in one direction or the other (if the 410 nm laser is not locked at the center of the  $5P_{1/2} \rightarrow 6S_{1/2}$  resonance), this shift should affect all hyperfine peaks equally so that the extracted splitting is the same.

In performing the analysis outlined above, we extract final values for all counter-propagating scans and all co-propagating scans separately, and any statistically resolved discrepancy is added to the error tally according to

$$\delta\nu_{\text{propagation direction}} = \frac{1}{2}|\Delta\nu_{\text{CTR}} - \Delta\nu_{\text{CO}}|$$

It is worth here noting that we consistently found the co-propagating scans to have wider peaks than the corresponding counter-propagating scans. While we were unable to uncover the reason for this distinction, it appears to be only a discrepancy in *shape* and not in *center* and is therefore of little concern.

## Laser Scan Direction

While taking data we record both *upscans*, where the frequency of the red laser increases through the scan; and *downscans*, where the frequency decreases through the scan. Though the direction of the scan should not impact the recorded splitting value, we sometimes find that it does.<sup>3</sup> We append a systematic error corresponding to any resolved discrepancy between upscans and downscans according to

$$\delta\nu_{\text{scan direction}} = \frac{1}{2}|\Delta\nu_{\text{UP}} - \Delta\nu_{\text{DOWN}}|$$

## Laser Sweep Speed

We take data with a wide range of scan periods (equivalent to a range of scan speeds), and, as always, expect no dependence in hyperfine splitting on sweep speed. Because the scan period is continuous rather than binary, its treatment is slightly more subtle.

To begin, we plot the final HFS value of each set of data against its corresponding scan period and apply standard least-squares regression to fit a line to the data. If there is no significant trend (i.e. the slope of the line is not statistically resolved from zero) we say there is no systematic associated with sweep speed. However, if there is a resolved slope, we must apply some sort of error. Typically we can divide the scan periods into two groups: one corresponding to “fast periods” less than 14 seconds and another corresponding to “slow periods” greater than 14 seconds.<sup>4</sup> We can then apply a systematic error according to

$$\delta\nu_{\text{sweep speed}} = \frac{1}{2}|\Delta\nu_{\text{fast}} - \Delta\nu_{\text{slow}}|$$

## Scan Linearization

When we fit the data we extract hyperfine splitting values not only from the center peaks but also from the sidebands (for example, in a  $7P_{1/2}$  scan we can extract an HFS value from the difference of peaks 4 and 3, 2 and 1, and 6 and 5; as well as 1000 minus the difference of peaks 3 and 2 and peaks 5 and 4). If the polynomial Fabry-Pérot fit does not entirely account for the non-linearity of the scan, that residual non-linearity should show up as a discrepancy in splitting values between those various sets of peaks. We can append a systematic error corresponding to this residual non-linearity by finding the largest of all the various sideband HFS values,  $\Delta\nu_{\text{max}}$ , as well as the smallest of all the various sideband values,  $\Delta\nu_{\text{min}}$ , and subtracting the two:

$$\delta\nu_{\text{scan linearization}} = \frac{1}{2}|\Delta\nu_{\text{max}} - \Delta\nu_{\text{min}}|$$

---

<sup>3</sup>One possible reason stems from the non-linear behavior of the laser, which changes depending on scan direction. A discrepancy in the HFS values from opposite scan directions might reflect our inability to entirely remove this non-linearity through the Fabry-Pérot fit, though there are other possible reasons we understand less well.

<sup>4</sup>While this number may seem arbitrary, for most HFS measurements we have several sets in the 12-13 second range and several more in the 15-18 second range, so this choice proved a convenient divider.

An alternate method of applying a scan linearization systematic involves the various 1000 MHz sideband splittings and is described in more detail in [34], section 4.3. This method tends to give decent agreement with that described above.

## Frequency Calibration

For each set of  $\sim 100$  scans we can find an average sideband splitting,  $\overline{\Delta\nu}_{\text{SB}}$  and compute a corresponding calibration factor,  $C_{EOM} = 1000/\overline{\Delta\nu}_{\text{SB}}$ , as outlined above. In principle, given perfect Fabry-Pérot fits and no thermal drift, this calibration factor should not vary from set to set, but in practice it does. In order to quantify the resulting uncertainty in frequency calibration, we can calculate a final HFS value using the largest calibration factor found in any one set of scans,  $\Delta\nu_{\text{max}} = \Delta\nu_{\text{raw}} * C_{EOM,\text{max}}$ , and then compute a similar value using the smallest calibration factor found in any set. We can then assign a frequency calibration systematic according to:

$$\delta\nu_{\text{frequency calibration}} = \frac{1}{2} |\Delta\nu_{\text{max}} - \Delta\nu_{\text{min}}|$$

## Indium-113 Contribution

As mentioned above, in the analysis of our  $^{115}\text{In}$  data, we must contend with the presence of small peaks due to  $^{113}\text{In}$ , the  $\sim 4\%$  abundant isotope. For the  $7P_{1/2}$  spectra, we can easily resolve at least one of these peaks (see figure E.1) and alternately fit and ignore this small peak in our analysis. It turns out that doing so does not affect our results in any statistically significant way, and so we apply no systematic error associated with the isotope.

As a glance at figure E.2 makes clear, accounting for the  $^{113}\text{In}$  isotope in a similar manner is impractical for the  $7P_{3/2}$  spectra. Indeed, in most cases we find no peaks with enough resolution to fit, and so we must establish another method of accounting for potential systematics. Our approach, ultimately, is to create simulated spectra (with relative peak amplitudes and signal-to-noise ratio as observed in the collected data) with small added isotopic peaks. In all cases we assume  $^{113}\text{In}$  hyperfine splittings that differ by  $\sim 1\%$  from those observed in  $^{115}\text{In}$  (this is consistent with past measurements of thallium-203 and 205 in the Majumder lab) and vary indium-113 peak locations over a range of roughly 100 MHz about the  $^{115}\text{In}$  peaks. We then fit these spectra using the same MATLAB program used for fitting laboratory data, and compare hyperfine splittings gathered from those fits with the splittings used to create the simulations. The discrepancy between extracted splitting values and ‘true’ values varies as a function of relative 113-115 location, with maximal errors arising when the indium-113 peaks are located a half-width away from their respective  $^{115}\text{In}$  resonances.

We cannot, and do not, expect that the indium-113 peaks are located at this ‘worst-case-scenario’ location in all our data (particularly because we alter the 410 nm lock point between sets), and so we accordingly apply systematic errors that fall

somewhat below this maximal value. Ultimately, these systematics appear at the level of less than 0.1 MHz and do not contribute significantly to our final error totals.

As a last note, it is worth mentioning that taking data in two propagation directions allows us greater confidence that we have adequately accounted for this second isotope. Because the first-step ( $5P_{1/2} \rightarrow 6S_{1/2}$ ) transition in  $^{113}\text{In}$  is excited off resonance, shifting propagation directions should effectively ‘flip’ the  $^{113}\text{In}$  peaks about their  $^{115}\text{In}$  counterparts, so that applying a propagation direction error, as we do, should at least in part account for this second isotope.

### Other Systematics

Throughout the data-taking process we vary other experimental parameters like laser polarization, laser power, oven temperature, and the 410 nm hyperfine transition ( $F = 4 \rightarrow F' = 5$  vs.  $F = 5 \rightarrow F' = 4$ ).

For red laser polarization, relative laser power, and oven temperature, we can apply a similar method to that for the scan period systematic described above. Namely, we plot HFS against the quantity of interest and use least-squares regression to fit a line to the data. If the slope is resolved, we can split the data into two subsets (it is typically apparent from the distribution of power ratios or polarization values where to divide them) and take half the difference of their mean HFS values as above. As can be seen in table E.1 below, few of the splittings admit polarization or power systematics.

The final systematic we consider regards the 410 nm hyperfine transition. In the case of the  $7P_{1/2}$  splitting, this first-step transition should not have any impact on the measured HFS, and indeed, we find no statistically resolved discrepancy between measurements taken with the two different transitions.

In the case of the  $7P_{3/2}$  splitting, meanwhile, this first-step transition determines which three hyperfine peaks we will observe in a scan by dipole selection rules. The  $F = 4 \rightarrow 5$  splitting is visible in both three-peak spectra, and we can compare the values of this splitting measured in each of the two spectra. Any resolved discrepancy is added to the error budget for the  $F = 4 \rightarrow 5$  HFS value as a ‘hyperfine group’ systematic:

$$\delta\nu_{\text{hyperfine group}} = \frac{1}{2} |\Delta\nu_{F=4 \rightarrow F'=5} - \Delta\nu_{F=5 \rightarrow F'=4}|$$

As it turns out, in our data this approach overestimates the hyperfine group error. Indeed, while the counter-propagating splittings agree quite closely between the two hyperfine groups, the co-propagating scans err significantly: for the  $F = 3, 4, 5$  scans the co-propagating data fall  $\sim 0.4$  MHz below the shared counter-propagating value while the co-propagating data for the  $F = 4, 5, 6$  scans fall  $\sim 0.4$  MHz *above* that value (figure E.5). Accordingly, so as not to double-count the propagation error, we apply a propagation direction systematic of  $\sim 0.5/2 = 0.2$  MHz and a hyperfine group error corresponding to the difference between the two *counter-propagating* values only. It turns out that the discrepancy between these counter-propagating values is not statistically resolved, so we ultimately apply no systematic for the hyperfine group.

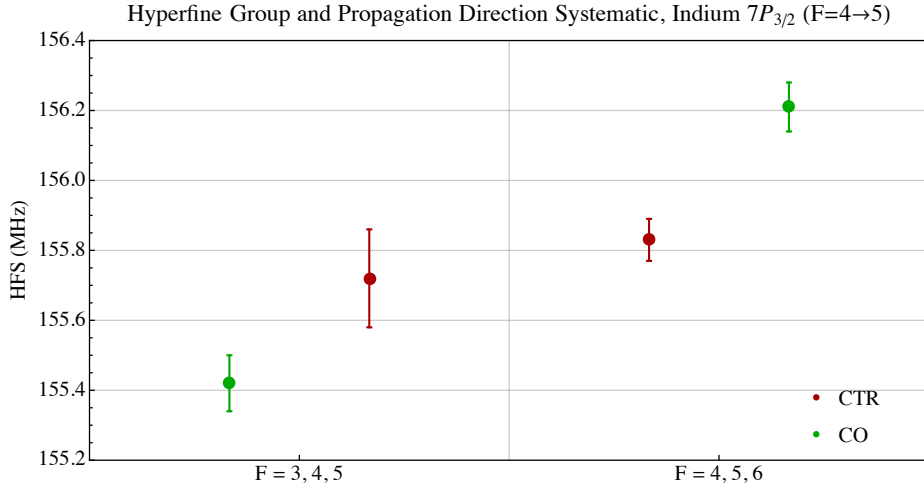


**Figure E.5:** Co and counter-propagating values for the  $7P_{3/2}(F = 4 \rightarrow 5)$  splitting derived from each of two different ‘hyperfine groups’ of three HF levels each. Note how the counter-propagating values agree closely while the co-propagating values differ, leading us to include only counter-propagating scans in our HF group systematic (doing otherwise would double-count the propagation direction systematic).

## E.5 Final Results

Our final results for the indium  $7P_{1/2}$  and  $7P_{3/2}$  hyperfine splittings, with associated statistical and systematic error budgets, can be found in table E.1. In each case the final error is at the level of one tenth of one percent (0.1%) – more than enough precision to serve as a useful test of theory.

Inverting equations 2.5-2.6 allows us to solve for the magnetic dipole, electric quadrupole, and magnetic octupole hyperfine constants,  $a$ ,  $b$ , and  $c$  respectively, from these final splitting values. The resulting values and associated errors, along with the results of a 1984 measurement [39] and theory calculations from [8], can be found in table E.2. Our results are in reasonable agreement with the previous measurements, though they represent roughly an order-of-magnitude improvement in precision. Interesting to note as well is that our measurements fall closer to the theory values than do the 1984 results. While this trend may not be statistically significant, it is at least somewhat encouraging.

Our measurements show a small but nonetheless resolved magnetic octupole constant for the indium  $7P_{3/2}$  state. While the previous measurements of this state [39] did not resolve this ‘ $c$ ’ constant, a 1957 paper [40] found such a resolved constant in the  $5P_{3/2}$  state of indium. Accordingly, the existence of a small nuclear octupole moment in indium has been known for some time.

Hyperfine Interval	$7P_{1/2}$ HFS	$7P_{3/2}$ HFS		
	$1 \rightarrow 2$	$3 \rightarrow 4$	$4 \rightarrow 5$	$5 \rightarrow 6$
<b>Final Result (MHz)</b>	458.44	114.01	155.77	208.37
<b>Statistical Error (MHz)</b>	0.03	0.03	0.05	0.04
<b>Systematic Error Sources (MHz)</b>				
Beam co vs. counter-propagation		0.10	0.25	0.27
Laser sweep speed and direction	0.10	0.04	0.05	0.04
Scan linearization	0.06	0.05	0.05	0.05
Frequency calibration	0.10	0.06	0.08	0.08
Red laser polarization	0.04			
Laser power			0.10	
$^{113}\text{In}$ Contribution		0.05	0.07	0.05
<b>Combined Error Total (MHz)</b>	0.16	0.15	0.30	0.30

**Table E.1:** Final hyperfine splitting results, with statistical and systematic error budget, for the  $7P_{1/2}$  and  $7P_{3/2}$  states of indium.

Level	Constant	Present Work	Ref. [39]	Theory [8]
$7P_{1/2}$	$a$	91.69(03)	90.7(1.0)	95.61
	$a$	32.18(03)	32.3(2)	30.83
$7P_{3/2}$	$b$	22.63(25)	24.5(1.5)	
	$c$	0.04(02)		

**Table E.2:** Comparison of hyperfine constants measured in this work against previous measurements (1984) and theory calculations.

# Bibliography

- [1] E. V. Hoenig, Bachelor's thesis, Williams College (2017).
- [2] P. A. Vetter, D. M. Meekhof, P. K. Majumder, S. K. Lamoreaux, and E. N. Fortson, Phys. Rev. Lett. **74**, 2658 (1995).
- [3] B. C. Regan, E. D. Commins, C. J. Schmidt, and D. DeMille, Phys. Rev. Lett. **88**, 071805 (2002).
- [4] S. G. Porsev, M. S. Safronova, and M. G. Kozlov, Phys. Rev. Lett. **108**, 173001 (2012).
- [5] B. K. Sahoo, R. Pandey, and B. P. Das, Phys. Rev. A **84**, 030502 (2011).
- [6] M. G. Kozlov, S. G. Porsev, and W. R. Johnson, Phys. Rev. A **64**, 052107 (2001).
- [7] M. S. Safronova, W. R. Johnson, U. I. Safronova, and T. E. Cowan, Phys. Rev. A **74**, 022504 (2006).
- [8] U. I. Safronova, M. S. Safronova, and M. G. Kozlov, Phys. Rev. A **76**, 022501 (2007).
- [9] M. S. Safronova, M. G. Kozlov, W. R. Johnson, and D. Jiang, Phys. Rev. A **80**, 012516 (2009).
- [10] B. K. Sahoo and B. P. Das, Phys. Rev. A **84**, 012501 (2011).
- [11] M. S. Safronova, U. I. Safronova, and S. G. Porsev, Phys. Rev. A **87**, 032513 (2013).
- [12] M. S. Safronova and P. K. Majumder, Phys. Rev. A **87**, 042502 (2013).
- [13] B. L. Augenbraun, A. Carter, P. M. Rupasinghe, and P. K. Majumder, Phys. Rev. A **94**, 022515 (2016).
- [14] D. S. Richardson, R. N. Lyman, and P. K. Majumder, Phys. Rev. A **62**, 012510 (2000).
- [15] M. Gunawardena, H. Cao, P. W. Hess, and P. K. Majumder, Phys. Rev. A **80**, 032519 (2009).

- [16] G. Ranjit, D. Kealhofer, G. D. Vukasin, and P. K. Majumder, Phys. Rev. A **89**, 012511 (2014).
- [17] P. M. Rupasinghe, N. B. Vilas, E. Hoenig, B.-Y. Wang, S. Cheng, and P. K. Majumder (2017), [arXiv:1702.06565](https://arxiv.org/abs/1702.06565).
- [18] S. C. Doret, P. D. Friedberg, A. J. Speck, D. S. Richardson, and P. K. Majumder, Phys. Rev. A **66**, 052504 (2002).
- [19] G. Ranjit, N. A. Schine, A. T. Lorenzo, A. E. Schneider, and P. K. Majumder, Phys. Rev. A **87**, 032506 (2013).
- [20] T. R. Fowler and J. Yellin, Phys. Rev. A **1**, 1006 (1970).
- [21] T. P. Guella, T. M. Miller, B. Bederson, J. A. D. Stockdale, and B. Jaduszliwer, Phys. Rev. A **29**, 2977 (1984).
- [22] M. S. Safronova, Email communication (2016).
- [23] D. J. Griffiths, *Introduction to Quantum Mechanics* (Pearson Prentice Hall, 2004), 2nd ed.
- [24] V. Gerginov, A. Derevianko, and C. E. Tanner, Phys. Rev. Lett. **91**, 072501 (2003).
- [25] B. L. Augenbraun, Bachelor's thesis, Williams College (2015).
- [26] J. Mitroy, M. S. Safronova, and C. W. Clark, J. Phys. B **43**, 202001 (2010).
- [27] A. Khadjavi, A. Lurio, and W. Happer, Phys. Rev. **167**, 128 (1968).
- [28] R. W. Schmieder, American Journal of Physics **40**, 297 (1972).
- [29] A. Kortyna, C. Tinsman, J. Grab, M. S. Safronova, and U. I. Safronova, Phys. Rev. A **83**, 042511 (2011).
- [30] A. L. Carter, Bachelor's thesis, Williams College (2016).
- [31] A. T. Lorenzo, Bachelor's thesis, Williams College (2011).
- [32] N. R. Bricault, Bachelor's thesis, Williams College (2014).
- [33] N. A. Schine, Bachelor's thesis, Williams College (2013).
- [34] S. Cheng, Bachelor's thesis, Williams College (2016).
- [35] A. S. Arnold, J. S. Wilson, and M. G. Boshier, Rev. Sci. Instrum. **69**, 1236 (1998).

- [36] C. J. Hawthorn, K. P. Weber, and R. E. Scholten, Rev. Sci. Instrum. **72**, 4477 (2001).
- [37] B. W. Shore, *Manipulating Quantum Structures Using Laser Pulses* (Cambridge U.P., 2011).
- [38] W. Demtröder, *Laser Spectroscopy: Basic Concepts and Instrumentation* (Springer, 1998), 2nd ed.
- [39] C. Belfrage, S. Hörbäck, C. Levinson, I. Lindgren, H. Lundberg, and S. Svanberg, Z. Phys. A **316**, 15 (1984).
- [40] T. G. Eck and P. Kusch, Phys. Rev. **106**, 958 (1957).